A MULTIMODAL BIOMETRIC AUTHENTICATION FOR SMARTPHONES

A DISSERTATION IN

Electrical & Computer Engineering

And

Mechanical Engineering

Presented to the Faculty of the University
of Missouri-Kansas City in partial fulfillment of
the requirements for the degree

DOCTOR OF PHILOSOPHY

by

SASHI KANTH SARIPALLE

M.S., University of Missouri-Kansas City, 2010

Kansas City, Missouri

2015

A MULTIMODAL BIOMETRIC AUTHENTICATION FOR SMARTPHONES

Sashi Kanth Saripalle, Candidate for the Doctor of Philosophy in Electrical Engineering

University of Missouri-Kansas City, 2015

ABSTRACT

Biometrics is seen as a viable solution to ageing password based authentication on smartphones. Fingerprint biometric is leading the biometric technology for smartphones, however, owing to its high cost, major players in mobile industry are introducing fingerprint sensors only on their flagship devices, leaving most of their other devices without a fingerprint sensor. Cameras on the other hand have been seeing a constant upgrade in sensor and supporting hardware, courtesy of 'selfies' on all smartphones. Face, iris and visible vasculature are three biometric traits that can be captured in visible spectrum using existing cameras on smartphone. Current biometric recognition systems on smartphones rely on a single biometric trait for faster authentication thereby increasing the probability of failure to enroll, affecting the usability of the biometric system for practical purposes. While multibiometric system mitigates this problem, computational models for multimodal biometrics recognition on smartphones have scarcely been studied. This dissertation provides a practical multimodal biometric solution for existing smartphones using iris, periocular and eye vasculature biometrics.

In this work, computational methods for quality analysis and feature detection of biometric data that are suitable for deployment on smartphones have been introduced. A fast, efficient

feature detection algorithm (Vascular Point Detector) for identifying interest points on images garnered from both rear and front facing camera has been developed. It was observed that the retention ratio of VPD for final similarity score calculation was at least 10% higher than state of art interest point detectors such as FAST, over various datasets. An interest point suppression algorithm based on local histograms was introduced, reducing the computational footprint of matching algorithm by at least 30%. Further, experiments are presented which successfully combine multiple samples of eye vasculature, iris and periocular biometrics obtained from a single smartphone camera sensor. Several methods are explored to test the effectiveness of multi-modal and multi algorithm fusion at various levels of biometric recognition process, with the best algorithms performing under 2 second on an IPhone 5s. It is noted that the multimodal biometric system outperforms the unimodal biometric systems in terms of both performance and failure to enroll rates.

APPROVAL PAGE

The faculty listed below, appointed by the Dean of the School of Graduate Studies, have examined a dissertation titled "A Multimodal Biometric Authentication for Smartphones," presented by Sashi Kanth Saripalle, candidate for the Doctor of Philosophy degree, and certify that in their opinion it is worthy of acceptance.

Supervisory Committee

Reza Derakhshani, Ph.D., Committee Chair
Department of Computer Science and Electrical Engineering

Gregory W. King, Ph.D.
Department of Civil and Mechanical Engineering

Ghulam M. Chaudhry, Ph.D.
Department of Computer Science and Electrical Engineering

Yugyung Lee, Ph.D.
Department of Computer Science and Electrical Engineering

ZhiQiang Chen, Ph.D.
Department of Civil and Mechanical Engineering

CONTENTS

LIST OF ILLUSTRATIONS

Figure Page

LIST OF TABLES

Table Page

ACKNOWLEDGMENTS

This dissertation is the result of various discussions, situations, deep collaborations and support of many great people. I would like to begin by thanking my advisor Reza Derakhshani. He has provided me with several years of guidance, teaching, and support. Reza not only supported my academic research but also gave me enormous freedom to develop and implement my own ideas, even though he did not concur with all of them. His knowledge and motivation towards research is an inspiration to me, and the example he has provided will stick with me long past my time at CIBIT lab.

I wish to members of my thesis committee for being flexible in accommodating me. Much thanks to Gregory King for his advice about the research writing and his systematic approach towards solving complex research problems.

A special shout out to my dear friend, Vikas alias 'V6'. Vikas was a major part of my research at CIBIT lab and has been instrumental in changing my view on approach towards scientific problems. He is remarkable in explaining even the most complicated computer vision algorithm in a way that everybody immediately sees the essence of the root concept. A huge thanks to Pavan Tankasala, 'da man', who is not only a great collaborator but also a friend who supported me throughout my research.

Finally and most importantly, I would like to thank my wife Deepthi. Her support, encouragement and unwavering love were undeniably the foundation upon which the past few years of my life have been built. I thank my family for their faith in me, and allowing me to be as ambitious as I wanted.

CHAPTER 1

INTRODUCTION

The goal of a biometric system is to provide a secure and convenient way of accessing high security information. Use of smart devices to access high security applications such as financial and personal mail has been on a rise and, so is the need in securing these smart devices. Traditionally, most of the smart devices are secured using a knowledge based token such as passwords and PIN's. These tokens are hard to remember and easy to forget. However, biometrics on other hand are convenient and robust. Additionally, availability of existing hardware such as cameras on these smart devices pave a smooth path for use of biometrics such as face, iris or eye vasculature.

Biometric system recognizes an individual based on certain unique physical or psychophysical features of the respective person. Eye vasculature biometrics is a science of recognizing a person based on visible red blood vessel patterns on human eye. In eye vasculature recognition, the biometric system captures the required biometric sample, extracts the region of interest (ROI), measures the quality of the ROI, extracts features from the ROI and, matches it against the existing database for a match. Based on the expected biometric sample quality, a local or global feature extraction and matching scenario is used. Most of the global feature matching algorithms are computationally demanding, and lack robustness with respect to non-linear distortions incurred during sample acquisition from smart devices. Aforementioned weakness of global feature matching is addressed using local feature matching. A local feature extraction method in a biometric system entails local interest point

detection and feature extraction. Although, several interest point detectors and feature extraction methods have been proposed in past decades, the problem of matching low quality images obtained from smartphones is far to be fully solved.

1.1. Motivation

Abundance of low cost smartphones and user friendly operating systems has seen a 25.3% rise in smartphone market in the second quarter of 2014. Only in second quarter of 2014, 301.3 million phones were shipped. Almost 60% of these smartphones do not have biometric systems integrated. However, all of these smartphones contain a rear and/or front facing camera. Eye vasculature biometrics uses visible vasculature on white to the eye to recognize a person that can be easily captured via front or rear facing camera. I show that it is feasible to build a software based multi biometric (eye vasculature, iris and periocular region) system using images garnered from front or rear facing camera.

1.2. Contributions

Unique contributions towards eye vasculature biometrics and multi modal biometrics for use in smartphones presented in this thesis are as follows:

- A new quality metric based on Vascular Point Detector (VPD). Amount of spatial content of visible vasculature is accurately calculated compared to other filtering methods. A framework of combining VPD with other quality metrics is proposed.
- The Vascular Point Detector, a non-training based curve and edge detector to find vasculature structures in noisy low resolution images is introduced. VPD can be easily

scaled to work on high resolution images. It is seen that VPD points has high retention rate compared to state of art corner and edge detectors.

- A Non Vascular Point Suppression (NVS) algorithm that eliminates the points that do not contain high information in their neighboring region. It is seen that the retention of VPD as well as other corner detectors such as FAST is improved by as much as 15%.
- A framework for progressive matching algorithm based on interest regions in periocular region. It is seen that progressive matcher reduces the computational footprint of multimodal biometric recognition in half on an average.

CHAPTER 2

BIOMETRIC SYSTEMS

Biometrics is a science of automatically identifying an individual based on their unique physiological or behavioral characteristics. Sir William Herschel demonstrated an initial use of handprint biometrics to verify worker's identity in 1858 (NTSC). In mid-19th century, Alphonse Bertillion, a law enforcement officer was famous for using physical body measurements to identify criminals (Jain et al., 2004). In late 19th century, use of fingerprints for person identification was proposed. Law enforcement departments immediately embraced the idea of using fingerprints for person identification based on the traits distinctiveness. However, initially, person identification based on fingerprints were manually verified. In early 20th century automated fingerprint biometric systems for person recognition were introduced. Since the introduction of automated biometric systems, use of biometrics has seen an exponential growth. Automated biometric system or biometric system is a device that collects a biometric sample from an individual, extracts features, compares the features against the available templates in the database, and returns a recognition result. Some of the most common biometric systems use fingerprints, face, iris and, voice traits (Jain et al., 2011). All biometrics systems are designed in a two-step process: Enrollment process and Recognition process. In enrollment process, the biometric system scans the biometric trait of an individual and further processes the trait to extract compact and meaningful representation. This representation of an individual's biometric trait is known as a template. The biometric system then stores the template in a local/central database. Recognition process is activated when the user wants to claim his/her identity to gain access. In the recognition process, the biometric system scans the biometric trait and processes the trait in a similar fashion as in enrollment phase. The processed

information is then compared to existing template in the database to establish the identity. Depending on the application, biometric systems can be realized in two modes: verification mode and identification mode. In verification mode, the system matches the biometric sample obtained from the individual with his/her own biometric templates stored in the system database. Verification mode is generally known as one vs. one comparison, where a user is identified based on a claimed identity. In identification mode, the obtained biometric sample from an individual is matched against various templates (many users) to establish an identity. This is commonly known as one vs. many comparison, where a user is identified without

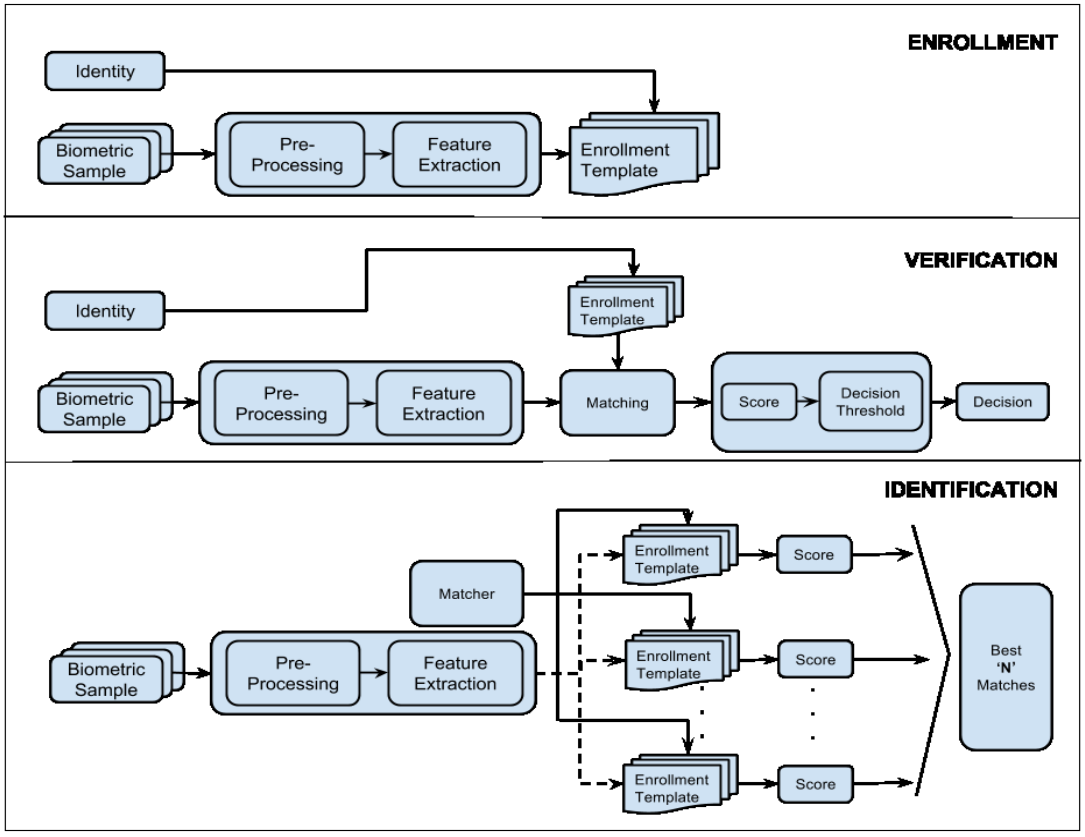

Fig. 1. Biometric models for authentication

claiming an identity (Fig. 1).

Biometric traits can be broadly divided into physical and behavioral traits (Jain et al., 2011). Physical traits are iris, fingerprint, face, eye vasculature, retinal vasculature, DNA, eye shape etc. and examples of behavioral traits are speech, signature, handwriting, gesture etc. Physical traits are something that can be measured over time. Behavioral traits are generally learned over time and are acquired after an effort from user. Voice biometric is one trait that is both physical and behavioral. Voice biometric is measured using vibrations of vocal cords and vocal tract shape, but also depends on user's behavioral state such as state of mind. Table 1 shows the current biometric system in consumer market. Fingerprint biometric systems are the most used followed by face biometrics (Derakhshani et al., 2008, Gottemukkula et al., 2011, Jain et al., 2004, Jain et al., 2008, and Ortega et al., 2006).

Table 1: Biometric market share in commercial segment

Biological Trait	***2012 Market Share[1]***	***Accuracy***	***Usability***	***Required Hardware***
Eyeprint	0 %	High	Medium	RGB Camera
Face	12.9 %	Medium	Medium	RGB Camera
Fingerprint	58.9 %	High	High	Optical or Capacitive Sensors
Hand Geometry	4.7 %	Low	High	Optical or Capacitive Sensors
Iris	5.1 %	Very High	Medium	Near Infrared Cameras
Others	12.2 %	Variable	Variable	Variable
Vein Recognition	3 %	Medium	Medium	Near Infrared Sub-Dermal Scanners
Voice	3.2 %	Low	Medium	Micro phone

Biometric systems that use a single biometric trait (Unimodal biometric systems) do not meet stringent performance standards needed in high security applications thus limiting them from being widely deployed on personal devices (Ross & Jain., 2004). Some common limitations of a unimodal biometric system are: Sensor noise, intra-class variation,

distinctiveness, non-universality, spoof attack. For example, in knowledge based authentication system, if a correct password is presented, the system always authenticates the user correctly. However, in a biometric system, even if legitimate biometric identifier is provided to the system, a correct decision cannot be guaranteed due to sensor noise or other aforementioned limitations of the system (Ross & Jain, 2004). Performance of all unimodal biometric systems saturate at a point from which additional performance becomes significantly difficult. In such situations, there is need of appending additional sources complementing the biometric system to increase its performance. When a biometric system accepts more than one biometric trait to generate a decision, it is known as multimodal biometric system.

Multimodal biometric systems are more robust due to the presence of multiple, independent biometric traits. These systems are also able to meet the stringent performance requirements imposed by high security applications. A multimodal biometric system due to its intrinsic property of collecting more than one unique biometric trait addresses the problem of non-universality. Further, multimodal biometric systems provide anti-spoofing measures by making it difficult for an intruder to simultaneously spoof the multiple biometric traits of an individual (Ross & Jain, 2003). Information originating from a multi biometric system can be fused in three ways: (a) Feature level fusion: Features from the multiple biometric samples are fused in initial stages to form a single large feature set. However, the features from different biometric traits need to be compatible for fusion. (b) Fusion at match score level: The match scores obtained from various biometric traits are fused to obtain a decision. (c) Fusion at decision level: Decisions from various biometric traits are combined using binary operations such as AND/OR rule, majority voting etc. Fusion at decision level is generally not preferred due to the scarcity of information available. A fusion at match score level is preferred when

the features from various biometric traits are not compatible to fuse at information level (Ross & Jain, 2003). Depending on available sensors and traits a variety of scenarios are possible in biometric system. A multimodal biometric system using multiple sensors for authentication on personal devices is not convenient. However, if multiple biometric traits can be extracted using a single sensor at the same time, the system becomes feasible for personal device authentication. In this thesis, I propose two such multi biometric systems that can be used for personal authentication using smartphones. The first multimodal biometric system uses eye vasculature and periocular biometric traits. The second biometric system uses, eye vasculature, iris and periocular biometric traits. Both systems acquire their biometric traits using a smartphone camera.

2.1. Biometrics on Smart Devices

Parallel to rapid growth of biometric systems, in early 20th century smartphones were making their way as an essential gadget for personal communication. As technology advanced, smartphones evolved, and in second quarter of 2014 alone, a growth of 31% was observed in sales of smartphones - a record 301 million smartphones were shipped in single quarter[1]. Due to their ease of use, powerful computing power and various sensors, smartphones are widely used for email, banking transactions, photography and many more applications replacing personal computers in some cases. It is expected that the use of smartphones for accessing high information data is only going to increase- particularly as the bring-your-own-device (BYOD) trend continues to grow even further in corporate industry. Due to the sensitive information that is being stored on the smartphones, it is absolutely necessary to secure the device.

[1] http://www.idc.com/prodserv/prodserv.jsp

Traditionally, knowledge based identity authentications such as passwords and PIN's are used to secure the device. However, passwords are easy to hack and hard to remember. It is seen that six of ten mobile users reuse passwords across multiple accounts. On the other hand, biometric systems are easy to use and tough to hack. A survey by Ericsson ComsumerLab[2] reveals that 52% of the 74,000 (74% of 100,000 consumers were interested in biometric technology on smartphones) interviewed consumers want to use fingerprint technology over passwords to unlock their device. The rest of 48% are interested in eye recognition to unlock the device. It is estimated that a whopping 63% of the smartphones shipped in the second quarter of 2014 alone do not have a biometric system integrated. Similarly, most consumer smart devices shipped a few years back do not have embedded biometric systems installed.

2.2. Eye Vasculature Biometric

2.2.1. Introduction and Background

Eye vasculature biometrics is a science of recognizing the person based on red blood vessel patterns on white part of the eye. Eye vasculature biometrics were first introduced by Dr. Derakhshani and Dr. Ross in 2006 (Derakhshani and Ross, 2006). In academia and industry eye vasculature biometric technology is known under various names: Conjunctival vasculature recognition, Eyeprint recognition, and Sclera recognition. Although, Zhou (Zhou et al., 2012) introduces Scleral recognition as a new biometric in 2012, they still use visible blood vessel patterns for matching purposes.

[2] http://www.ericsson.com/res/docs/2013/consumerlab/10-hot-consumer-trends-report-2014.pdf

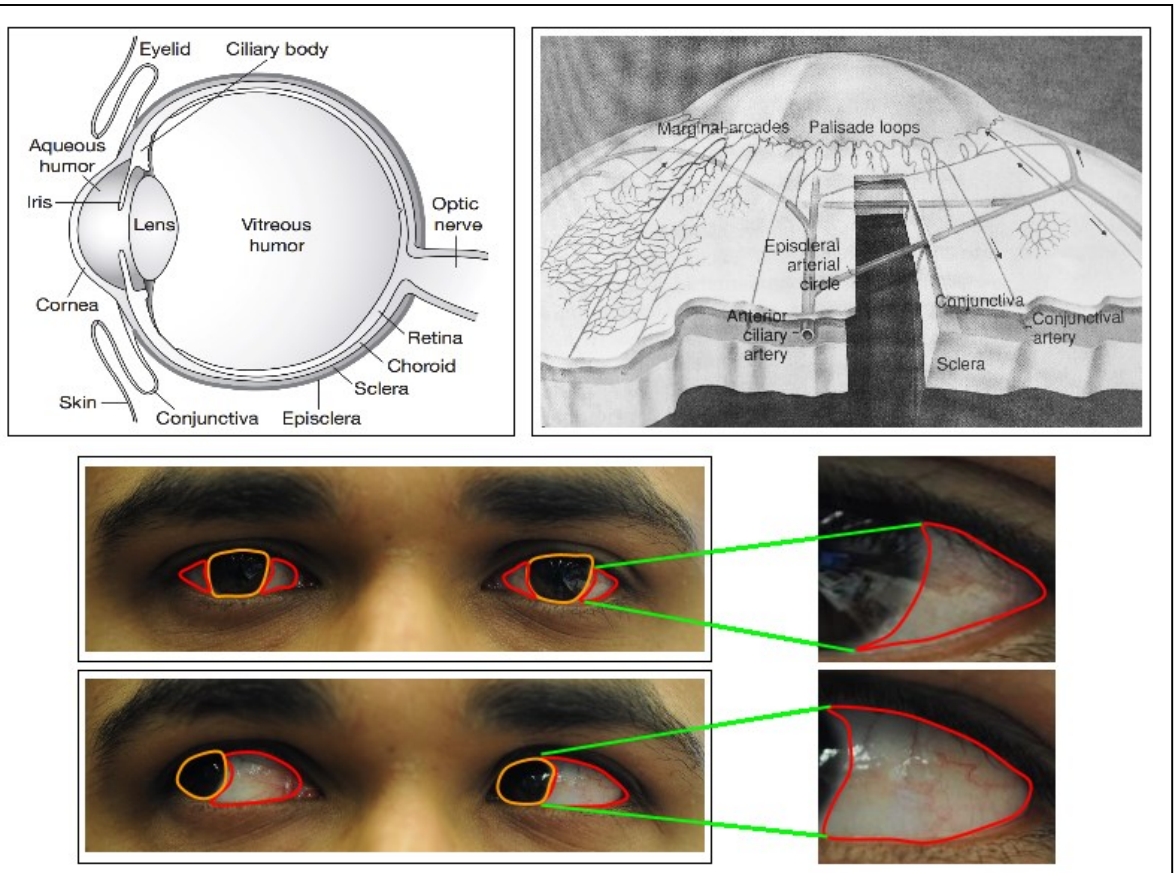

Fig. 2. (Clockwise): Anatomy of eye (Smith et al., 2007), lateral representation of sclera and conjunctiva (Bron et al., 1997), Eyeprint regions (enclosed in red boundary)

It is important to understand the anatomy of the human eye and, in particular the structure of blood vessels to define the eye vascular biometrics. Blood vessels on conjunctiva and episclera contribute towards the visible eye vasculature. Conjunctiva is a thin membrane which joins the eyeball to the eyelids. Although conjunctiva is continuous membrane it can be divided into three regions: palpebral, bulbar and fornical (Bron et al., 1997). The visible vasculature on white of eye from conjunctiva derives from bulbar conjunctiva. While conjunctiva is vascular, only vasculature from bulbar conjunctiva is seen due to the tissues anterior positioning with respect to sclera. The blood vessels on bulbar conjunctiva derive from anterior ciliary artery and long posterior ciliary artery. Anterior ciliary artery derives from muscular artery and splits to form smaller branches of episcleral arteries. The episclera

anteriorly separates sclera from bulbar conjunctiva and is vascular in nature due to episcleral arteries. The long posterior artery anatomizes with anterior ciliary artery in ciliary body. Similar to anterior ciliary arteries, anterior ciliary veins are derived from ophthalmic vein, which split into smaller braches deriving episcleral veins (Fig. 3). The combination of visible eye arteries and veins on human eye is termed as conjunctival vasculature by Derakhshani and Ross (Derakhshani and Ross, 2006) (Fig. 2).

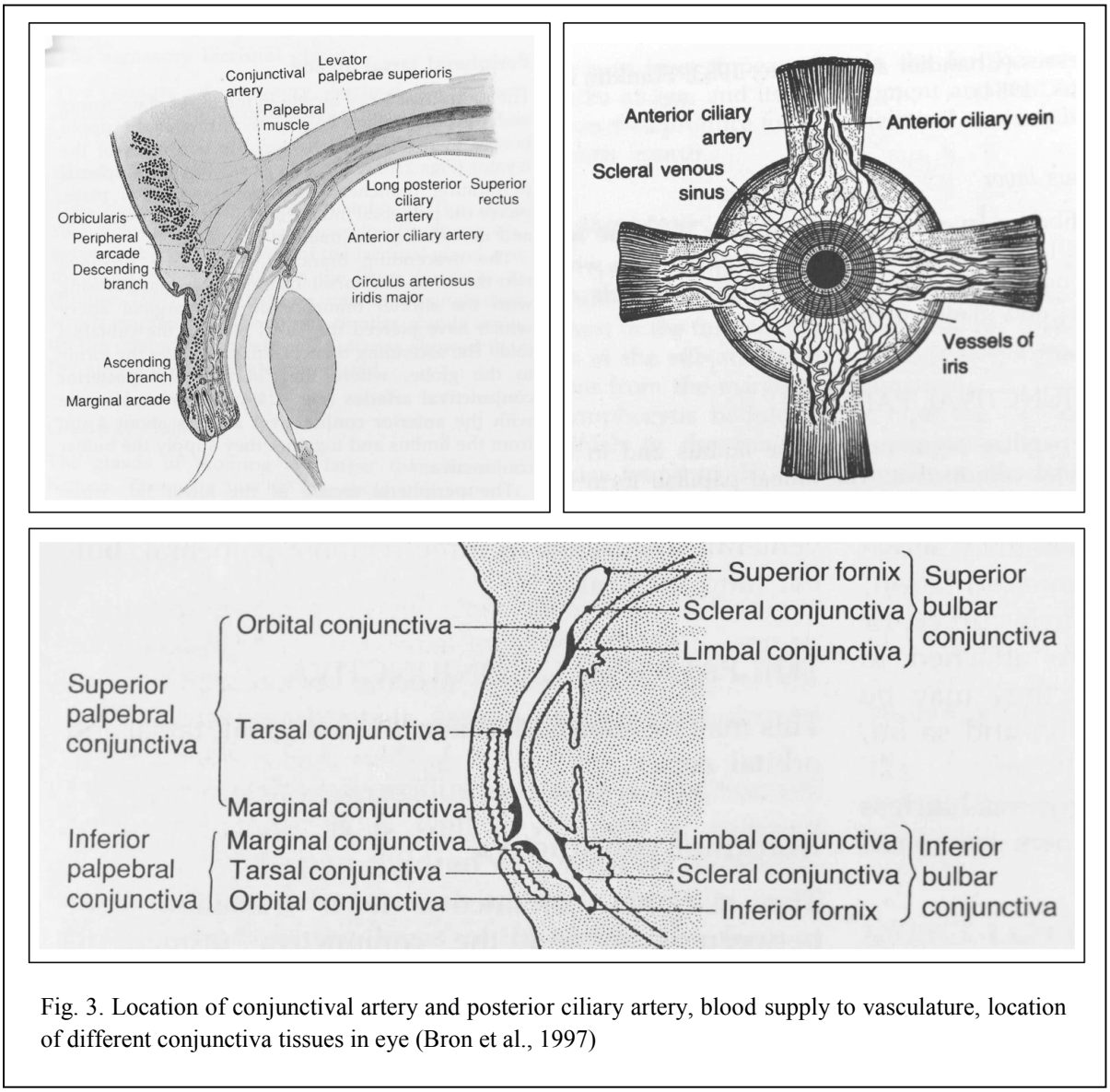

Fig. 3. Location of conjunctival artery and posterior ciliary artery, blood supply to vasculature, location of different conjunctiva tissues in eye (Bron et al., 1997)

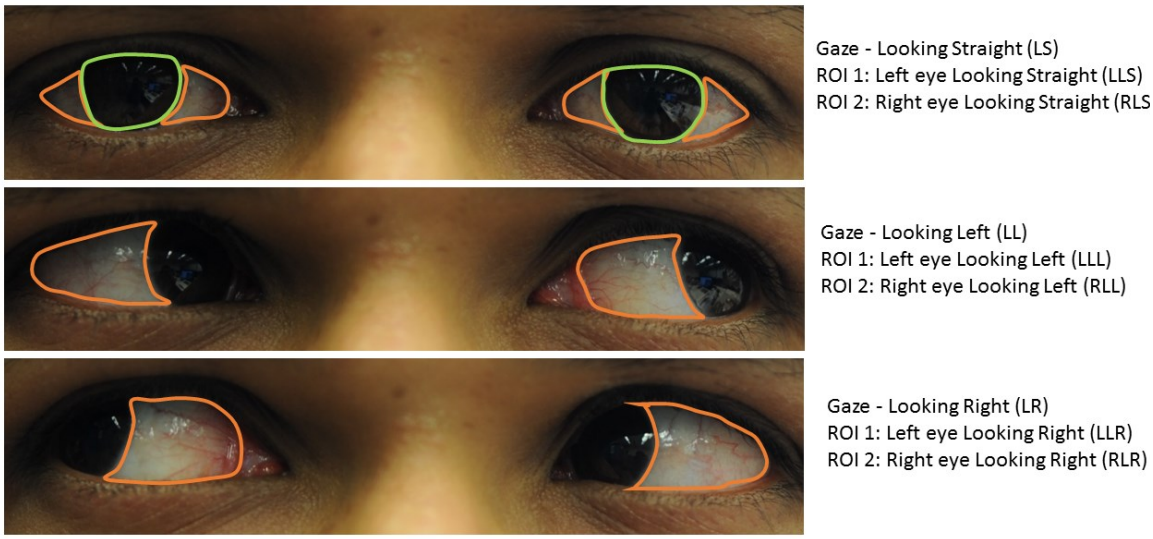

Fig. 4. ROI's in eye vasculature biometrics. All ROI's are bounded by orange boundaries for various gazes.

It is evident that the visible vasculature originates from ophthalmic artery and ophthalmic vein. Both the artery and vein are formed at the time of birth and are affected by various external factors that are not in control of humans. Thus, the formation of visible vasculature on sclera is completely random and the aforementioned process explains the reason for even twins having different vascular patterns (Hilfiker et al., 1998).

Eye vasculature recognition has been gaining a lot of interest in consumer industry and educational research for its use of simple RGB camera for personal authentication. Eye vasculature as a biometric trait gains its importance mainly for two reasons: (a) Eye vasculature recognition complements RGB iris recognition. (b) Eye vasculature recognition can replace iris recognition when iris is off angle or completely not visible in case of darker irides. It is seen from Fig. 4 that visibility of vasculature is maximum when the iris is off angle. The Eyeprint regions are marked inside an orange boundary and iris region is enclosed in green boundary. The Eyeprint regions (ROI) are marked accordingly based on gaze. The

Table 2: Summary of work on eye vasculature biometrics

Research Group	Year	Biometric Traits	EER (%) (*EV)	EER (%) (System)	Database	Hardware
Derakhshani et al.	2006	EV	0	0	In house (6 Subjects)	dSLR
Derakhshai et al.	2007	EV	4.3	4.3	In house (50 Subjects)	dSLR
Crihalmeanu et al.	2009	EV	25	25	In house (50 subjects)	dSLR
Thomas et al.	2010	EV	3.38	3.38	[a]UBIRIS v1	dSLR
Zhou et al.	2010	EV	1.34	1.34	[a]UBIRIS v1	dSLR
Zhou et al.	2012	EV, Iris	NA	NA	[b]UBIRIS v1	dSLR
Oh et al.	2014	EV, Peri Ocular	8.44	3.26	[b]UBIRIS	dSLR
Gottemukkula et al.	2013	EV, Iris	11.28	2.83	In house (50 Subjects)	dSLR
Gottemukkula et al.	2013	EV	11.28	2.83	[c]250 Subjects (Purdue Data)	iPhone 5
Tankasala et al.	2013	EV	10.22	4.52	[a]UBIRIS	dSLR

*EV – Eye Vasculature; [a] Selective UBIRIS dataset; [b] Partially constrained UBIRIS dataset; [c] Purdue University (BSPA Lab) collected the data as a 3rd party testing center

gaze is in reference to the subject. Table 2 provides an overview of existing eye vasculature biometric research. As it is evident from Table 2, eye vasculature biometrics is a fresh biometric technology explored only by a very few research groups.

Also, there are no publicly available datasets that were designed for eye vasculature biometrics. Computational Intelligence and Bio-Identification Technologies (CIBIT) lab at University of Missouri – Kansas City (UMKC) has a copy of a dataset collected from Purdue University which captures images of eye specifically targeted towards eye vasculature

recognition (Eyeprint biometrics). The dataset was obtained from EyeVerify®, a company that offers Eyeprint biometrics for consumer applications. Apart from this dataset, most of the research group use UBIRISv.1 (Proenca & Alexandre, 2005) or in-house datasets. The first biometric system for eye vasculature biometrics was based on minutiae based feature extraction on images captured from dSLR camera (Derakhshani & Ross, 2007). Gottemukkula (Gottemukkula, 2014) was the first researcher to use images from smartphones for eye vasculature biometrics. He proposes sophisticated feature extraction and matching methods for robust performance of eye vasculature matching. Other researchers have used images from dSLRs implementing various local and global feature extraction methods (Tankasala et al., 2013, Zhou et al., 2010, Crihalmeanu et al., 2009).

2.2.2 Eye Vasculature Properties

For a physical/behavioral trait to be deemed a biometric, it should satisfy a certain qualities a biometric trait possesses - *Universality, Distinctiveness, Permanence, Collectability, Performance, Acceptability and Circumvention* (Jain et al., 2004). Eye vasculature satisfy all the aforementioned qualities.

Universality – Vasculature, which is a combination of visible arteries and veins in human eye are essential for blood circulation and present in every human being.

Distinctiveness – Vasculature is randomly grown after human birth and is dependent on various environment conditions. Even conjoined twins do not share the same vascular patterns (Hilfiker et al., 1998).

Permanence – It is seen that the overall structure of visible vasculature seen in whites of the eye do not change for at least over 48-60 months. This was observed on an in-house dataset.

The vasculature changes in pattern only if users have a medical condition such as (Gottemukkula, 2014):

Diabetes: In certain users with high diabetes, loss of capillaries and macro vasculature dilation may occur that can change partial pattern of the visible vasculature (Owen et al., 2005, 2008).

Hyperemia & conjunctivitis: During these conditions, the visibility of vasculature in white of the eye will vary (Heath, 2006).

Scleritis: During this condition, non-prominent scleral vasculatures are engorged (Smith et al., 2007).

Subconjunctival hemorrhage: During this condition, the vasculature in bulbar conjunctiva will disrupt and other blob like patterns may appear due to blood clots (Mimura et al., 2010).

Collectability – It is seen that data collected by users in unconstrained environment from front facing camera of smartphones have been used for eye vascular recognition (Gottemukkula, 2014). It therefore can be claimed that collectability is rather convenient for eye vascular biometrics.

Performance – It is shown that in constrained environments, almost perfect recognition can be achieved on 250 subject database (Gottemukkula, 2014). Furthermore, it is shown that the computational cost for a verification process is less than a second on an iPhone 5s (Gottemukkula, 2014).

Acceptability – Acceptability of eye vasculature for biometric recognition is yet to be determined considering the biometric was recently introduced.

Circumvention– It is shown that eye vasculature can be fairly shielded from template attacks using steganography techniques introduced by Gottemukkula (Gottemukkula, 2014). Spoofing has been address by liveness detection (Derakhshani et al., 2013, 2014).

2.3.Periocular Biometric

2.3.1. Introduction and Background

Periocular region refers to facial region around the eye. There is no definition of what area around the eye periocular biometric is confined to, but, it mainly encompasses features derived from of eye shape, eyelashes, eye brows and surrounding ocular skin regions. The extent of area around ocular region to be considered for a periocular biometric system varies in many cases and mainly depends on application. Periocular region due to its ease of capture is considered to be a promising biometric complementing ocular biometrics (eye vasculature and iris). Although periocular biometrics derives its roots from facial biometrics, the research of periocular biometrics is still fresh and only a few authors published in this area. Park (Park et al. 2009) first investigated the feasibility of using periocular region in visible wavelength for recognition in non-constrained environment. After introducing periocular biometrics, most of the research into developing algorithms for periocular recognition have relied on general machine learning algorithms derived for other biometrics. Hollingsworth (Hollingsworth et al. 2010) were the first group to try and develop features exclusively for automatic periocular biometric recognition based on human verification performance on periocular images under different lighting conditions. They however show that feature regions that machines use for periocular recognition are different from human based periocular recognition. They claim that features derived around eyelids, eye shape, eyelashes and tear ducts could improve periocular

recognition. Santos et al. first studied the use of periocular biometrics on various smartphone. They show that fusion of periocular region with iris in visible wavelength improves the EER from 34.9% to 14.5%. Padole (Padole et al., 2012) show that periocular recognition is affected by distance of capture, pose, occlusion and skin pigmentation. In my scenario, the user is assumed to be corporative towards the biometric system. So, pose and occlusion noise are negligible.

Table 3: Summary of work on periocular biometrics

Research Group	Year	Biometric Traits	Best Recognition ([a]PO)	Best Recognition (System)	Database	Hardware
Park et al.	2009	PO	80.8% Rank-1	80.8% Rank-1	In house (30 subjects)	dSLR
Park et al.	2011	PO	87.32% Rank-1	87.32% Rank-1	FRGC v.2 (568 Subjects)	dSLR
Bharadwaj et al.	2010	PO	73.65% Rank-1	73.65% Rank-1	UBIRIS v2 (261 Subjects)	dSLR
Miller et. al	2010	PO	89.76% Rank-1	89.76% Rank-1	FRGC (410 Subjects)	SLR
Hollingsworth et al.	2012	PO	94.3% AUC	94.3% AUC	In house (210 Subjects)	dSLR
Adams et al.	2010	PO	92.16% Rank-1	92.16% Rank-1	FRGC (410 Subjects)	SLR
Padole et. al	2014	PO	NA	NA	In house (261 Subjects)	dSLR
Santos et al.	2014	PO, Iris	15.5% EER	14.5% EER	MICHE database	Smartphones
Oh et al.	2014	PO, EV	6.52% EER	3.26% EER	UBIRIS v.1 (241 Subjects)	dSLR
Woodard et al.	2011	PO	87% Rank-1	87% Rank-1	FRGC (410 Subjects)	dSLR

2.3.2 Periocular Region Properties

Periocular region satisfies the quality of a biometric to certain extent.

Universality – Periocular region is a part of face and, is present in all human beings.

Distinctiveness – Periocular region is distinct amongst various humans but not unique.

Permanence – Poor. Periocular region can change based on makeup and other environment changes such as UV exposure.

Collectability – High. Periocular region is conveniently collectable biometric.

Performance – Moderate.

Acceptability – Acceptability of periocular region for biometric recognition is poor considering the research was introduced very recently.

Circumvention– Spoofing periocular region can be mitigated using liveness detection. Attacks can be mitigated using steganography techniques (Gottemukkula, 2014).

2.4. Iris Biometric

2.4.1. Introduction and Background

Iris is the colored tissue around pupil region that is surrounded by *sclera* (white part of eye). The function of iris tissue is to control the amount of light entering the eye. The muscles in the iris, *dilator* and *sphincter* control the contraction and dilation of pupil region, and, therefore, the amount of light passing through the pupil. Iris tissue has a typical pattern consisting of furrows, ridges and pigment holes. It is believed that the formation of iris is based on genes and other environment conditions at time of birth. Due to its stochastic formation process, iris is distinct between any two individuals as well as distinct between the left and right eye of the same individual. The color of iris has been studied for its soft biometric

properties (Dantcheva et al., 2011). Texture of iris on other hand has been observed to be constant for a long time, however, some studies show that long term (11 years) iris recognition shows a drop in performance due to texture changes.

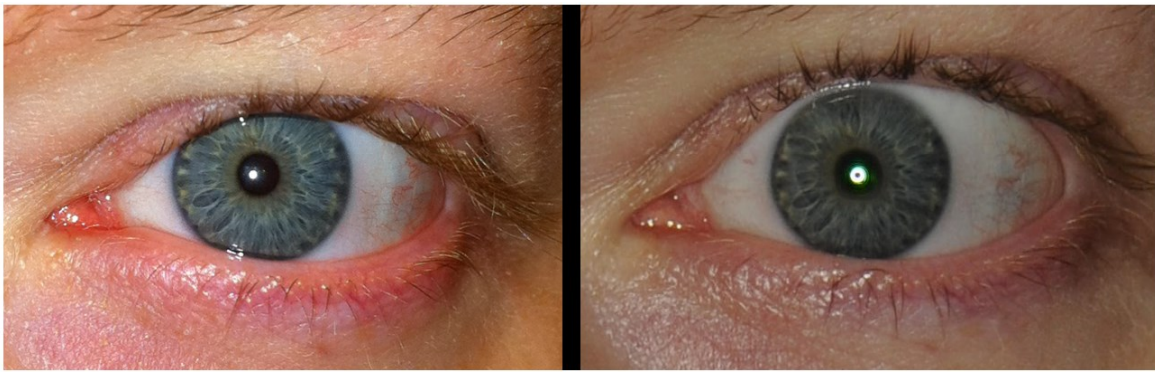

Fig. 5. RGB Iris image of same eye captured using iPhone 4S and Nikon D3S sensors

Automated iris biometric was first proposed by Flom and Safir in 1987. Johnston from Los Alamos National Laboratory published a study in 1992 reporting the permanence of iris structure over a period of 15 months on a sample size of 650 subjects (Johnston, 1992). His report concluded that iris was a potential biometric for recognition and identification, but no results were presented. A major breakthrough in automated iris biometric systems was achieved with Daugman's patent in 1994 (Daugman, J. 1994). Daugman presented a series of works showing the feasibility of automated operational iris biometric model. In 2004, he published a work on capturing iris in Near Infrared (NIR) spectrum for robust iris recognition. Iris images obtained in NIR spectrum are generally noise free and contain rich texture information regardless of the irides pigmentation. Most of the commercial iris biometric systems are built on the NIR iris biometric model proposed by Daugman (Daugman, J., 1993, 2004, 2010).

However, performance of iris recognition while using the similar aforementioned Daugman's method drops significantly in visible wavelength (VW). This is due to various

reasons, some of the most significant being (a) visibility of iris texture in dark pigmented irides (b) Non distinct limbic boundaries in various capture environments (c) various spectral and glare reflections. It has however been shown that a perfect recognition is possible in VW iris recognition if the images were noise free. Proenca (Proenca et al., 2010) first studied the feasibility of utilizing noisy VW iris for biometric recognition via NICE II competition. But, the aim of NICE II is to use iris as a biometric in non-corporative capture environment (covert operation scenario). Santos (Santos et al., 2014) used iris information obtained from front facing camera of smartphones to fuse with periocular regions. They use modified Daugman's approach towards matching iris images reporting best EER of 36.6% on 50 subject dataset.

2.4.2. Properties of Iris Biometric

Iris biometric satisfies all the properties of a biometric trait with high confidence.

Universality – Being a part of eye, iris is universal in nature.

Distinctiveness – Iris tissue is shown to be distinct across individuals as well as across individuals left and right eye.

Permanence – It is shown that iris is relatively permanent for a long period of time.

Collectability – Moderate. Iris recognition in NIR spectrum is very constrained. Unconstrained iris recognition is still very infant in nature.

Performance – High. A perfect accuracy is obtained for both, constrained NIR and VW iris biometric systems.

Acceptability – Acceptability is high. Government agencies have embraced this idea for border security on a large scale.

Circumvention– Spoofing iris region can be mitigated using liveness detection. Attacks can be mitigated using steganography techniques (Gottemukkula, 2014).

2.5. Proposed Multimodal Systems for Smartphones

Due to inherent properties of biometric traits, harsh capture environments, and external sensor manufacturing constrains, to date, no biometric system is able to achieve 100% recognition rates. This however can be alleviated by fusing multiple biometric traits without restoring to use of conventional passwords. On smartphones, the camera sensors are limited to optical improvements, and users tend to capture biometrics in surprising ways, thus demanding the need for multi-biometric capture. Also, use of unimodal biometric system leads to large False Reject Rates (FRR) and Failure to Capture (FTC) rates when the biometric captured is of low quality, thus making the use of biometric system unpleasant and at times frustrating. I show that the use of multiple biometrics lead to low FRR's.

2.5.1. Model 1

Model 1 is a combination of eye vasculature and periocular biometrics. We use this scenario when iris out of sight, in an off angle position. As we see in *Model 1*, I design a progressive matcher which matches the most significant biometric (eye vasculature, iris, periocular – based on availability) first. Significance of the biometric trait is based on expected image quality and computational time taken by respective biometric to declare a decision. If the first biometric system doesn't authenticate the person, then, the second biometric trait is fused with the

features of first biometric to obtain a decision improving the usability of the system.. Details of each block in the *Model 1* are explained in the respective sections of the following chapters.

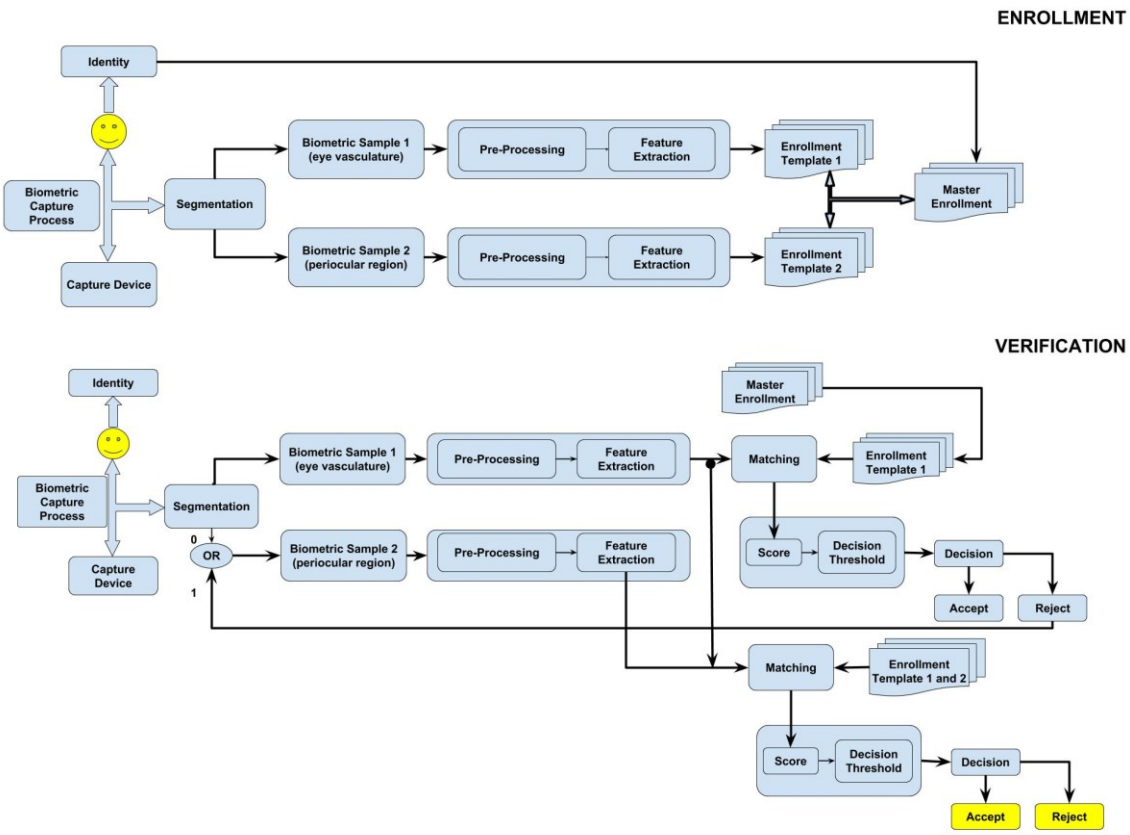

Fig. 6. Flow chart of proposed bimodal system (*Model 1)*

Matching the biometrics progressively helps reduce the computational time required to authenticate the person thereby

2.5.2. *Model 2*

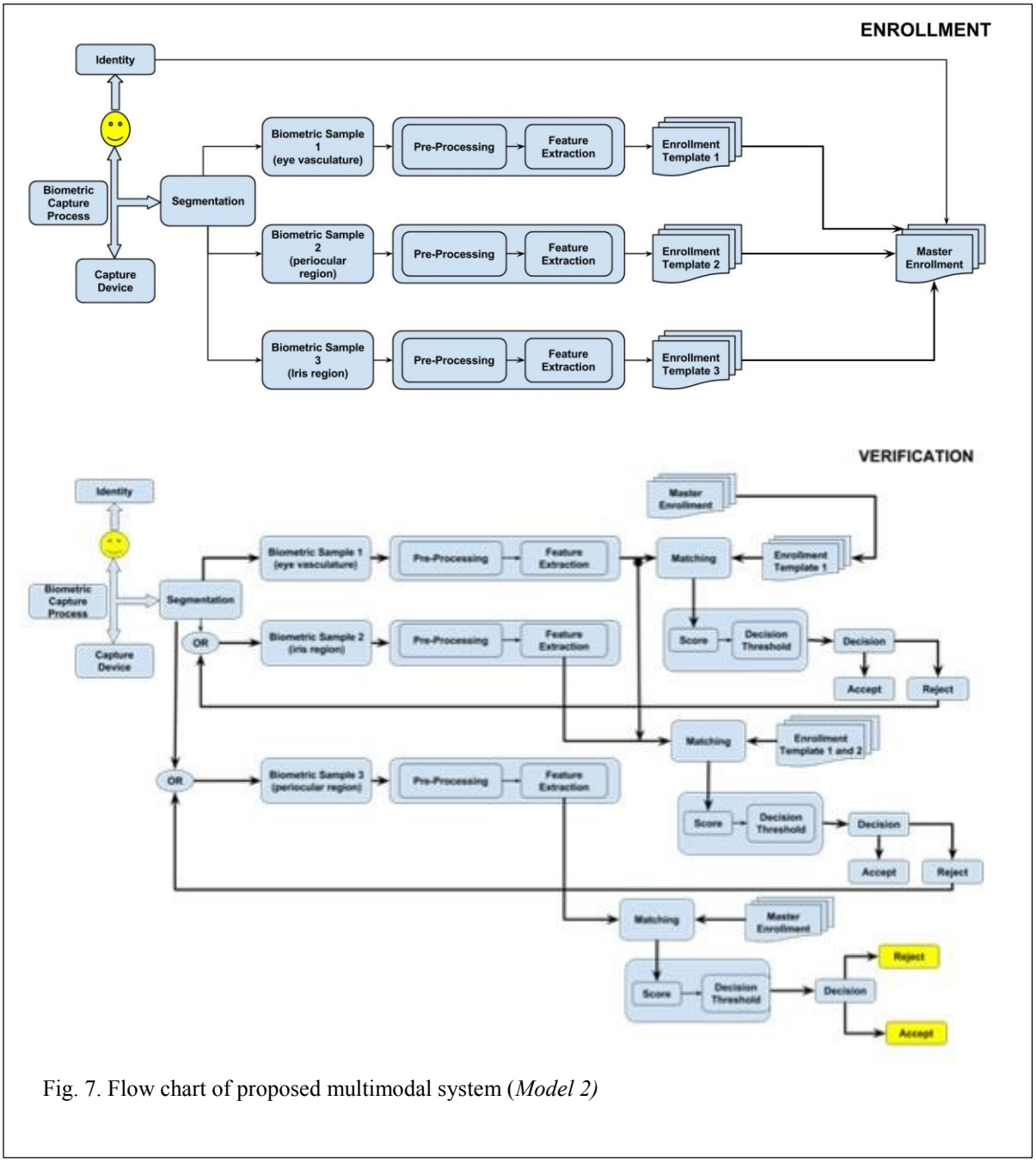

Fig. 7. Flow chart of proposed multimodal system (*Model 2)*

Model 2 is a fusion of eye vasculature, iris and periocular region. This model essentially uses

the complete eye, however, the information fusion between the three biometrics is sequential. As the verification progresses, the master template created at the time of enrollment releases respective biometric templates for matching purposes. *Model 2* is similar to *Model 1* in the way matching process is implemented except that three biometric modalities are involved.

CHAPTER 3

DATABASE

Three different databases are used to evaluate the methods proposed in this thesis (DB-I, DB-II, DB-III).

3.1. Database-I (DB1)

DB1 is collected by Biometric, Standards, Performance and Assurance (BSPA) Laboratory at Purdue University. A subset of DB-I was used by Gottemukkula to test the feasibility of using eye vascular biometrics for smartphones (Gottemukkula, 2014). While Gottemukkula has shown the biometric power of eye vasculature in matching Eyeprint from different days, I extend his dataset to show the capability of Eyeprint to match across various lighting conditions and capture scenarios. DB1 is further divided into parts - *DB1 Still*, *DB1 Video*.

Images in *DB1 Still* dataset were acquired with the rear-facing camera of iPhone 5. The images were captured in a regular *indoor* environment with ample lighting and, also in a dark indoor environment with no lights. In *dark* environment, no natural light was from windows was allowed. The phone was placed at a distance of 4 to 8 inches from the user and in built flash was used as a light source. 250 participants were invited for two sessions, each session being at least 7 days apart. Each session consisted of two sub-sessions, each sub-session being at least 15 minutes apart. Before the data collection procedure, all the participants were demonstrated on how to use the designed application by BSPA. The demonstration is not rigorous and was only intended to introduce the participant to the application. After the

demonstration, the participants were asked to follow the voice and haptic prompts from the data collection application. During the process, the participants were asked to look left and up for 2-3 seconds and then right and up for another 2-3 seconds. For each gaze, the phone captured multiple images, refocusing and re-metering every time. Fig. 8 shows a sample of all ROI's from *DB1 Still*.

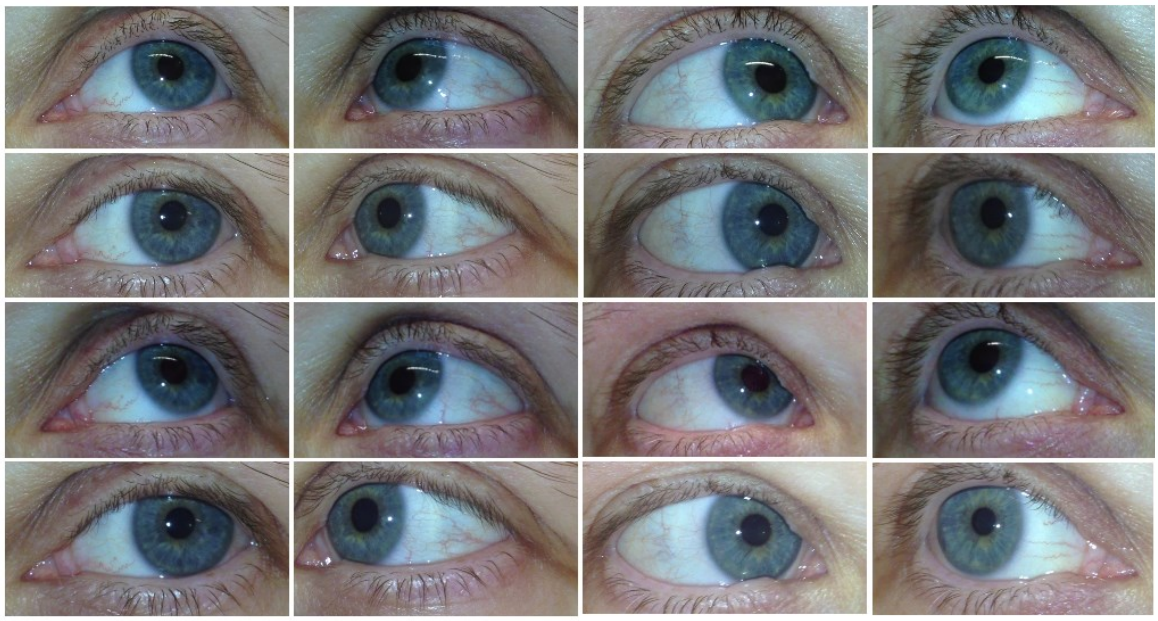

Fig. 8. Image samples from DB1. (Row wise): Still mode (light environment), Still mode (dark environment), Still mode (video environment), Video mode (dark environment)

DB1 Video is captured in the same procedure as *DB1 Still* except that video mode of back facing camera is used to capture images. In this case, re-metering and re-focusing the eye region for each capture is not performed. This procedure reduces the amount of time required to capture multiple images per session. Fig. 8 shows a sample of all ROI's from *DB1 Video*.

3.2. Database-II (DB2)

DB2 is captured using rear facing (*DB2 RF*) and front facing (*DB2 FF*) camera of iPhone 5 at Computational Intelligence and Bio-Identification Laboratory (CIBIT), UMKC.

DB2 RF images were acquired using a rear facing camera of an iPhone 5 in an indoor environment. Fifty volunteers were invited for two sessions that were 2 to 7 days apart. Each session consisted of two sub-session each at least 15 minutes apart. The application was demonstrated to each participant and a mock data capture was done with the participant. After the mock demo, the participants were given the phone for the actual data capture. The application generates a series of voice prompts guiding the participant to move the phone to optimal position for data capture. An optimal position is decided by the application when both eyes are in frame and in focus. Generally, the optimal position of the phone is around 4-8 inches from the participant. After the optimal position is attained, participants are asked to look up and to the left for 1 to 2 seconds, and then look up and to the right for another 1 to 2 seconds, with the related voice prompts being delivered by the device. At the beginning of the 1-2 second capture, the application adjust the focus on the eye region and meters the white balance. The images are recorded at 1080p video at 30 frames per second.

DB2 FF images are captured using the front facing camera of an iPhone 5 in indoor environment. *DB2 FF* images were captured at the same of capturing *DB2 BF* images from same participants. The capture process is similar to that of that explained in *DB2 BF*. However, for iPhone 5 front facing camera, the focus is fixed. So, the voice prompts were tailored to have participants move the phone to 4-6 inches from their face (focal range of iPhone 5). The images were recorded at 720p video at 30 frames per second. For *DB2 FF*, from the video feed at the time of capture, stacks of four consecutive images with highest

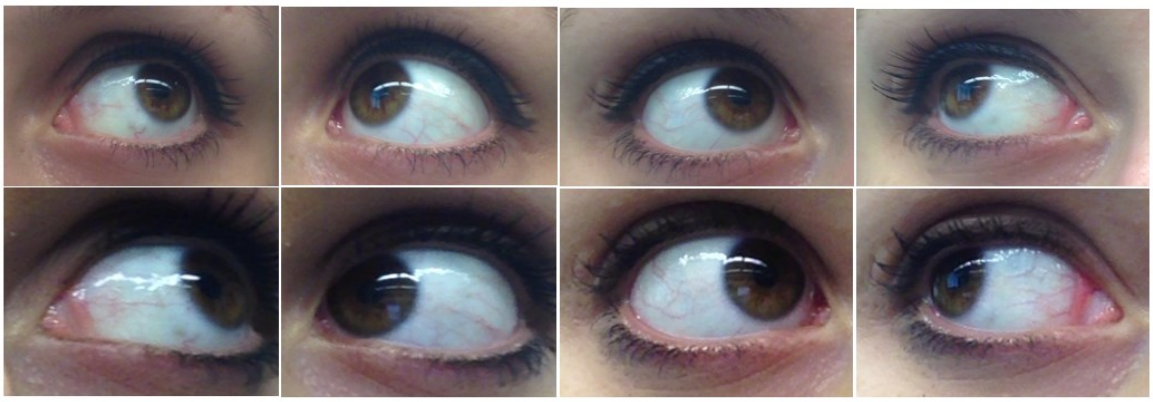

Fig. 9. Image samples from DB2. (Row wise): Back facing camera samples, Front facing camera samples

correlation are captured. All four images are averaged to produce one averaged image. Multiple averaged images are captured for each ROI from each session.

The aim of DB2 is to:

(a) Determine the robustness of proposed algorithms on low resolution front facing camera images.

(b) Determine if the Eyeprint from front facing camera sensor can be matched against an Eyeprint from back facing camera sensor or vice-versa.

3.3. Database-III (DB3)

DB3 is a collection of two databases (*DB3 HR, DB3 LR*). Participants were invited for two sessions 4-30 days apart. Each session consisted of two sub-sessions 30-45 minutes apart. During each session multitude of images were captured from each volunteer. Images for *DB3 HR* were collected using a contraption consisting of chin rest, controlled lighting and high resolution Nikon D3S camera. Images in *DB3 LR* were collected using iPhone 4S rear facing 8 megapixel camera from a distance of 8-12 inches. The subject were corporative to data

capture and the collection was performed under regular office environment. Each capture was acquired at different place in the office so that reflections on eye do not spatially reoccur. The aim of DB3 is

(a) Compare the robustness of proposed algorithms on high resolution and low resolution iris images in visible wavelength.

(b) To build a multimodal biometric system using Eyeprint, iris and periocular region.

Fig. 10. Image samples from DB3. (Row wise): dSLR (D3S) captures, iPhone captures

CHAPTER 4

EYE VASCULATURE RECOGNITION

Eye vasculature as a biometric trait has been promising based on its features as described in Chapter 2. The process of eye vasculature biometric system follows the procedure as shown in Fig. 11 (Enrollment, Verification). Below is the detailed flowchart of eye vasculature recognition process.

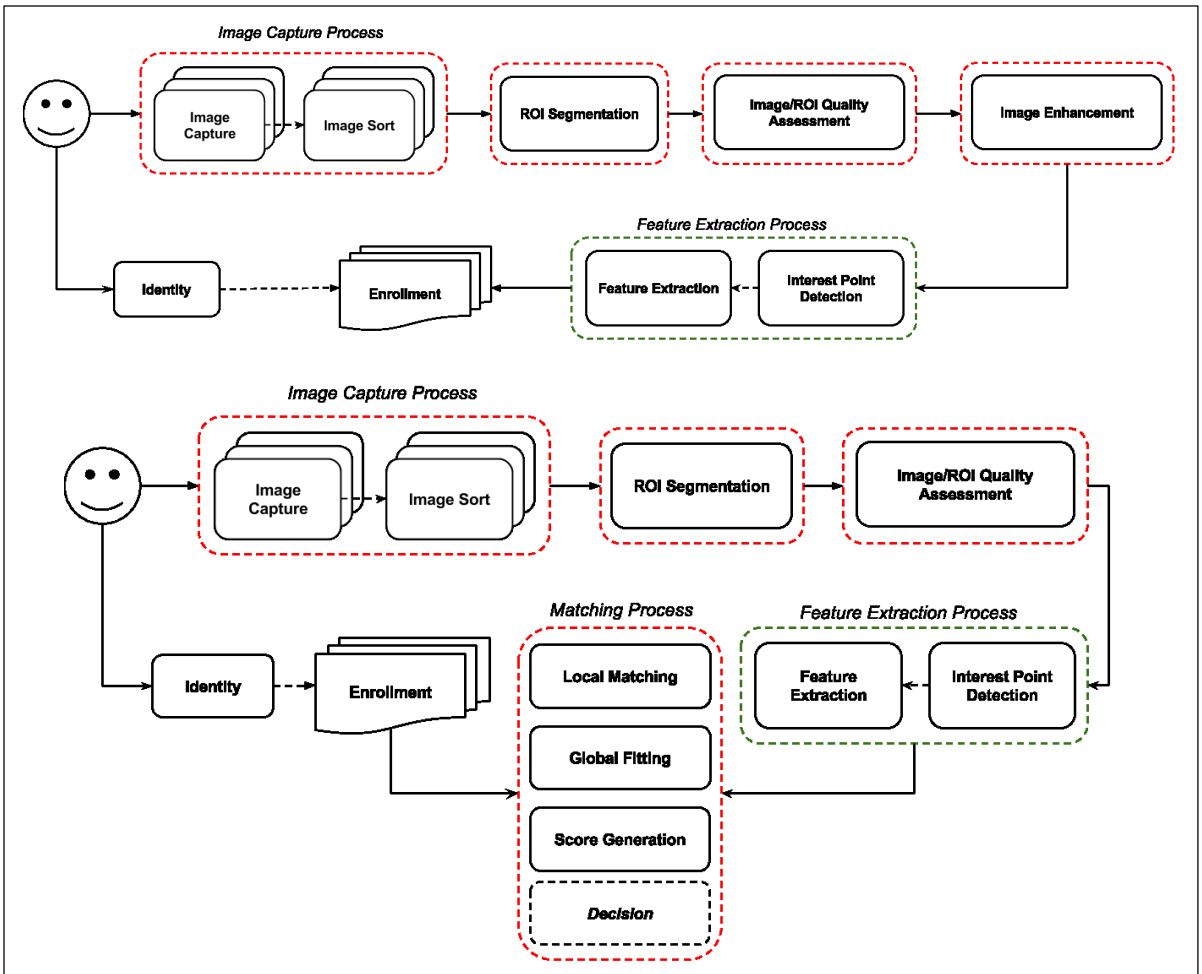

Fig. 11. Eye vasculature enrollment and verification process

4.1. Image Capture Process

The image capture process for all databases are explained in Chapter 3. Image sorting at image capture level is not implemented for all databases. For *DB1* images are excluded at image quality level after segmentation. For *DB3*, images are manually selected considering the aim of the database. However for *DB2*, multiple averaged images are collected. The images are further sorted and top *N* images are picked. The image capture pipeline is shown in Fig. 12. The sorting of the images is implemented using a sharpness metric derived from Laplacian of Gaussian (*LoG*) filter (Fig 11). The implementation of the algorithm is as follows:

Step 1: Normalize all images to values between 0 and 1. Call these normalized images.

Step 2: Convolve the normalized images with the *LoG* filter. Call these convolved images.

Step 3: Subtract each pixel of the convolved images with the maximum attainable value (one). Call these sharp masks.

Step 4: Multiply pixel by pixel sharp masks with corresponding normalized images. Call these coarse images.

Step 5: Find the difference between standard deviation of coarse images and normalized images. Call this sharpness metric.

Step 6: Sort the normalized images in descending order of sharpness metric.

Step 7: Pick first N normalized images after sorting.

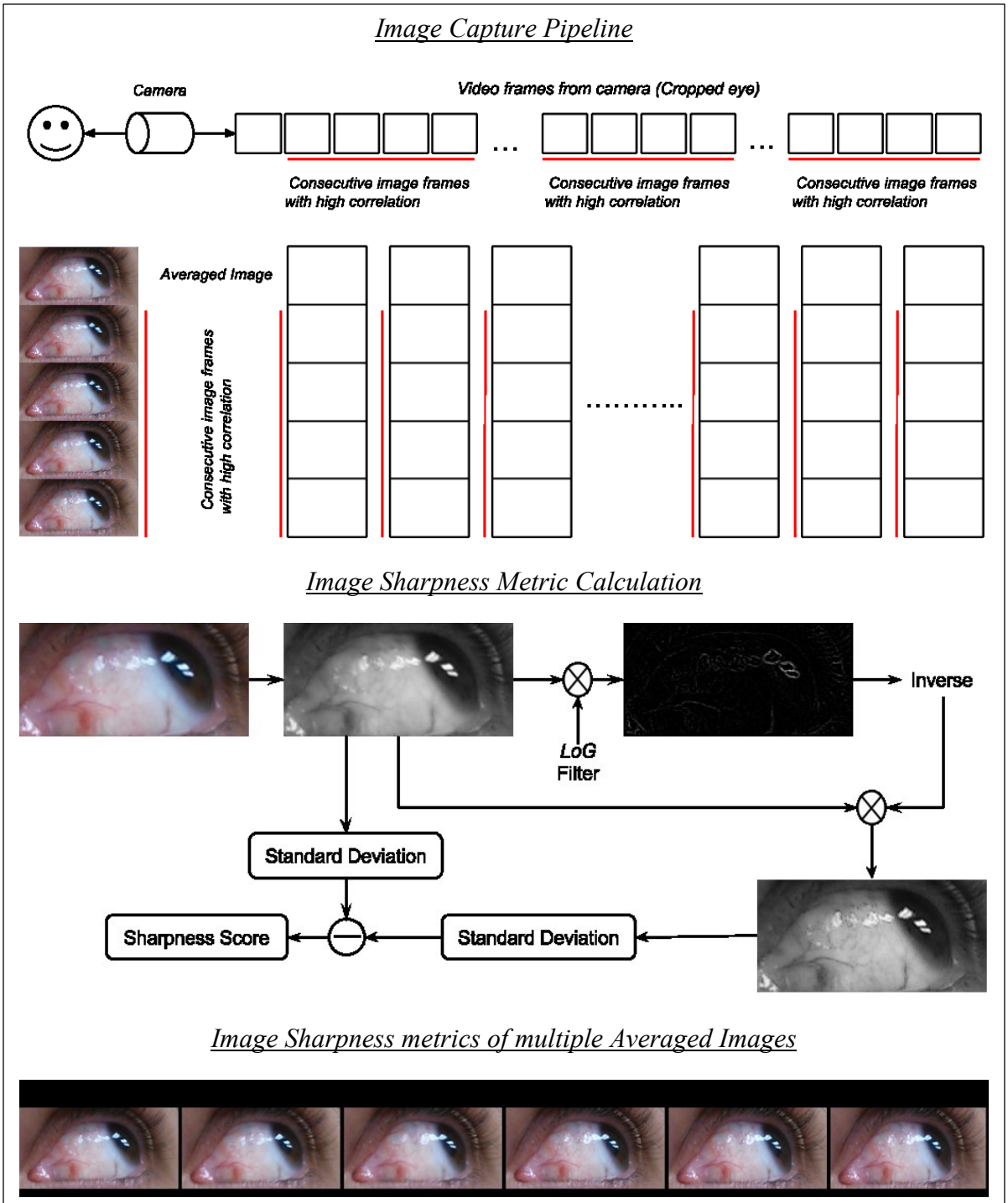

Fig. 12. (Row wise): Image capture pipeline describing the procedure used to acquire images, Flowchart of measuring sharpness metric for sorting acquired images, Sample images with corresponding sharpness metric

4.2. Region of Interest Segmentation

Segmenting the scleral region from eye crops is a very challenging yet critical step for performance of the biometric system. Under or over segmentation of ROI can lead to unwanted regions being matched, at times creating a false accept. Segmentation has been a challenging task for many years and will be for years to come when it comes to unconstrained image capture environments. Although a prior knowledge of what to segment is available, the regions of interest look differently under different scenarios. Since, the spatial resolution of DB1 and DB2 are different, different segmentation algorithms are employed. Images in DB3 are based on looking straight gaze, therefore requiring a different segmentation algorithm than those being employed for DB1 and DB2.

4.2.1. Segmentation for DB1[3]

DB1 as mentioned is captured using the rear facing camera of iPhone 4s. Inbuilt flash of the device was used as the illumination source. Because of the flash being used, the eyelids and limbic boundary is clearly visible. Any shadows on scleral region from external light source is generally suppressed by the flash. Due to these reasons, the contrast between limbic boundary and upper eyelid is high. However, for lighter pigmented skin tones, the lower eyelids contrast is not distinguishable from scleral region. The segmentation algorithm for DB1 is as follows (Fig. 13(a)):

Step 1: Smoothen the image using a median filter of size 5 to suppress high frequency structures. This is usually done to suppress the edges created using eye vasculatures.

[3] Led by Pavan Tankasala.

Step 2: Perform morphological gray scale reconstruction followed by image subtraction on blue layer of smoothened image (Soille, 1999).

Step 3: Perform morphological opening operation to eliminate any weak boundaries in the image obtained from Step 2. A disk shaped structuring element is selected considering the shape of lower eyelid where most weak boundaries are seen.

Step 4: The resulting image from Step 3 is binarized.

Step 5: Largest blob from the binarized image is extracted leaving all the other smaller blobs. The largest blob is filled with true pixels in case of any holes.

Step 7: Eye corner is estimated using polynomials obtained from partial lower and higher eyelids. A coarse scleral segmentation (fast secondary segmentation algorithm) with smooth edges is used to find the corner of sclera.

Step 6: Convex hull is performed on the largest blob with the corner included to smoothen the boundaries resulting in final scleral region.

Fig. 13(b) shows the example of successful and unsuccessful scleral segmentation cases. As we can see, in case of tight eye crop, the segmentation algorithm performs well. In cases of bad eye crops where excess lightly pigmented skin regions is included, the segmentation algorithm fails. This can be mitigated by observing the spatial location of obtained sclera with respect to other cues such as iris center and adjusting the blob of sclera accordingly. Similarly, other low performing segmentation algorithms such as adaptive thresholding can be used in cascade to vote for accurate scleral region.

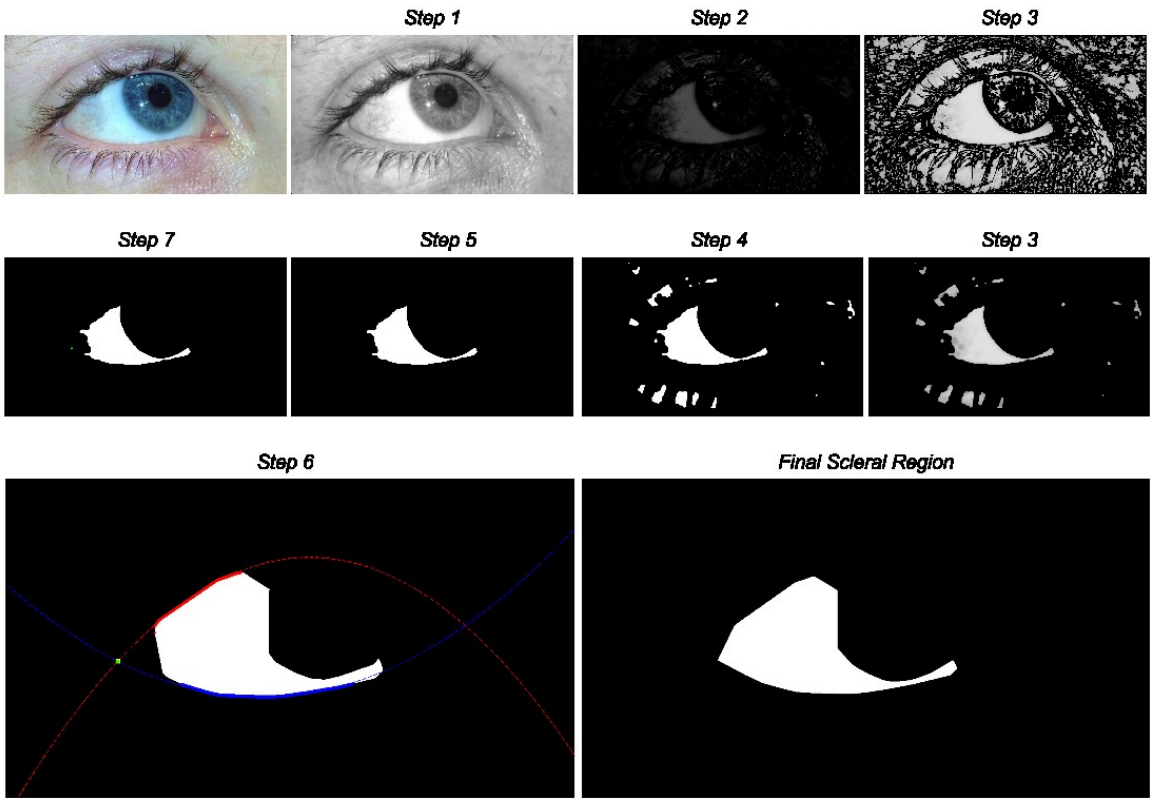

(a)

(b)

Fig. 13. (a) Representation of segmentation in step wise manner. In Step 6, red points (thick) represent upper eyelid points and similarly blue points represent lower eyelid points used for generating polynomial. Red and blue lines represent polynomial fit from corresponding points. Green location represents corner locations obtained from intersecting lower and upper polynomials. (b) Samples of passed and failed segmentation process in *DB1*.

4.2.2. Segmentation for DB2[4]

Images in DB2 are captured without flash and include low resolution images. Segmentation algorithm employed for DB1 doesn't perform well on DB2 for reasons including no distinguishable contrast between eyelids and scleral regions. The segmentation process for DB2 is based off an SDK from EyeVerify and is described in detail in Gottemukkula et al. (2014).

4.3. Quality Assessment

Quality assessment of acquired ROI plays an important role in the performance of the biometric system. A quantitative measure of the quality of the biometric sample indicates its ability to function as a biometric (Bharadwaj et al., 2014). Quality of an eye vasculature biometric can be measured by quantifying its degradation during acquisition and transmission. Some of the most common degradations that are observed at image acquisition are environmental distortions such as noise, blur, illumination and optical distortions that are inherent across various sensors.

Quality assessment of an eye vasculature biometric plays an important role at two crucial stages of biometric recognition process – enrollment and verification. Quality assessment of incoming images in enrollment process is a very important step that directly affects the biometric systems performance. A low quality image in enrollment database may lead to false match when matched across low quality verification image. On the other hand, a high quality image can be used to replace the least quality image in enrollment database

[4] David Hirvonen (Contractor at EyeVerify® LLC.) developed segmentation for low-resolution captures.

(template update process). Also, a measure of quality to reject incoming images in enrollment process will act as a performance metric for acquisition device (Failure to Enroll). In verification process, quality assessment of the acquired biometric sample helps mitigate false matches. Image quality in verification process can be used at various stages. Image quality can be used as a metric to reject verification process bypassing expensive computational time for matching and improving system usability. Image quality can be used as an indicator for parameter selection for image enhancement. Such quality based parameter selection for image enhancement can improve biometric performance over image enhancement based on generic parameters. Quality of the biometric can also act as a predictive measure of the respective biometric sample's ability to match and, in some scenarios can be fused into final match score to improve biometric systems performance (Schmid et al., 2009).

In this work, I propose a quality metric for assessing Eyeprint quality. The proposed method predicts the recognition confidence of the acquired biometric sample by fitting various image quality metrics to a linear model. Also, since the basic characteristics of DB1 and DB2 are different, the design of quality metric for these datasets vary accordingly. The results show that the quality metric helps reduce the false accept rate and false reject rate in both DB1 and DB2 datasets.

4.3.1. Noise in Eyeprint Images

Eyeprint in general suffers from very specific image degradations. Eyeprint recognition for personal authentication is expected to be performed in an uncontrolled, notorious capture environments. In such cases, blur, illumination, glare, and pose play a significant role in corrupting the information in acquired image. Apart from these, compression artefacts such as blocking and ringing effect can also be observed in captured biometric.

4.3.2. Datasets for Quality Metric Design

For designing quality metric for *DB1* and *DB2*, I considered two validation datasets with 30 subjects each. First validation dataset (*VD1*) was obtained using the same sensor used to capture *DB1* and second validation dataset (*VD2*) was obtained using same sensor used to capture *DB2*. Images for each subject in validation dataset were captured in varying lighting environments. It was ensured that all noise aberrations were included in the dataset. Also, images with no noise were also captured to use for enrollments. Enrollment images in *VD1* and *VD2* were manually picked for matching purposes.

4.3.3. Image Quality Metrics

The following image quality metrics were used across both *VD1* and *VD2* to design the final quality score.

Image blur (VD1, VD2):

Image blur is the most common type of degradation that occurs due to improper device focus and eye movement. Front facing camera of most smartphones have fixed focus and a slight movement away from the focal distance during image acquisition results in image blur. So, almost all images in *DB2 FF* (images captured using front facing camera of iPhone 5) have varying degree of blur. In *DB1*, focus is automatically set during the image capture based on eye location and blurry images are least expected. Blur in image causes loss of edge information which is very essential for eye vasculature recognition (Du et al., 2012). Image enhancements correct for focus degradations to a certain extent restoring edge information in images. I use a slightly modified version of cumulative probability of blur detection (CPBD) method to detect the blurriness of the image (Narvekar et al., 2009, 2011).

No-reference CPBD metric combines the edge width method and the concept of "just noticeable blur". Blur estimation begins with using an edge information map obtained from Vascular Point Detection (VPD). Edge information is used to measure the edge width at edge locations. Considering that edge regions provide with most information regarding the blur, we divide the image into 32 X 32 blocks. The block containing more than a number of edges are labelled to be edge blocks. At each location in an edge block width of edge is measured by profiling the gray scale location of edge. A patch of 15 X15 is extracted around each edge pixel. The maximal gradient is calculated in all directions at the edge location in the patch. The normal direction to the maximal gradient is utilized to profile the gray scale pixel values to obtain the edge width. Let e_i denote an edge pixel and $w(e_i)$ denote the corresponding edge width. The probability of blur detection P_{blur} at each pixel can be expressed as

$$P_{blur}(e_i) = 1 - exp^{\left(-\left(\frac{w(e_i)}{w_{JNB}(e_i)}\right)^{\beta}\right)}$$

Where β is a constant value, W_{JNB} is the just noticeable width which is dependent on the local contrast of the edge block. CPBD is estimated as

$$CPBD = P\left(P_{blur} \leq P_{JNB}\right) = \sum_{0}^{P_{JNB}} P(P_{blur})$$

$$CPBD2 = CPBD \Big/ \sum_{0}^{P_{All}} P(P_{blur})$$

Where, $P(P_{blur})$ denotes the probability distribution function at a given P_{blur}.

Fig. 14. Image samples showing various degrees of focus blur.

Illumination and Exposure (VD1, VD2):

Uniform illumination and sufficient exposure play a very important role in quality of acquired biometric. High exposure contaminates the image with glare and low exposure introduces noise in captured image. Similarly, adverse illumination effects the visibility of biometric thereby reducing the biometric system performance. Glare in an image is a consequence of improper illumination or exposure where the image information is saturated. For measuring glare, gamma correction is applied to red, blue and green channels separately and pixels saturated spatially at similar locations are labelled as glare pixels. Although this method is not accurate, it seldom estimates glare pixels accurately.

Fig. 15. Image samples capture under high exposure.

Pose (VD1, VD2):

Pose of the user plays an important role in the area of visible scleral region. Since the user captures their own biometric without supervision, there are a lot of pose variations in the

data. It is therefore necessary to quantify the amount the available sclera in captured biometric. Also, an estimate of blink is calculated using the eye opening.

Area of segmented sclera is measured as a normalized scored between enrollment scleral area and verification scleral area.

$$Available\ Sclera\ (Sc_{Sc}) = \frac{measured\ scleral\ area\ in\ verification}{measured\ scleral\ area\ in\ enrollment}$$

$$Eye\ Opening(Sc_{Eo}) = \frac{measured\ height\ of\ ROI\ in\ verification}{measured\ height\ of\ ROI\ in\ enrollment}$$

Vascularity (VD1, VD2):

Vascularity measures the amount of visible vasculature in the segmented ROI. It is essential to quantify the amount of vasculature to determine if the volunteer has sufficient information to be enrolled. Also, due to various aberrations such as bad illumination, visibility of certain vasculature structures is hampered.

$$V_v = \frac{\sum_v BVM(x,y)}{\sum_v ROI(x,y)}$$

Where, V_v is the vascularity for verification image, BVM is the mask obtained after finding vascular points and ROI is the segmented scleral region. V_E is the vascularity for enrollment image.

$$Vascularity = \frac{V_V}{V_E}$$

Vascularity 1 is based on BVM whereas, Vascularity 2 is based on gabor based vascular detection (Gottemukkula, 2014).

Fig. 16. (Row Wise): Image samples under various poses, Image samples with varying eye opening, Image samples occluded with eyelashes

Compression (VD1, VD2):

Acquired images are generally compressed to lower size to aid in easy transmission and feature extraction. Such compression techniques result in blocking and ringing artifacts in processed biometric image. The features for measuring the blocking artefacts are calculated horizontally and then vertically (Wang et al., 2002). First, we calculate a difference signal along each horizontal line of the image

$$d_h(m,n) = x(m,n+1) - x(m,n), m\forall[1,M]\,, n\forall[1,N-1]$$

M is the total number of rows and *N* is the total number of columns. Blocking artefacts along horizontal direction is measured by:

$$Blockiness\ (B_h) = \frac{1}{M([N/8]-1)}\sum_{i=1}^{M}\sum_{j=1}^{[N/8]-1}|d_h(i,8j)|$$

Apart from blocking, activity in signal is measured using

$$A_h = \frac{1}{7}\left[\frac{8}{M(N-1)}\sum_{i=1}^{M}\sum_{j=1}^{N-1}|d_h(i,j)| - B_h\right]$$

Activity signal along with blocking can provide a measure of blur in the image.

Similarly, vertical blocking artefacts and activity (B_v,A_v) are measured and final blocking and activity metrics are designed as follows (Wang et al., 2002):

$$Blocking\ Artifact\ (B) = \frac{B_h + B_v}{2}$$

$$Activity\ Metric\ (A) = \frac{A_h + A_v}{2}$$

Designing the quality metric

Since the eventual goal of any biometric system is to improve the match performance, it is intuitive that metrics used to measure quality of biometric be linked to the match score. The quality metric of a biometric is designed such that it predicts the recognition performance of the biometric system. There are many different ways to combine the quality metrics based on match score. We use a simple nonlinear regression to fit our quality metrics. Below are two such combinations that provide with most discriminative power to classify good images with bad images in terms of aforementioned quality metrics.

$$Score_{VD1} = 1 + (-0.2973 * A) + (-11.629 * CPBD) + (0.0606 * CPBD2) + (1.5553 * Vascularity1) + (-14.188 * Vascularity2)$$

For VD2 dataset, it is seen that *Vascularity2* alone provides with best discriminative power. It is supported by the fact that visible vasculature is directly related to focus of the image. The better the focus and exposure, better the visibility of vasculature. The threshold to reject any image using $Score_{VD1}$ is below 1.75. Similarly the threshold to reject all images from front facing sensor (VD2) is 0.1.

Fig. 17. (Row Wise): Image, Mask and corresponding Sclera for images that passed quality metric (2.218), Image, Mask and corresponding Sclera for images that failed quality metric (1.704).

Fusion Result

For the purpose of determining good images versus bad images, an initial visual inspection is performed on the complete dataset. Images that are in focus with no noise aberrations were labelled to be good images. Similarly, images with low noise aberrations and high visible vasculature content were labelled as good images. Images contaminated with high noise such as glare, blur and high exposure are labelled into bad images. However, it should be noted that all images that are visually labelled as bad images do not fail recognition process.

On the other hand, image enhancement improves the visibility of vessel like structures, thereby improving the chance of images labelled as bad image to match.

4.3.4. Results

In this section I show the importance of quality assessment for eye vasculature biometrics. It is shown that fitting of multiple scores using a simple linear regression to extract one single score is beneficial for accurate quality assessment. For VD1 it is seen that at 0% FRR the quality metric has 24.2% FAR for a dataset of 579 image dataset. However, the 30% of 110 falsely accepted images are effectively not bad images (Visual mislabeling). It is seen that 13% of images that I claim to be falsely accepted are god images for matching purposes. It is true that the images in a certain group (Ex. 'Bad') after enhancement might alter their spatial content to move to a certain different group (Ex. 'Good'). Due to this reason, 13% of 30% FAR images are good images and should not be counted as FAR's. So, the effective FAR of the system is 21%. It is also evident that the quality metric depends on the features and matching criteria. It is made sure that the quality metric is designed on the best configuration of matching method. For VD2, at 0% FRR, there is 22% FAR observed for a dataset of 320 images. *Vascularity 2* metric was deemed to be the single best quality metric.

Performance of biometric system (eye vasculature) with and without the quality analysis has been tested on two datasets. A number of scenarios combining datasets (*DB1, DB2 FF, DB2 BF*), image enhancement techniques and feature extraction methods can be analyzed to test the quality metrics. However, I test the performance of the designed quality metric on two datasets (*DB1 (150 Subjects, Single gaze, 1 sample)* and *DB2 FF (100 Subjects, Single gaze, 1 sample)*), considering they are captured using two different sensors. I also test the robustness of the quality metric on two different image enhancement methods.

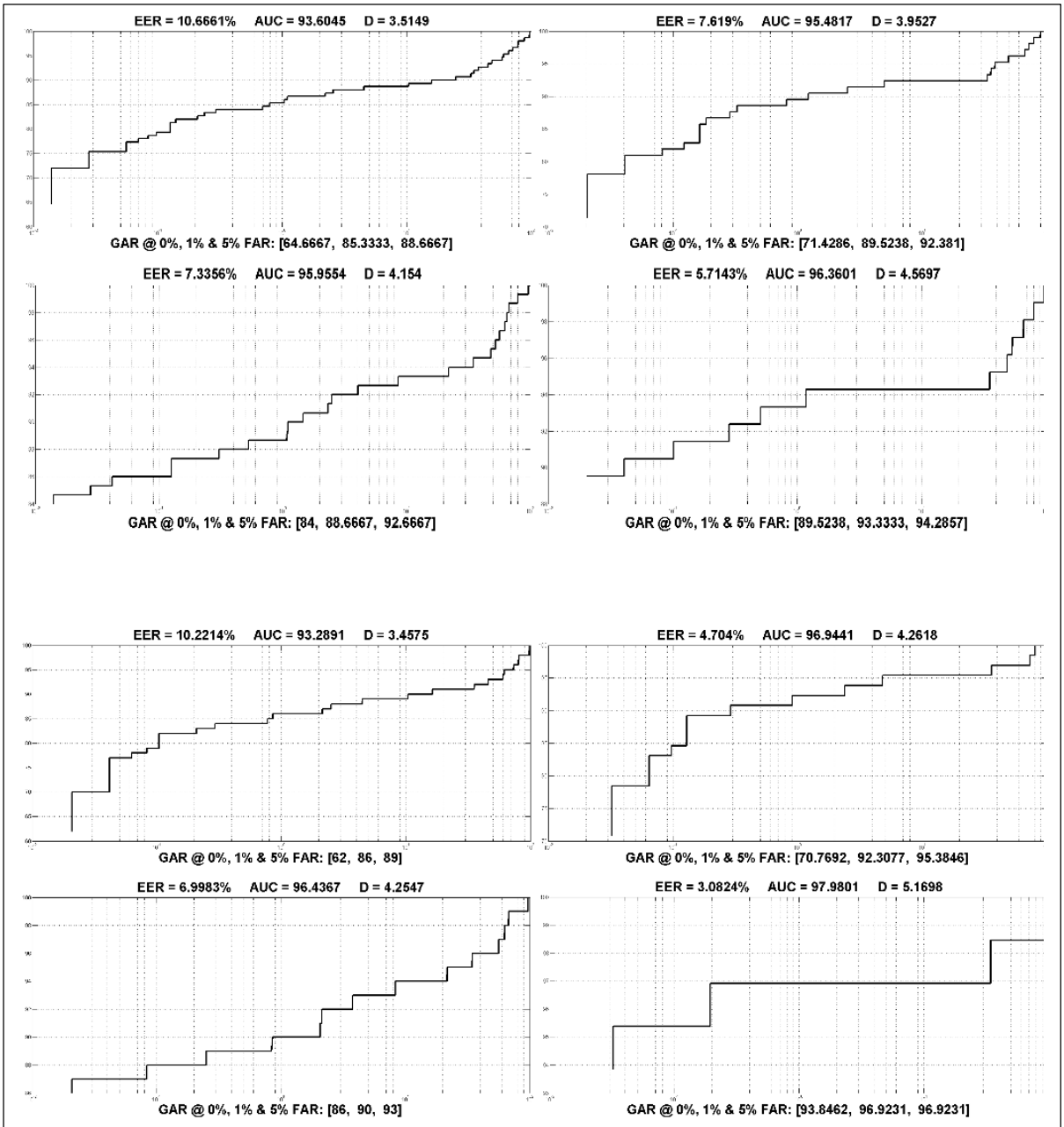

Fig. 18. Column 1 – No quality performance, Column 2 – Quality performance; Row: DB1 Enhancement 1, DB1 Enhancement 2, DB2 Enhancement 1, DB2 Enhancement 2

For the quality metric to be robust, it should perform well with any image enhancement technique.

Table 4: Performance of biometric system with and without quality analysis

Database	Enhancement	Quality	AUC	EER	[1]GAR	[2]GAR	[3]GAR	d
DB1	LoG	No	93.60	10.64	64.67	85.33	88.67	3.51
DB1	LoG	Yes	95.48	7.61	71.43	89.52	92.38	3.95
DB1	Gabor	No	95.96	7.40	84.00	88.67	92.67	4.15
DB1	Gabor	Yes	96.35	5.76	89.52	93.33	94.29	4.57
DB2	LoG	No	96.44	7.05	85.00	90.00	93.00	4.25
DB2	LoG	Yes	97.98	3.10	93.85	96.92	96.92	5.17
DB2	Gabor	No	93.30	10.38	62.00	86.00	89.00	3.46
DB2	Gabor	Yes	96.95	4.70	70.77	92.31	95.38	4.26

[1]GAR – GAR at 0% FAR; [2]GAR – GAR at 1% FAR; [3]GAR – GAR at 5% FAR; d – d-prime

Enhancement techniques used in this tests are described in *Section 4.4*. The combination of feature detectors and feature extraction methods are selected based on the best performance.

4.4. Image Enhancement

Image enhancement plays a crucial role in biometric system performance. Image enhancement is a process of modifying the image such that the modified image enhances the performance of the biometric system. It should be observed that image enhancement algorithms are closely tied to feature extraction algorithms. Enhancement algorithms modify

the statistics the image patches in a linear or non-linear fashion based on the algorithm. These changes in turn affect the features that are derived from the local image patches. So, it becomes important to choose a right image enhancement algorithm based on feature extraction algorithm or vice versa depending on biometric system performance. Two different image enhancement methods were developed for use with two different databases (*DB2, and DB3*). For *DB1*, I adopted an existing algorithm.

For *DB1*, we use contrast limited adaptive histogram equalization algorithm (CLAHE). In DB1, the scleral regions are in focus and the contrast between vasculature and sclera in green layer of RGB image is high. CLAHE operates within small regions to enhance the contrast such that the histogram of the output approximately matches the histogram specified by a flat histogram distribution (Zuiderveld, 1994).

In *DB2*, the images are captured without external flash. Also, a part of *DB2, DB2 FF* is captured using front facing camera of a smartphone. Since the image in process is averaged over multiple frames, there is certain level of smoothness that is observed. A simple contrast enhancing algorithm enhances the information and noise at the same rate. So, an image enhancement technique specific to eye vasculature is used for *DB2 FF* and *DB2 BF*.

For *DB2 BF* I use Gabor based eye vein enhancement. This method is a direct adoption from work by Gottemukkula (Gottemukkula, 2014). I use even Gabor filters to produce a filter which is in turn used to enhance vein like structures in scleral region. An even Gabor filter can be derived using:

$$G_{even}(x, y, f, \emptyset) = exp\left\{\frac{-1}{2}\left[\frac{x'^2}{\sigma_x^2} + \frac{y'^2}{\sigma_y^2}\right]\right\} \cos(2\pi f x')$$

Scale and orientation of Gabor kernel can be achieved through the following coordinate transformation:

$$x' = xcos(\emptyset) + ysin(\emptyset)$$

$$y' = -xsin(\emptyset) + ycos(\emptyset)$$

where, $\boldsymbol{\sigma}_x$ and $\boldsymbol{\sigma}_y$ define the spread of the Gaussian envelope along x and y-axes respectively, f is the frequency of the modulating sine or cosine, and Ø is the orientation angle of the kernel. I use six orientations for building my filter. Since convolution is additive in nature, I add all my six even Gabor filters to obtain a single filter (*Gabor Enhance Filter*).

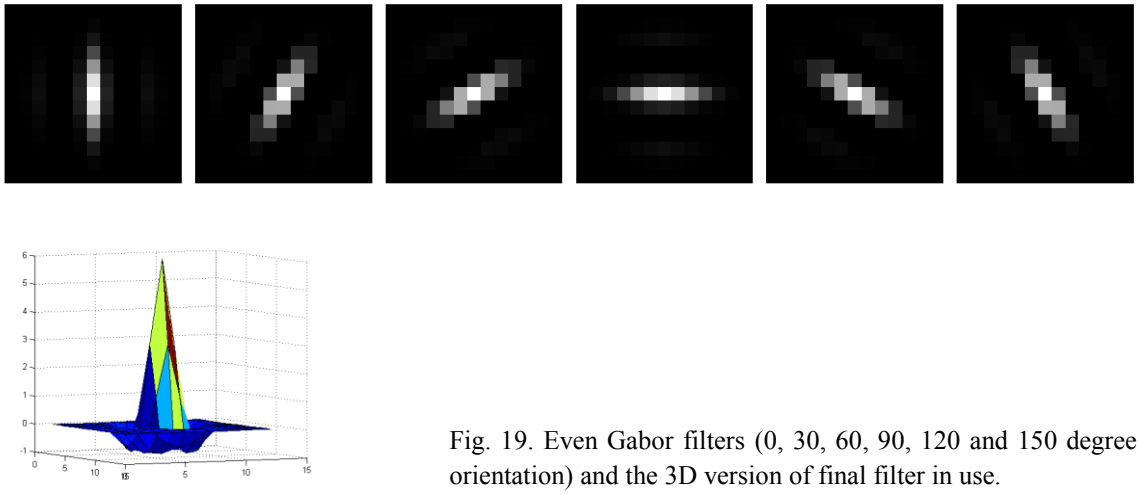

Fig. 19. Even Gabor filters (0, 30, 60, 90, 120 and 150 degree orientation) and the 3D version of final filter in use.

Gabor Enhance Filter is convolved with the green layer of RGB image to detect vascular like structures and enhance them. A CLAHE is applied to the convolved image to enhance the contrast of the image.

In *DB2 FF*, the image that is captured is a result of averaging multiple noisy frames. Due to averaging it is observed that image noise content is suppressed to a certain extent. However, there is a certain level of spatial random noise that is present. I use a Laplacian of Gaussian

(*LoG*) filter to sharpen these noisy low resolution images. Aforementioned *Gabor Enhance Filter* is also used in parallel to *LoG* based enhancement. The reason for using both enhancements in parallel is discussed in later part of this section. *LoG* as the name indicates is a sum of a Gaussian and a Laplacian filter (smoothening summed with sharpening filter). The following procedure is used for enhancing the green layer of RGB image using *LoG* enhancement:

<u>*Step 1:*</u> Convolve Green layer with LoG kernel of size 5x5 and a Gaussian standard deviation (σ) of 0.4, defined by the following equation to obtain the I_{LoG}.

$$LoG(x,y) = -\frac{1}{\pi\sigma^4}\left[1-\frac{x^2+y^2}{2\sigma^2}\right]e^{-\frac{x^2+y^2}{2\sigma^2}}$$

Further, I_{LoG} is derived as follows:

$$I_{LoG} = LoG \otimes I_{AVG}(Green\ layer\ of\ RGB\ image)$$

<u>*Step 2:*</u> Subtract I_{LoG} from the maximum value attainable in the image (1 for a double precision image).

<u>*Step 3:*</u> Each pixel of green layer is multiplied with corresponding pixel of step 2, to obtain a sharpened image ($I_{Sharpened}$).

In Fig. 20, I show the results of the *LoG* based enhancement on a green layer of an averaged image. *LoG* enhanced image is further processed using CLAHE.

As discussed previously, image enhancement methods change the features that are being derived later of the recognition process. It also stands to reason that various enhancement algorithms are dependent on image quality. So, for *DB2 FF*, I use a score fusion based on multi enhancement algorithm. I show that multi enhancement based matching improves biometric

system performance over single enhancement based recognition. The same doesn't stand for *DB2 BF*, so, I use only *Gabor Enhance Filter* for enhancing *DB2 BF* dataset.

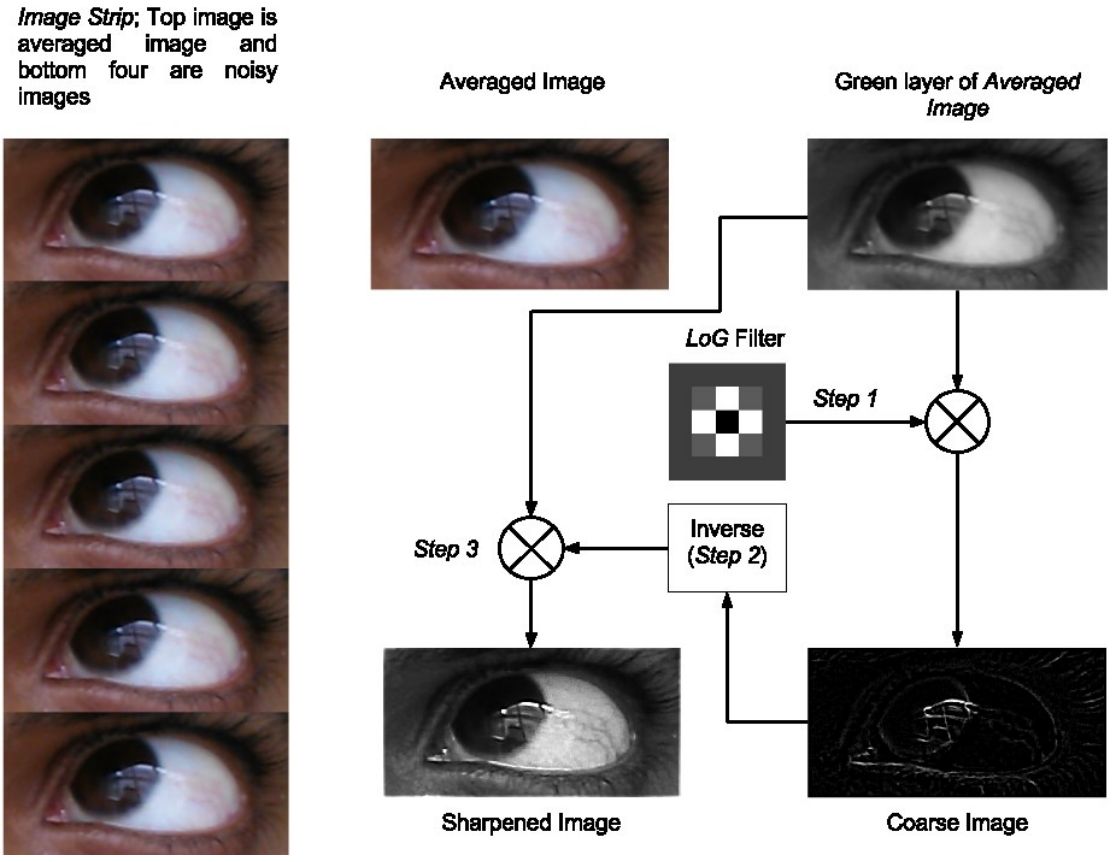

Fig. 20. Image enhancement using LoG filtering method

4.4.1. Results

The effect of image enhancement has been studied on the same dataset the quality analysis was studied. The datasets were filtered using respective image quality metrics. It was observed that Gabor based image enhancement performed best on *DB1*. LoG based image enhancement performed better than Gabor enhancement technique for *DB2 FF*. It is seen that *DB2 FF* has more sensor noise contamination and higher missing information. Gabor enhancement due to the use of even Gabor filters enhances any variations in intensity including noise. Similarly, *LoG* based filtering is also susceptible to noise because of the edge enhancing

Laplacian. However, it is observed that enhancing the noise improves the performance of the system. This might be due to many reasons, the most important being, that images captured are being enhanced spatially creating similar noise textures which are somewhat unique to each subject. Although this scenario has not been reported in literature previously, individual researchers have conformed similar observations on fingerprint recognition systems. Since *LoG* and *Gabor* based enhancements lead to different spatial enhancements (due to filters), it stands to reason that these algorithms provide different features from the same image. So, I fuse the individual scores from respective enhancements at score level to compare the performance of fusion scenario to individual enhancement techniques.

Table 5: Performance of biometric system with various image enhancement techniques

Database	**Enhancement**	**AUC**	**EER**	**[1]GAR**	**[2]GAR**	**[3]GAR**	**d**
DB1	LoG	95.48	7.61	71.43	89.52	92.38	3.95
DB1	*Gabor*	*96.35*	*5.76*	*89.52*	*93.33*	*94.29*	*4.57*
DB1	LoG + Gabor	96.01	6.37	89.52	92.38	93.33	4.39
DB2	LoG	97.98	3.10	93.85	96.92	96.92	5.17
DB2	Gabor	96.95	4.70	70.77	92.31	95.38	4.26
DB2	*LoG + Gabor*	*98.62*	*3.08*	*93.91*	*97.38*	*97.38*	*5.59*

[1]GAR – GAR at 0% FAR; [2]GAR – GAR at 1% FAR; [3]GAR – GAR at 5% FAR; d – d-prime

4.5. Feature Detection and Extraction

In biometrics, local feature detection and extraction have been extensively used in matching scenarios where biometric sample is affected by noise or partially available. Since we ask the user to capture their own biometric, it is expected to see various deformations in biometric samples. Also, it is expected to various noise artifacts such as occlusions, glare and specular reflections. Therefore it is vital to implement robust feature detectors for local matching in our application.

For eye vasculature recognition, I use multiple feature detection and extraction procedures. I later propose a feature detection algorithm which performs better than state of art feature detection algorithms. Feature detection process generally provides the position of the feature with some other possible data which further characterize the feature, such as its scale and orientation. Example of feature detectors are the Harris corner detector (Harris & Stephens, 1988) and the SIFT detector (Lowe, 2004). Feature extraction is a process of calculating meaningful vector around the extracted feature points. A vector containing intensity values around a point is the simplest feature vector. However, feature vectors are generally more complex and carry most valuable information around an extracted point such as gradient orientation histograms (SIFT) etc.

Feature detectors can be classified according to the extracted regions as corner detectors and blob detectors. Corner detector extracts regions in an image with strong intensity variations along at least most of the directions. Corners generally correspond to bifurcations, junctions or ends of line like structures. A blob detector like the name suggests detects blob like regions with uniform intensity values. The main goal of point detectors is to find reputable points irrespective of scale, rotation and noise (Bellavia, 2011).

4.5.1. Corner Detection

The first corner detector was first introduced to Moravec. The algorithm uses a sliding window over a candidate point and measures the intensity variations in all directions. Based on the difference in intensity in certain directions, the candidate point is labelled as corner or edge or flat region. Mathematically, we can represent the above scenarios using the mean of the autocorrelation function.

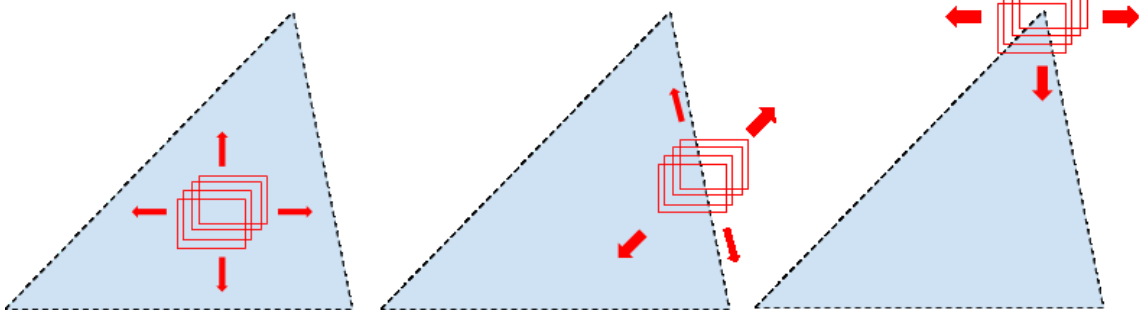

Fig. 21. (Left to Right) Sliding window on a region with no intensity changes in all directions; Sliding window on edges, where intensity changes are maximal in orthogonal directions of the corresponding edge; Intensity variation is maximal in all directions for a corner

$$C(x) = \sum_{x \in R} [I(x_i) - I(x_i - \Delta)]^2$$

where R is the window, x is the center of the window and Δ is the shift in the window. Expanding the second term in the summation window using Taylor expansion followed by some basic mathematical substitutions result in autocorrelation matrix being

$$\mu(I(x)) = \begin{bmatrix} \sum_{x \in R} d_{x_i}^2 & \sum_{x \in R} d_{x_i} d_{y_i} \\ \sum_{x \in R} d_{x_i} d_{y_i} & \sum_{x \in R} d_{y_i}^2 \end{bmatrix}$$

μ represents the autocorrelation matrix of image patch. The autocorrelation matrix is symmetric and has two positive eigenvalues $\lambda 1$, $\lambda 2$. Based on the values of the eigenvalues three important decision can be derived regarding the region of interest.

1. If $\lambda 1 \approx 0$ and $\lambda 2 \approx 0$, the region is flat since there are no relevant intensity variations
2. If $\lambda 1 \gg \lambda 2$ and $\lambda 2 \approx 0$, there is an edge there is an edge along the direction orthogonal to the eigenvector corresponding to $\lambda 1$.
3. If $\lambda 1 \approx \lambda 2$ and $\lambda 1, \lambda 2 \gg 0$, there is a corner where the directions of maximum intensity variation are given by the eigenvectors of μ.

Also, the eigenvalues are invariant to rotation, but, are susceptible to scale variations.

Based on the aforementioned conditions on eigenvalues of autocorrelation function, many corner detections were proposed. Harris and Stephens defined a cornerness function based on the determinant and trace of eigenvalue matrix. They define the determinant (*det*) as the product of eigenvalues and *trace* as the sum of eigenvalues. A cornerness function *H* is defined as

$$H = det(\mu) - \kappa\, trace^2(\mu)$$

'κ' is the linear coefficient which is generally varied between [0.04, 0.06] for the best results (Mikolajczyk & Schmid, 2004). Similar to H, Förstner proposed a cornerness metric (F) based on ratio of *det* and *trace* (Föstner & Gülch, 1987). The metric depends on the eccentricity of the ellipse defined by the autocorrelation function in the corresponding region.

$$F = \frac{det(\mu)}{trace^2(\mu)}$$

$$C = \frac{4 * det(\mu)}{trace^2(\mu)}$$

Where *C* measures the eccentricity of the ellipse defined by the eigenvalues of the autocorrelation function. A candidate point is defined as a corner if *F* and *C* pass a certain threshold. Shi and Tomasi use minimum of the two eigenvalues to obtain the cornerness mask

(Shi & Tomasi, 1993, Tomasi & Kanade, 1991). The final points from the cornerness mask are derived based on the corner values that are greater than a certain threshold.

There are other kinds of corner detectors based on intensity within a certain filter mask. These detectors most certainly do not always detect corners. Because of the region based intensity properties, these detectors always do not detect corners. These corner detectors are generally fast and do not rely on image derivatives. Smallest Univalue Segment Assimilating Nucleus (SUSAN) is one such algorithm which places a circular mask centered on a candidate point and calculates the response using

$$N(x) = \sum_{x_i \in R} e^{\frac{(I(x_i) - I(x))^6}{t}}$$

The response function *N* is processed through a decision function *S* to obtain the final corners.

$$S(x) = f(x) = \begin{cases} th - N(x), & th - N(x) > 0 \\ 0, & otherwise \end{cases}$$

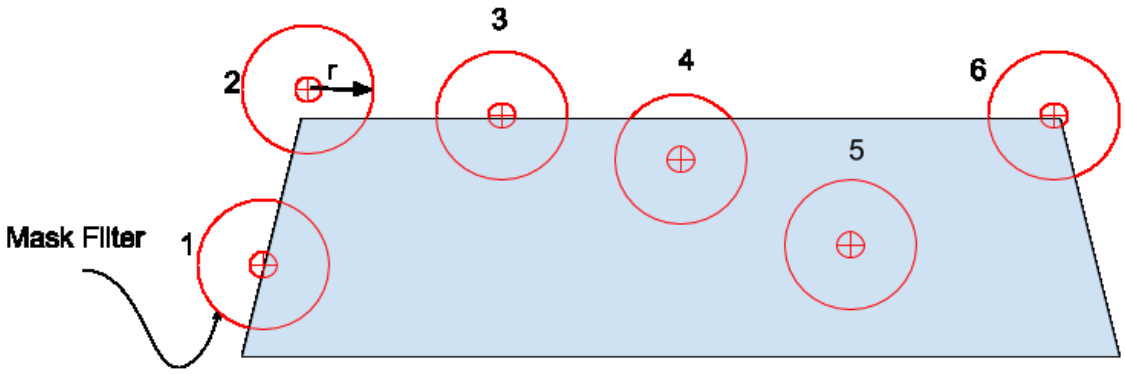

Fig. 22. SUSAN detector output - (2, 4, 5) are determined as flat regions; (1, 3) are determined as edge regions; (6) is determined as corner.

'*th*' is the threshold used to determine the corner from the SUSAN detector response (Smith & Brady, 1997). Similarly, Feature from Accelerated Segment Test (FAST) assigns a candidate point as a corner if a certain predefined continuous points are with an intensity values less than that of point in the center of the kernel mask (Rosten & Drummond, 2006).

Rosten (Rosten et al., 2009) demonstrated that FAST-9 has higher repeatability over other variants of FAST. FAST-ER has been shown to perform the best when the images are noisy, but, the algorithm requires significant training before being applied in real world scenarios.

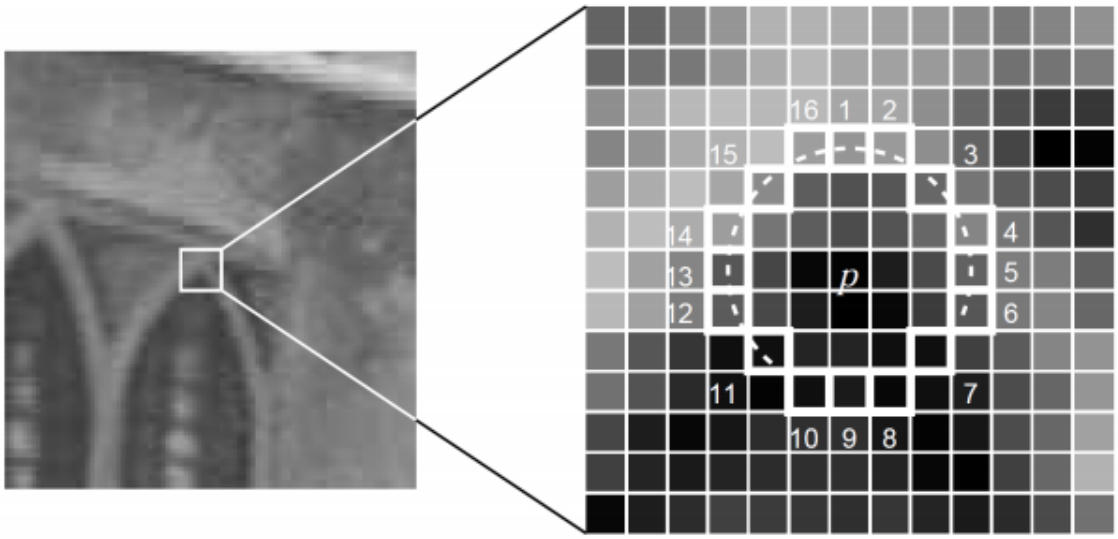

Fig. 23. Example of corner detection on a point *p* using FAST algorithm. (Image from Rosten and Drummond, 2006)

FAST algorithm has been mainly developed to be used in real time application at frame rate such as on smartphone. The FAST corner detection works as follows:

Step 1: Select a candidate point *p*. Let the intensity at *p* be I_p.

Step 2: Consider a Bresnham circle with radius 3. This circle has 16 pixels surrounding *p*.

Step 3: Compare pixels 1, 5, 9, 13 of the circle with I_p. At least three of these points must be greater or less than a certain threshold when subtracted from I_p. If this criteria is not satisfied the algorithm labels the candidate point as non-corner point.

Step 4: If *N* continuous pixels in the circle are greater than or less than a certain threshold *T* to I_p, then the candidate pixel is labelled to be corner point. *N* is 9 in my tests.

Step 5: Repeat the procedure for all candidate points.

FAST algorithm is rotation invariant but is affected by changes in scale.

4.5.2. Blob Detection

As the name indicates, these detectors look for regions that differ in intensity, color or other statistics when compared to their neighbors. Scale Invariant Feature Transform (SIFT) detector is one of the most famous blob detectors (Lowe, 2004). The algorithm uses the Difference of Gaussians (*DoG*) to find interest points in multiple scales. The difference of Gaussians can be seen as an approximation of the Laplacian of Gaussian (*LoG*). The difference of Gaussians can be computed efficiently by smoothing each image octave with different Gaussian kernels and then by subtracting them. SIFT descriptor is rotation and scale invariant, but, is computationally expensive due to *DoG* calculations. Speed-Up Robust Features (SURF) (Bay et al., 2006) was introduced as an improvement over SIFT with respect to computational footprint. SURF extracts features based on the determinant of hessian matrix. For a given Point (x, y) in an image, the Hessian matrix around an image patch is determined as follows:

$$\mathcal{H}(x,\sigma) = \begin{bmatrix} IP \otimes \left(\frac{\partial^2}{\partial x^2}\left(\frac{1}{2\pi\sigma^2}e^{-\frac{x^2+y^2}{2\sigma^2}}\right)\right) & IP \otimes \left(\frac{\partial}{\partial x}\frac{\partial}{\partial y}\left(\frac{1}{2\pi\sigma^2}e^{-\frac{x^2+y^2}{2\sigma^2}}\right)\right) \\ IP \otimes \left(\frac{\partial}{\partial x}\frac{\partial}{\partial y}\left(\frac{1}{2\pi\sigma^2}e^{-\frac{x^2+y^2}{2\sigma^2}}\right)\right) & IP \otimes \left(\frac{\partial^2}{\partial y^2}\left(\frac{1}{2\pi\sigma^2}e^{-\frac{x^2+y^2}{2\sigma^2}}\right)\right) \end{bmatrix}$$

where $\sigma = 1.2$ is the spread of Gaussian. The performance of the algorithm is further enhanced by using integral images and approximated box filters instead of regular images and Gaussian filters respectively. Furthermore, various scales are investigated by incrementing the

size of box filters, known as octaves. A non-minimal suppression algorithm is used to localize the points from various scales (Neubeck & Gool, 2006). Finally, the local maximum using the determinant of Hessian matrices are interpolated in scale and image space (Brown & Lowe, 2002). In my experiments, I have used three octaves (9x9, 15x15 and 21x21). SURF features are both scale and rotation invariant.

Since all the biometric dataset captures are guided through an application in smartphone, I have the flexibility to trigger the response when the capture should be initiated. The trigger response for each dataset is consistent with respect to the eye position on the frame. So, I can confidently say to a certain extent all my image samples have minimal scale aberrations. It is however expected that scale variations might range from 0.5 to 1.5, rotation from -30^0 to 30^0. Apart from scale and rotation other major factor affecting the biometric samples is position of phone (view point variations) which varies from $\pm 30^0$ from ideal position (ideal position being parallel to that of face plane). Since I have limited scale aberrations, I can have my feature detectors to be scale variant. I pick FAST-9 as my second choice of feature detector over other corner detectors because of high reputability and low computational footprint. My first choice of feature detector is Vascular Point Detection (VPD) algorithm that I propose. A rigorous preliminary test amongst all corner detectors for eye vasculature matching revealed that FAST-9 and Harris-Stephens corner detectors performed best. With blob detectors, I use SURF as my first choice of feature detector because of its speed and robust performance compared to other feature detectors.

4.5.3. Vascular Point Detector

Vascular Point detector (VPD) is a curve detecting algorithm that relies on ternary pixels in a window to determine if a candidate point is corner or not. Although numerous point finders have been studied in recent past, most of them are specifically designed for certain application. A few which are robust to multiple applications are either non-resilient to noise or perform worse than VPD. VPD by design detects edges, corners, and line like structures. Since eye vasculature has no definite shape and can be assumed as a combination of multiple curves and lines, VPD succeeds in detecting the continuous pattern. The VPD algorithm is designed as follows:

Step 1: Select a candidate point on the sharpened image and assign multiple windows with varying widths around it. I select two windows (Window 1 and Window 2)

Step 2: Let the candidate pixel be P0 and identify the ternary pixel intensities in both windows.

Step 3: If any of the ternary pixels *are* greater than 250 in intensity value, assign the candidate point as non-corner. The image is expected to be of *uint8* precision (256 is the maximum attainable intensity). The reason being any pixel greater than 250 generally falls into glare category and region around glare are generally of high contrast with least information regarding texture of the surface.

Step 4: Create a counter.

Step 5: Compare the intensity of ternary pixels with the candidate pixel intensity.

Step 6: If the intensity of a ternary pixel is less than that of candidate point by a threshold '*th*', then increment the counter.

Step 7: Loop through all the ternary points and increment the counter based on *Step 5*

Step 8: If the counter is more than 'N', then assign the candidate point to be corner

Fig. 25 shows the steps involved in creating a binary corner mask. A logical mask with all corners assigned to true values is generated by the end of the aforementioned VPD procedure. This mask is known as Binary Vascular Map (*BVM*).

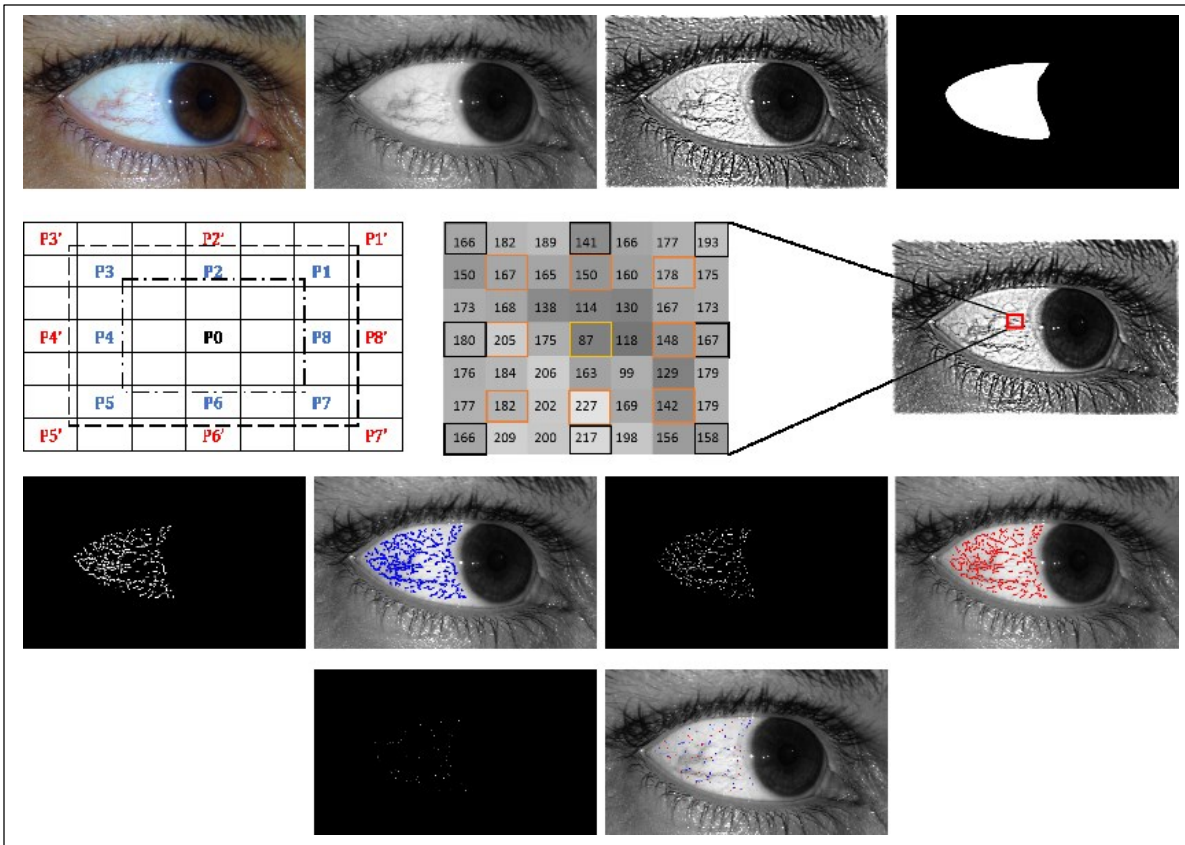

Fig. 24. (Row wise, Left to Right): Original Image, Green layer of Original Image, Sharpened image using image enhancement technique (*LoG*), *Window 1* and *Window 2* used to calculate corner, Example of corner detection using *Window 1* and *Window 2* ternary pixels, *BVM*, *BVM* superimposed in original green layer of image, *thinned BVM*, *thinned BVM* superimposed on green layer of image, *Sparse BVM*, *Sparse BVM* superimposed on green layer of image.

BVM can be mathematically represented as:

$$\mathrm{BVM}(x,y) = \begin{cases} 1 & \sum_i (\,(\mathrm{Pi} - \mathrm{P0}) > \mathrm{th}) \,||\, (\,(\mathrm{Pi'} - \mathrm{P0}) > \mathrm{th}) \geq N \\ 0 & \sum_i (\,(\mathrm{Pi} - \mathrm{P0}) > \mathrm{th}) \,||\, (\,(\mathrm{Pi'} - \mathrm{P0}) > \mathrm{th}) < N \end{cases}$$

BVM generally is affected by noisy regions that are created by vein hallucination or sensor noise. So, BVM is further post processed to obtain a finer vascular map. Connected components in BVM are individually investigated based on the size of the region to be labelled as vein regions. If the connected component is labelled as vein region, the component is Gaussian thinned to obtain a single pixel wide component. This single pixel wide component latches onto the center of vasculature on the original image. Similarly all connected components in BVM are post processed to obtain *thinned BVM.*

However *thinned BVM* reveals the structure of vascular structures and is an imminent threat to the security of the eye vasculature system. A hacker who has the template with the locations of thinned BVM can trace the vascular like structure based off the original image. However, if these *thinned BVM* can be sparse without affecting the performance of the system, then these point detectors can be used in conjunction with other obfuscation technologies. (Gottemukkula 2014). *Sparse BVM* can be obtained by suppressing the thinned BVM pixels in the same neighborhood. *Thinned BVM* is divided into blocks using a M x M window. If more than one corner point is present in thinned BVM bloc, derive the gradient across all the corner points from the original sharpened image. Assign the point with highest gradient as the corner and remove the rest. This way, there is a chance of only one corner point being retained from many in an M x M block.

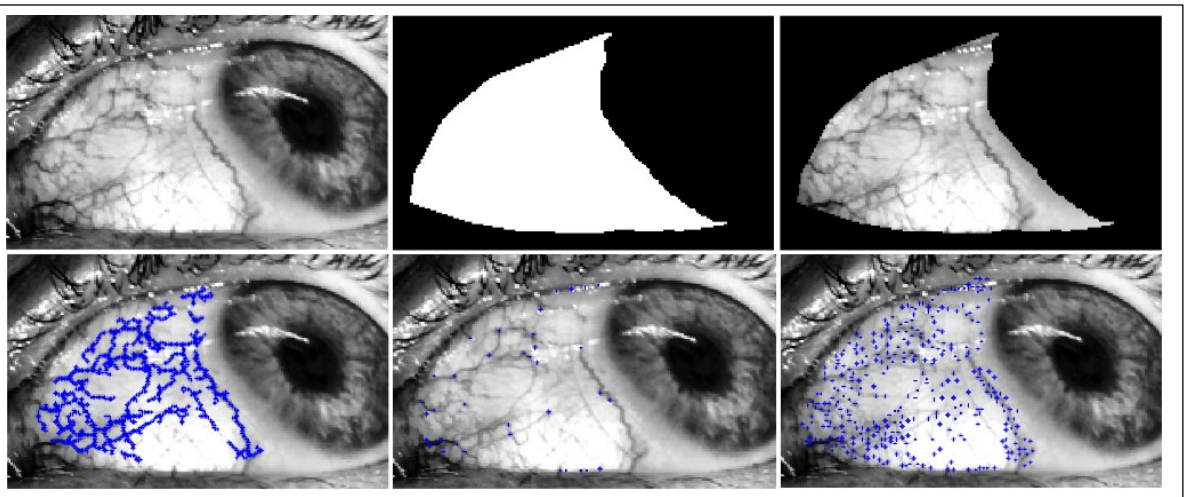

Fig. 25. Enhanced Original Image, Segmented Mask, Sclera Region; Detected VPD Points, Harris Points, FAST Points on sclera

4.5.4. Interest Point Quality

Not all detected interest points carry high information content which is essential for robust performance. Also, the computation speed of a matching method is superlinear to number of interest points and only a certain few interest points lead to optimal performance of application in which they are used. Harris, Laplace, SIFT and SURF detectors of many use non-maximal suppression to eliminate *weak* interest points based on a given neighborhood. The process of non-maximal suppression can be realized in many forms. A typical suppression procedure entails extracting local maxima by performing a grey scale morphological dilation and then finding the subset of corner points that match the dilated image and are also greater than a certain threshold. However, many a times, non-maximal suppression doesn't evenly distribute interest points throughout the image scene, which is potentially non-ideal if images have missing information. An improvement over non-maximal suppression by evenly distributing the key points is observed via adaptive non-maximal suppression. In adaptive non-maximal suppression, for each corner point, the minimum suppression radius is calculated. The minimum suppression radius is the distance from the candidate corner to a different corner

with higher corner strength. The corners are ordered based on their suppression radius and the top 'N' points are selected based on application.

Similarly for FAST points, corner score (V) is determined for each corner in the image. Image is then tiled using m-by-n window and only one corner of multiple present in each window are selected based on highest corner score.

$$V = max \begin{cases} \sum (N_p - p) \; if \; N_p > p \\ \sum (p - N_p) \; if \; p > N_p \end{cases}$$

Where, N_p is the value of pixel on continuous arc calculated around candidate point p.

Although most of the aforementioned point detectors intrinsically look into limited pixels variations in a certain direction to label a candidate point as corner, most of these detectors ignore the variations in surrounding nearby regions which play an important role in feature descriptor encoding. More importantly, quality of the corner is determined based on its variation compared to a certain restricted surrounding pixels.

Non Vascular Point Suppression (NVS) based on feature quality

In this method, I use histogram distributions of smaller regions around corner to detect the strength of the corner to provide feature extraction methods with distinct information. Specifically, I compare the histogram of multiple overlapping patches derived around corner point to determine the strength of point. This algorithm is inspired from the movement of biological eye when looking at an image. Human eye continuously looks for structures with edge information and contrast change to scrutinize, recognize and remember those structures.

It is seen that eye fixates at places which have high contrast changes, indicating that contrast change plays an important role in scene information. The algorithm is designed as follows:

Step 1: Determine the size of region (*R*) that needs to be analyzed to measure the corner strength. Let the size be *M*.

Step 2: Determine the size of local patches (LP) within the region that are used to measure histogram distributions. Let it be *N*. Let the LP centered on center of R be named center patch (CP). Calculate the center coordinate of the local patches as follows

- Center of Region *R* → round to next integer (*M/2,M/2*) → (*c,c*)
- Minimum row value (*indMn*) a LP center can be on → {round to next integer of (*N/2*)}.
- Maximum row value (*indMx*) a LP center can assume–> {*M* – (round to next integer of (*N/2*)) – 1}
- Maximum and Minimum column values a LP center can assume are *indMx* and *indMn*.
- Calculate the indices which in turn are used to calculate center coordinates of LP.
    - Indices are [*indMn*:1: *c*-lower integer of (*N/2*) ; *c*+lower integer of (*N/2*):1:*indMx*].
- Let the indices be [i1,i2,i3,…,in-3,in-2,in-1,in]. The center coordinates then would be
    - For vertical direction → [(i1,c), (i2,c), (i3,c), ….,(in,c)]
    - For horizontal direction → [(c,i1), (c,i2), (c,i3), ….,(c,in)]

- For diagonal directions → [(i1,i1),(i2,i2),(i3,i3),….,(in,in)] and [(i1,in),(i2,in-1),(i3,in-2),…,(in,i1)]

Step 3: Calculate histogram distributions for all LP.

Step 4: Subtract the histograms of CP with all calculated LP.

Step 6: For each subtraction, calculate the distribution of pixels based on number of bins being occupied to total available bins. Let us denote this metric as *Sc1*.

Step 7: Derive a combination of band-pass filters based on the distribution of pixels in original image (see band-pass filter derivation). These band-pass filters are used to measure the amount of spurious pixels such as glare against information pixels. Subtracted patches are filtered based on the derived band pass filter and a corner response (*Sc2*) is calculated.

Step 8: Use *Sc1* and *Sc2* in cascade framework. *Sc1* rejects or accepts the point. *Sc2* is used to quantify the corner strength.

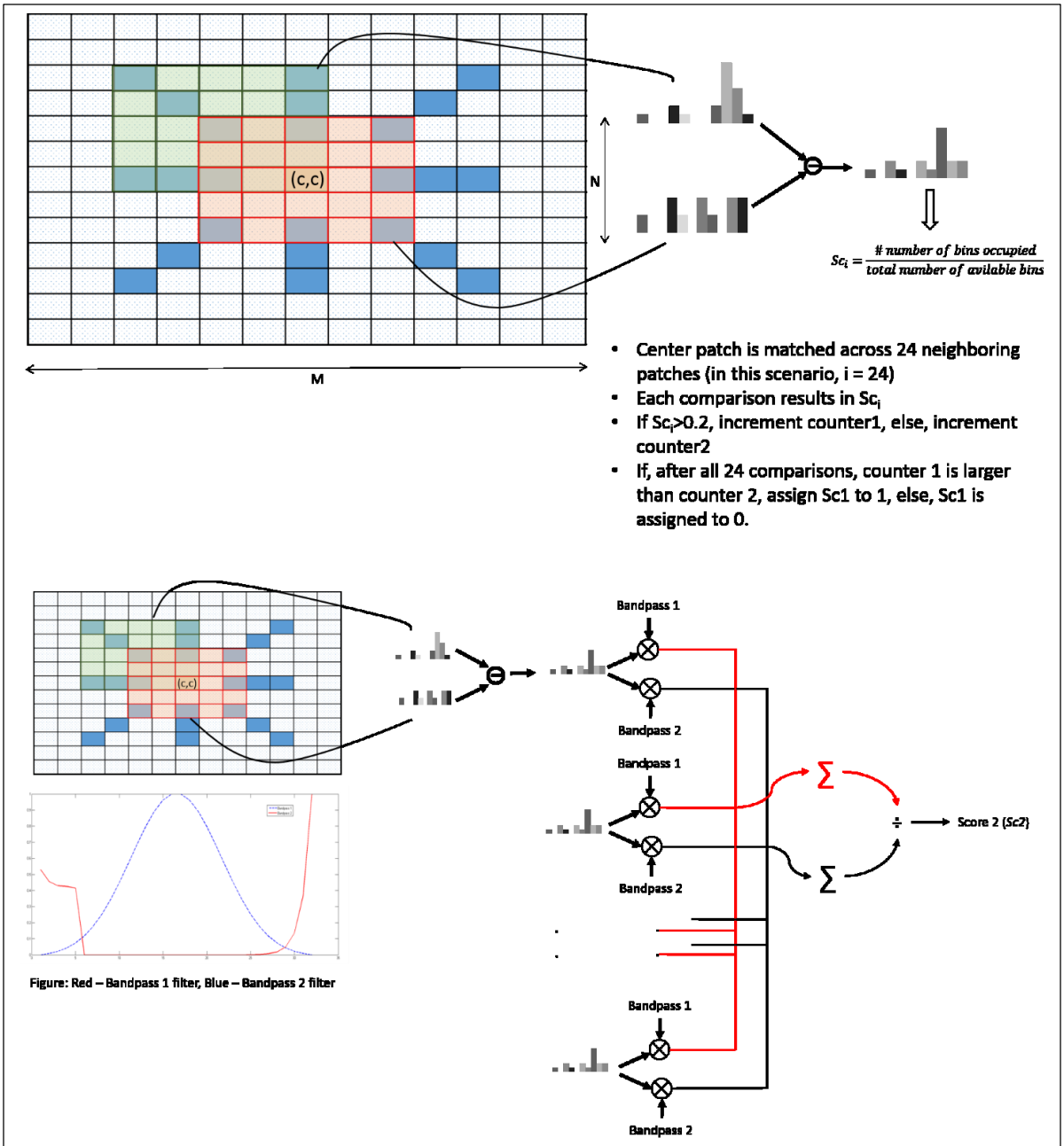

Fig. 26. (Top): Procedure in deriving *Sc1* score. Blue pixels denote the center of *LP* that are being used in calculations. (Bottom): Filter defined by red boundaries represents *Bandpass 2* and Gaussian represents *Bandpass 1*. The image describes steps involved in calculating *Sc2*.

Estimating the band-pass filters

Band-pass filters are dynamically generated based on the complete scleral image statistics. This way there is a prior understanding regarding the distribution of pixels. The band-pass filters are calculated as follows:

Step 1: Extract the green layer of scleral region from RGB image.

Step 2: Derive histogram of the region using 32 bins. Assuming that I have a *uint8* image, 8 pixels are clustered into each bin.

Step 3: Calculate the exponential of inverse normalized histogram.

Step 4: Suppress the exponential by a factor *k*. *k* generally varies from 0.1 to 0.3 and should be tuned based on application.

Step 5: Calculate the response of inverse exponential with integer values ranging from 1 to 32.

Step 6: Concatenate the first 5 elements from Step 4 and remaining from Step 5. This provides with *Bandpass 1*.

Step 7: For *Bandpass 2*, construct a Gaussian with normal distribution of scleral pixels (green channel)

This filter construction process is adaptive to image pixels. If the image is dark, most of the scleral pixels fall near lower tail of the histogram. So, *Bandpass 1*would have a higher repose over *Bandpass 2*. This reduces the score of the point. Similarly, a glare saturated image would

have all its pixels in the upper tail and *Bandpass 2* will have a higher response, eliminating the point with low score.

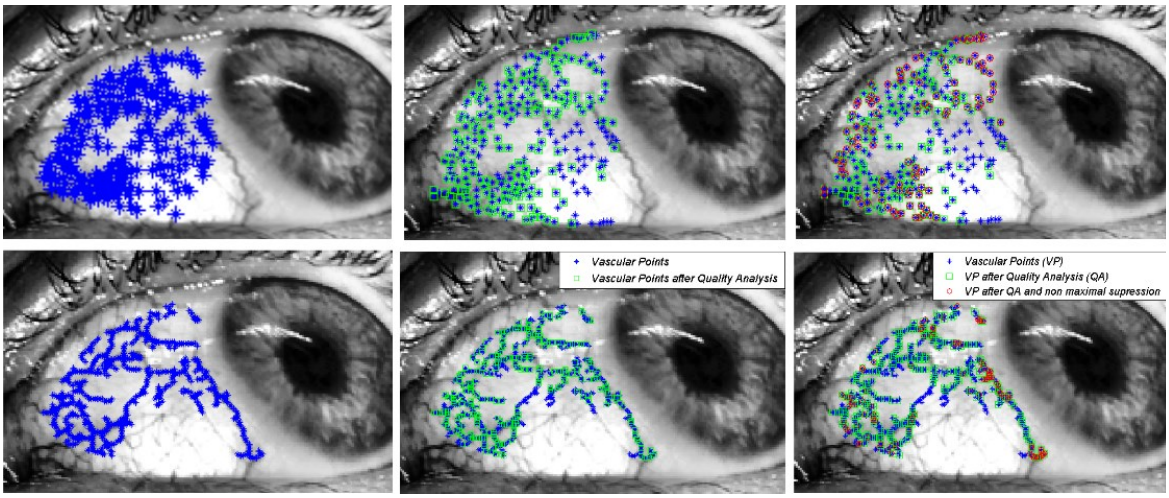

Fig. 27. (Row wise) FAST points, FAST Points (Supressed) after Quality analysis (QA) (red), FAST points after QA and non-maximal suppression (green); VPD points, VPD Points after Quality analysis (QA) (green), VPD points after QA and non-maximal suppression (red)

Point Fusion

It is seen that points extracted from various feature detectors overlap due to similarity in the way these algorithms are designed. So, it is necessary to use minimal subset of points that result in best performance. To do this, I follow the following algorithm:

Step 1: Determine the best individual corner detection method from FAST and VPD. Harris has been omitted due to its contribution towards the number of unique points being detected.

Step 2: Retain all the points from best algorithms recognized from Step 1. Remove all points within 3 pixel distance from retained points.

Step 3: Add the points obtained from blob detector (SURF) to the points from *Step 2*.

4.5.5. Feature Extraction

Feature extraction is a process of deriving discriminative information from around interest points. Feature extraction returns a feature descriptor F_k around a point k which contains information around the point Fk = [fk1,. . ., fkn]. These extracted feature descriptors from enrollments and verifications are later compared using a similarity/dissimilarity function $d(F1,F2)$. Feature descriptors are ideally compact, discriminative and robust to noise. A simple example of feature descriptor is the values of image intensities around an interest point. However, the use of intensities in a patch as descriptor is not a good choice because it has a high dimension, it is very sensitive to small variations and it is very redundant.

Local feature extraction followed by matching has gained considerable interest on object recognition especially with noisy environments and occlusions being prevalent in data capture. Feature descriptors can be approximated into two classes – binary and non-binary (Gottemukkula, 2014). Binary descriptors are fast to compute and robust to image aberration. One of the most commonly used binary descriptors for matching problems are Local Binary Patterns (LBP). LBP's are derived by concatenating the binary responses from comparing the intensity value of the center pixel with its neighbors. Several variations of LBP's have been proposed for various applications. One such LBP variants I use in my tests were first introduced by Gottemukkula (Gottemukkula, 2014). Patterned Histograms of Extended Multi-Radii Local Binary Patterns (PH-EMR-LBP) were first introduced to accommodate the missing information in the vascular content observed in various samples taken at different locations. Patterned Histograms of Extended Multi-Radii Center Symmetric Local Binary Patterns (PH-EMR-CS-LBP) were inspired from Center Symmetric Local Binary Patterns (CS-LBP). PH-EMR-CS-LBP encode the directionality intrinsically and these features are resilient to lack of

spatial information. Both PH-EMR-CS-LBP and PH-EMR-LBP are resilient to noise, rotation, translation and partial occlusions. FREAK (Alahi et al., 2012) describes features around a point by shortlisting 512 high variance features out of all the possible comparisons between the responses from 43-weighted Gaussians. Similarly, one of the most common non-binary feature descriptors are SIFT and SURF amongst various other feature descriptors. Both SURF and SIFT use histograms of local gradients to compute the future descriptor. Histograms of oriented gradients (HOG) calculate the 1D histogram of gradient within the sub-regions (Dalal & Triggs, 2005). Gradient location-orientation histogram (GLOH) increases robustness by computing SIFT features in a log-polar grid (Mikolajczyk & Schmid, 2004).

Based on the work by Gottemukkula (Gottemukkula, 2014) my first choice of feature extractors are PH-EMR-LBP, PH-EMR-CS-LBP and SURF. I also test other state of art detectors such as FREAK against my choice of feature extractors. Since feature extraction methods are not the primary concern of this dissertation, I leave the reader to refer to the respective feature extraction methods for further details.

In our application, since we expect a scale aberration on a scale of -0.5 to +1.5, we use our feature detectors and extractors at multiple scales. For this study, I use two scales: *Scale 0* and *Scale 1*. *Scale 0* is the scale where the image is in its regular size. *Scale 1* is the scale at which the image is down sampled by half. I do not up sample my images since most of the users tend to keep the phone away from them rather than closer. This has also been seen in testing previously where images up sampled provide no added advantage.

4.6. Feature Descriptor Matching and Score Generation

4.6.1. Feature Descriptor Matching

A measure of similarity/dissimilarity between two feature descriptors can be determined based on the feature type (binary or non-binary). The *Minkowski distance* of order *m* is the most common similarity metric used for matching non-binary feature.

$$d_m = \left(\sum_{i=1}^{n} |f1(i) - f2(i)|^m \right)^{1/m}$$

I use the Sum of Squared Distance (SSD) and Euclidean distance as my choice of similarity metric for binary and non-binary features respectively. Various other similarity metrics were used but, *SSD* performed better than the rest.

Enrollment feature (E_f) is matched with verification feature (V_f) using SSD by:

$$SSD = \sum_{n=1}^{N} \left(E_f(n) - V_f(n) \right)^2$$

Where, *N* is the length of respective descriptor (PH-EMR-LBP = 512, PH-EMR-CS-LBP = 144 and SURF = 64). When an enrollment feature matches against the verification feature, they are labelled as *Matched-Point-Pair*. Similarly *Matched-Point-Pairs* are derived after matched all verification features are matched against enrollment features. The process of deriving *Matched-Point-Pairs* is as follows

1. Find similarity (*SSD*) between all verification features against enrollment features.
2. For each verification feature match it against all enrollment features.
3. If the condition below suffices, then assign the feature V_{fi} and E_{fj} as a *Matched-Point-Pair*. E_{fj} is the closest first match to V_{fi}, whereas E_{fk} is the second closest match to V_{fi}.

$$\frac{SSD(V_{fi}, E_{fj})}{SSD(V_{fi}, E_{fk})} < Threshold$$

This method is known as nearest neighbor distance matcher (NNDM). It is seen that NNDM performed better than nearest neighbor (NN) when the dataset is affected by noise. NN is shown to better over *Threshold Matcher*, which considers a pair to match if their *SSD* exceeds a certain threshold.

4. Calculate *Step 3* for all three features.
5. Sum the *SSD* for a *Matched-Point-Pair* across all three feature descriptors.
6. Continue *Step 2* to *Step 5* until all *Matched-Point-Pairs* are derived.

Nearest Neighbor (*NN*) matcher selects the closest match below a certain threshold while reject all other matches. This leads to less false matches. *NNDM* matcher improves over *NN* matcher by additionally penalizing the descriptors which have many similar matches (due to noise), i.e., the distance to the nearest neighbor is comparable to the distances to other descriptors.

As described by Gottemukkula in his work we end up with 2 sets of *Matched-Point-Pairs* when a single enrollment image is matched with a single verification image. In summary, we have the following *Matched-Point-Pairs*:

1. Matched-Point-Pairs at *Scale 0*.

2. Matched-Point-Pairs at *Scale 1*.

As one can argue the process of detecting *Matched-Point-Pairs* can be computed in many ways leading to better performance, I ended up with the particular method after rigorous testing.

In matching vascular structures, it is repeatedly seen that features around the veins look similar when extracted in a small neighborhood. So, it is expected to see a number of false matches in the *Matched-Point-Pairs.* So, I employ an outlier rejection process (RANSAC) to remove any false matches from the *Matched-Point-Pairs*.

4.6.2. Outlier Detection

In performing outlier rejection, a homography between enrollment and verification biometric sample is assumed. Any verification point after being transformed onto enrollment sample using the assumed homography falls away from corresponding enrollment point beyond a certain threshold, the corresponding *Matched-Point-Pair* is labeled as an outlier. It is assumed that a genuine match has significantly lower outliers compared to imposter match. Random Sample Consensus (RANSAC) algorithm (Fischler & Bolles, 1981) is applied to solve related problems in prior literature (Torr & Murray, 1997; Zhang, 1997). RANSAC is an iterative statistical process that randomly samples a subset of matched point correspondences within the *Matched-Point-Pairs*. RANSAC is an iterative statistical process that finds the largest subset points (inliers) within the *Matched-Point-Pairs* that corresponds to the assumed homography, a non-reflective similarity in my study. The optimal inlier pairs will satisfy a given confidence and distance threshold.

4.6.3. Match Score Generation[5]

Match score is generated from the output of outlier rejection process. RANSAC after finding the *inlier* point pairs returns the scale and rotation in form of a transformation matrix. We then use the number of inlier points (*N),* recovered angle (*RA*) and recovered scale (*RS*) for the final score. The final score can be calculated from:

$$Score_{Stage-I} = \frac{log_2(N) * corr(inlier\ point\ pairs)}{(1 + |log_2(RS + \varepsilon)|) * \left(1 + \left(\frac{RA}{\alpha}\right)^2\right)}$$

[5] Reza Derakhshani (Chief scientist at EyeVerify LLC.) developed score generation formula.

where ε is a slight error added to bypass the –Inf value when *RS* is equal to 0. α is set to 0.2 to normalize the *RA*.

4.7. Results

In this section I compare the performance of the proposed feature detector (VPD) against FAST and SURF feature detectors. Constant set of feature detectors are used to compare the performance of the feature detectors (FREAK, SURF, PH-EMR-CS-LBP & PH-EMR-LBP). The rest of the section is divided as follows: *FAST Vs. VPD Comparison*, *DB1* Performance, *DB2 BF* Performance, *and DB2 FF* Performance.

4.7.1. FAST vs. VPD Comparison

Performance of corner detectors was reported on three databases (*DB1, DB2 BF, DB2 FF*). I consider only a single gaze (Left gaze – LLL, RLL) for reporting the performance of the biometric system. A total of 95 subjects were considered for reporting the performance on DB1. 51 subjects were considered for reporting the performance of *DB2 BF*, and, 50 subjects were considered for reporting the performance of *DB2 FF*. It is seen that FAST performs slightly better than VPD for *DB1*. FAST points latch to only vascular like structures just like VPD when the noise content is very low, such as in *DB1*. As the noise content from the sensor increases, it is seen that performance of FAST corner detector drops. It is observed that fusion of FAST and VPD corner points consistently performs better than individual corner detectors. This is expected due to the two complementary methods employed to calculate the corner points. VPD doesn't detect moles and other smaller structures that are present on the surface of the scleral region, whereas, FAST detects these regions.

Generally performance of interest point detectors are reported based on spatial repeatability of points found on a scene when imaged with multitude of aberrations. However most of the datasets used to measure the performance of interest points are synthetically modified with known aberrations with no missing information from scene. However, in our case, there is expected to be missing information and thus, spatial repeatability of points cannot be used as a performance metric to compare interest point detectors. So, I use 'Retention' rate as a performance metric for my interest point detectors. Retention can be described as a ratio of number of points being used for calculating match score to the number of points being detected on original image.

$$Retention = \frac{\begin{array}{c} Number\ of\ points\ (derived\ from\ a\ certain\ Point\ detector) \\ retained\ after\ RANSAC \end{array}}{\begin{array}{c} Number\ of\ points\ \ (derived\ from\ a\ certain\ Point\ detector)\ matched \\ across\ an\ enrollment\ and\ verification \end{array}}$$

It is possible that points detected by *Point Detector A (*in enrollment) be matched with points detected with *Point Detector B* (in verification). This is a cross match scenario. This ratio is very small or negligible in my tests and is not reported.

The best configurations that are seen in Table 6 are used for further tests on respective datasets.

Table 6: Performance of biometric system with various point detectors

Corner Detector	Enhancement	Database	AUC	EER (%)	[1]GAR	[2]GAR	[3]GAR	d	Retention
FAST	Gabor	DB1	99.35	0.59	95.86	100	100	8.92	41%
VPD	Gabor	DB1	96.28	1.18	93.49	98.82	99.41	7.01	32%
FAST+VPD	***Gabor***	***DB1***	***100***	***0.58***	***99.41***	***100***	***100***	***11.02***	***22%+13%***
FAST	Gabor	DB2 BF	98.29	3.39	89.93	95.23	99.2	5.752	23%
VPD	LoG, Gabor	DB2 BF	99.01	1.89	92.23	95.99	99.17	7.25	32%
FAST+VPD	***LoG, Gabor***	***DB2 BF***	***99.99***	***0.59***	***95.29***	***100***	***100***	***8.649***	***18%+21%***
FAST	LoG, Gabor	DB2 FF	92.12	10.91	71.89	84.26	89.57	3.421	19%
VPD	LoG, Gabor	DB2 FF	97.89	6.23	78.86	90.21	94.36	4.86	52%
FAST+VPD	***LoG, Gabor***	***DB2 FF***	***99.95***	***1.14***	***89.04***	***100***	***100***	***5.92***	***46%+13%***

[1]GAR – GAR at 0% FAR; [2]GAR – GAR at 1% FAR; [3]GAR – GAR at 5% FAR; d – d-prime

4.7.2. DB1 Performance

DB1 was captured in two modes (*Video, Still*) as discussed in Section 3.1. It was observed that both modes have their respective advantages and disadvantages in terms of acquisition speed and image quality. Also, there were two environments in which the data was captured – light and dark. In real-world scenario it is possible that the enrollment template was created in a dark environment and verification occurs in a bright environment. So, I perform a cross environment matching. Also, I consider only a single gaze (Left gaze – LLL, RLL) for reporting the performance of the biometric system. A total of 95 subjects were considered for reporting the performance on DB1. Subjects were selected if at least a single sample is available in *Dark* and *Light* environments for both the modes.

All the features described in *Section 4.5.5* were used to measure the performance of the system. The features were matched using the method described in *Section 4.6.1*. Table 7 shows the performance of the biometric system under various lighting scenarios.

Table 7: Performance of biometric system on *DB1*

Database	Case	AUC	EER (%)	[1]GAR	[2]GAR	[3]GAR	d
DB1	1	100	0.58	99.41	100	100	11.02
DB1	2	100	0.056	92.94	100	100	9.855
DB1	3	100	0.007	95.86	100	100	10.96
DB1	4	99.99	0.59	95.29	100	100	8.65
DB1	5	100	0.042	98.21	100	100	9.1
DB1	6	100	0.0358	98.21	100	100	8.65
DB1	7	100	0.0035	98.82	100	100	16.1
DB1	8	99.99	0.095	96.65	100	100	11.99

[1]GAR – GAR at 0% FAR, [2]GAR – GAR at 1% FAR, [3]GAR – GAR at 5% FAR, d – d-prime

Case 1: Long term results (Session 1 vs. Session 2) in *Light* environment using *Still* mode images.

Case 2: Long term results (Session 1 vs. Session 2) in *Light* environment using *Video* mode images.

Case 3: Long term results (Session 1 vs. Session 2) in *Dark* environment using *Still* mode images.

Case 4: Long term results (Session 1 vs. Session 2) in *Dark* environment using *Video* mode images.

Case 5: Session 1 images from *Light* environment vs. Session 2 images from *Dark* environment (*Still* mode)

Case 6: Session 1 images from *Light* environment vs. Session 2 images from *Dark* environment (*Video* mode)

Case 7: Session 1 images from *Light* environment (*Still* mode) vs. Session 2 images from *Light* environment (*Video* mode)

Case 8: Session 1 images from *Dark* environment (*Still* mode) vs. Session 2 images from *Dark* environment (*Video* mode)

Figure 28 is the graphical representation of above results based on the mode of operation. It is evident from the results that the designed biometric system is robust to change in lighting conditions as well as change in modes of operation (*Still* and *Video*). So, for high quality templates, images can be enrolled in *Still* mode where the application captures each image after adjusting focus and white balance. Thus, it is expected that images acquired are in focus and well exposed. For verification purposes, *Video* mode can be employed to expedite the capture process (3X times faster than *Still* mode in capturing images). All the images are resized to 133 pixels in height retaining the aspect ratio of the image before enrollment and verification process. This helps in reducing the computational footprint of all feature detectors and extractors used in the biometric system. This size was determined based on extensive validation.

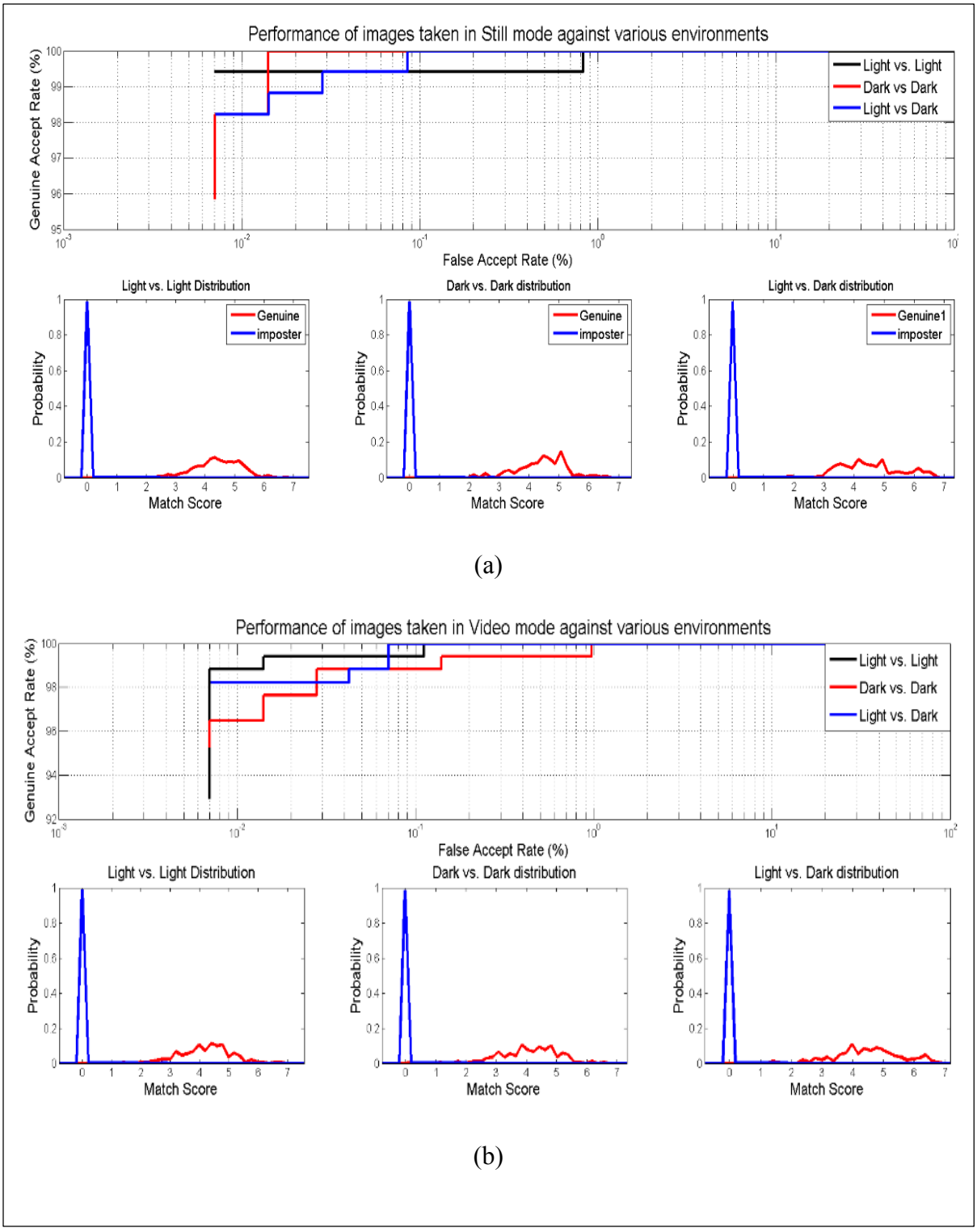
Performance of images taken in Still mode against various environments
Genuine Accept Rate (%)
False Accept Rate (%)
Light vs. Light
Dark vs Dark
Light vs Dark
Light vs. Light Distribution
Dark vs. Dark distribution
Light vs. Dark distribution
Genuine
imposter
Genuine1
Probability
Match Score
(a)
Performance of images taken in Video mode against various environments
Genuine Accept Rate (%)
False Accept Rate (%)
Light vs. Light
Dark vs. Dark
Light vs. Dark
Light vs. Light Distribution
Dark vs. Dark distribution
Light vs. Dark distribution
Probability
Match Score
(b)

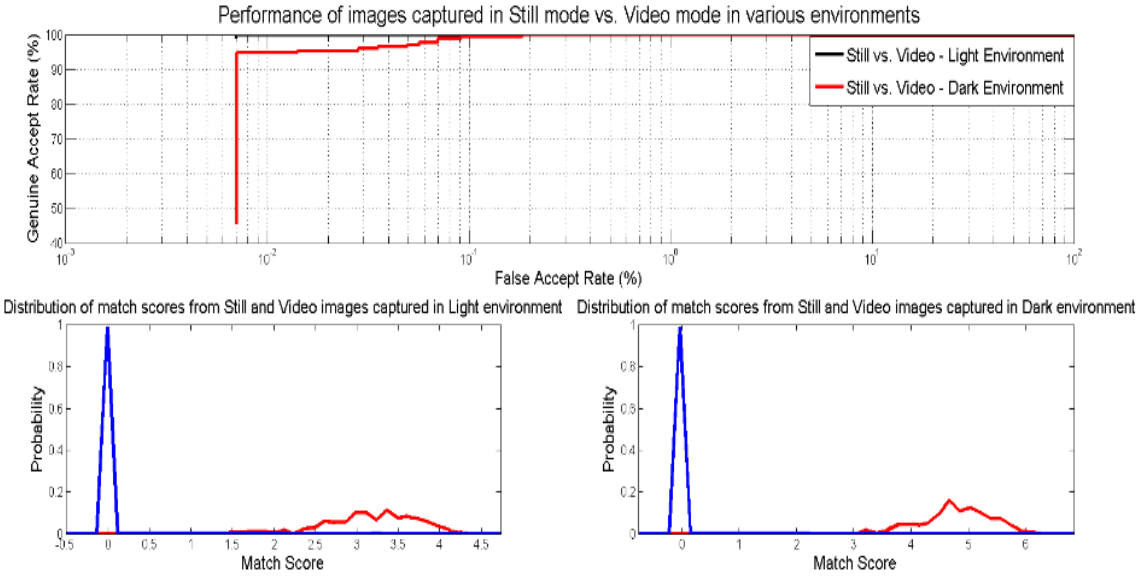

(c)

Fig. 28. (a) Performance of biometric system in *Still* mode capture across various capture environments. (b) Performance of biometric system in *Video* mode capture across various capture environments. (c) Performance of images captured in *Video* mode against *Still* video across various capture environments.

4.7.3. DB2 Performance

DB2 was captured in using both back facing camera (DB2 BF) and front facing camera (DB2 FF). This back facing dataset is similar to DB1 *Video* mode except that the users didn't have any training and the lighting was uncontrolled. The main purpose of DB2 is to compare the performance of the designed biometric system on databases collected using front and rear facing camera. DB2 was captured in regular office (regular room lighting) and outdoor environments (sunlight). I consider only a single gaze (Left gaze – LLL, RLL) for reporting the performance of the biometric system. A total of 42 (out of 51) subjects were considered for reporting the performance on DB2. Additionally, a few subjects were eliminated from final calculations because they didn't have at least 1 sample which passed the quality metric.

Subjects were selected if at least a single sample is available in *Office* and *Outdoor* environments for both the datasets (DB2 *FF* and DB2 *BF*).

All the features described in *Section 4.5.5* were used to measure the performance of the system. The features were matched using the method described in *Section 4.6.1*. Table 8 shows the performance of the biometric system on DB2 in various environments.

Table 8: Performance of biometric system on *DB2*

Database	Case	AUC	EER (%)	[1]GAR	[2]GAR	[3]GAR	d
DB2 BF	1	99.94	0.33	87.10	100	100	5.32
DB2 BF	2	99.99	0.081	93.10	100	100	6.33
DB2 BF	3	99.91	2.32	85.29	97.06	100	5.51
DB2 FF	1	99.93	1.19	79.41	100	100	5.72
DB2 FF	2	99.93	1.46	86.76	97.06	100	5.18
DB2 FF	3	99.88	1.48	86.76	95.59	100	5.24
DB2 FF/BF	4	99.49	2.76	22.58	87.10	100	3.15
DB2 FF/BF	5	99.26	3.62	28.57	80.95	100	3.44

[1]GAR – GAR at 0% FAR, [2]GAR – GAR at 1% FAR, [3]GAR – GAR at 5% FAR, d – d-prime

Case 1: Long term results (Session 1 vs. Session 2) in *Office* environment.

Case 2: Long term results (Session 1 vs. Session 2) in *Outdoor* environment.

Case 3: Session 1 images from *Office* environment vs. Session 2 images from *Outdoor* environment.

Case 4: Session 1 from *Office* environment in *DB2 BF* vs. Session 2 images from *Office* environment in DB2 *FF* (Cross sensor matching)

Case 5: Session 1 from *Outdoor* environment in DB2 *BF* vs. Session 2 images from *Outdoor* environment in DB2 *FF* (Cross sensor matching)

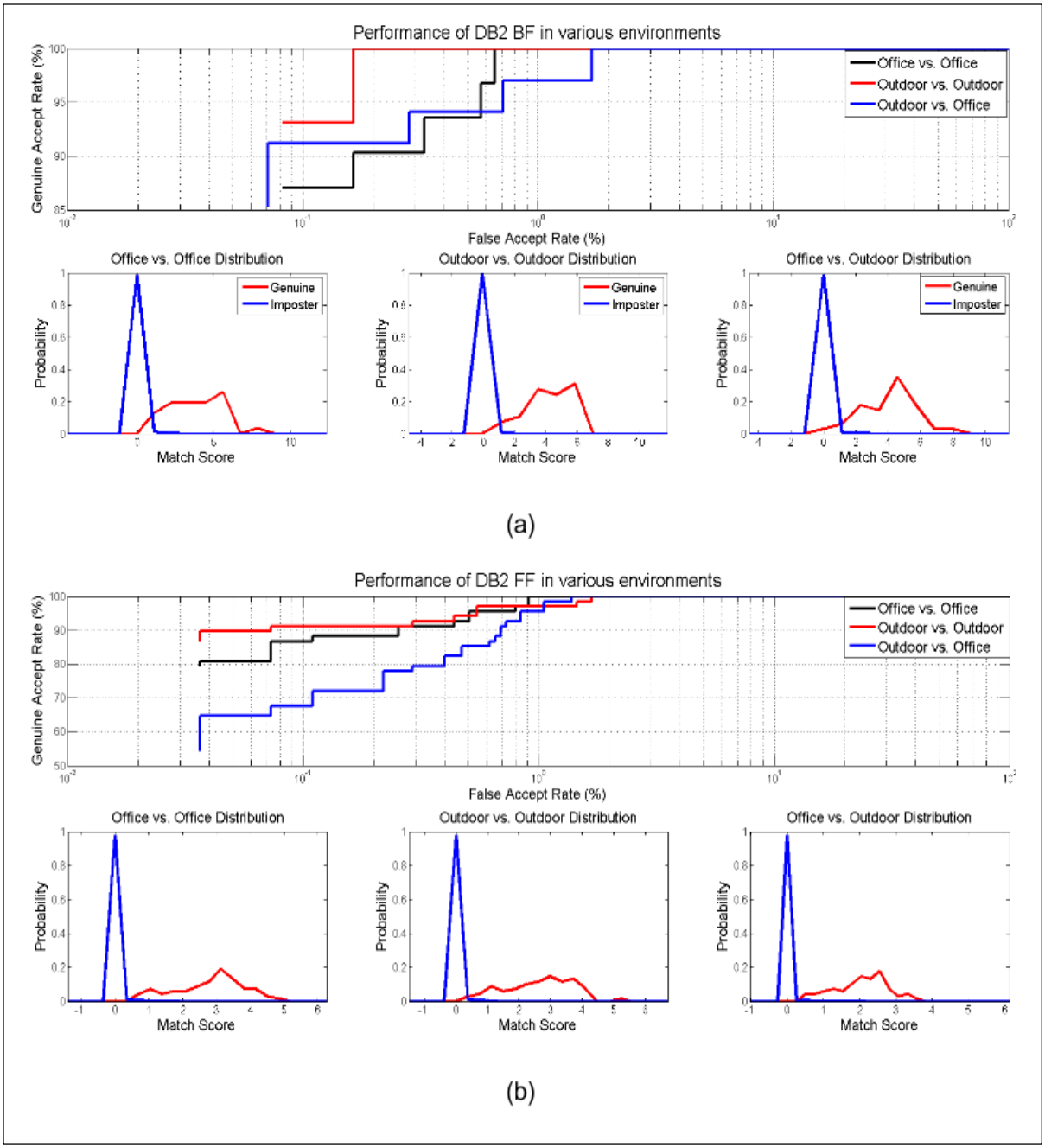

It is expected that *DB2 BF* performs similar to the *DB1 Video* due to the image capture pipeline. However, when there is uncontrolled image capture process it is expected that the performance of the biometric system decreases. The GAR at 1% FAR drops from 92.94% to 87.1%. This is due to some bad quality images being not rejected by quality metric.

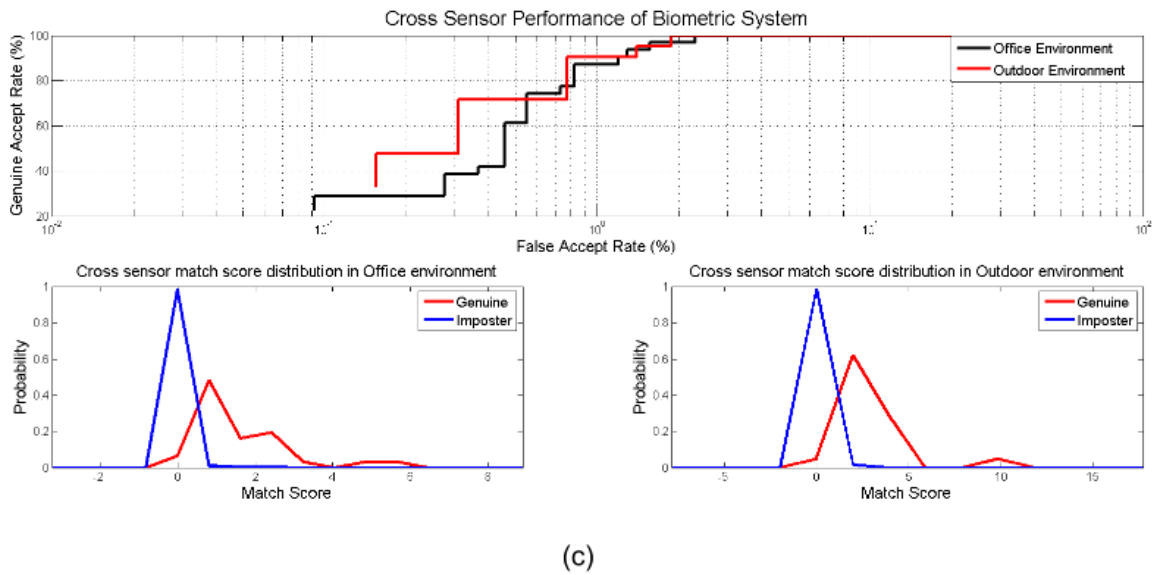

(c)

Fig. 29. (a) Performance of biometric system on *DB2 BF* across various capture environments. (b) Performance of biometric system on *DB2 FF* across various capture environments. (c) Cross sensor performance between rear facing and front facing across various capture environments.

DB2 *FF* performs similarly in all environments tested. The front facing data capture doesn't use any external light, rather, the light from the screen was sufficient to illuminate the scleral region. It is seen that the biometric system underperforms on DB2 *FF* when compared to DB2 *BF*. This is expected due to the lack of image adjustments such as focus and exposure that are available in DB2 *FF*. Apart from the disadvantages in the imaging pipeline for DB2 *FF* and unconstrained data acquisition, the biometric system performs exceptionally well considering that eye vasculature is the only single biometric in study. However, cross sensor comparisons between DB2 *BF* and DB2 *FF* shows a deteriorating performance. When the enrollments were selected from DB2 *BF*, it is seen that the ROI consists of rich texture that is matched against a lower quality image with significantly missing information, resulting in false rejection. So, it concludes from the results that images taken at higher resolution cannot be robustly matched against the verifications from lower quality images.

CHAPTER 5

IRIS RECOGNITION IN VISIBLE WAVELENGH ON SMARTPHONES

Iris as a biometric has been stable despite many new modalities being explored in recent years. Most of the commercially deployed iris biometric systems are based on Daugman's iris recognition model. However, Daugman's approach towards iris recognition requires a constrained environment where the subject needs to adjust his/her face at a certain distance from the capture device, and with the biometric sample being acquired in near-infrared (NIR) spectrum. Irides obtained at infrared wavelengths render most of the texture information regardless of pigmentation while minimizing illumination distortions. A few improvements to Daugman's code were introduced after developing the algorithm, but, the framework of the process has remained constant from its invention: Segmenting the iris, translating the segmented iris into a fixed grid (using a polar transformation), convolving the normalized grid using multiple gabor filters and quantizing the output to one of the four quadrants based on phase information after each convolution, matching the quantized output using hamming distance (Daugman, 2010). The same method has been successfully applied to visible wavelength images achieving perfect accuracies, but, the data didn't include any aberrations (Demirel et. al., 2005). Introduction of noisy visible wavelength iris recognition competition (*NICE-II*) has seen many recognition algorithms being developed for unconstrained iris recognition mainly using modified Daugman's algorithm, zero-crossing and texture analysis methods (NICE II). It was observed that texture analysis based recognition methods performed better than Daugman's code, proposing that local texture based analysis was better equipped to perform when images were noisy and occlusions were expected (Bowyer, 2012).

Local feature descriptor based iris recognition has been first used for irides captured in NIR wavelength (Belcher & Du, 2009, Alonso-Fernandez et al., 2009, Mehrotra et al., 2009). Although these methods have not been completely successful, the implementation of these methods provided encouraging signs in use of the methods. Later on, similar local feature based matching were used for visible wavelength iris recognition. Due to its robust performance, these methodologies were extended onto noisy datasets and results have shown that local matching perform better over traditional Daugman's code. In Daugman's based matching, when converting an iris region to polar coordinates, it is vital that segmentation is very accurate in order to create an iris pattern mapping that is very similar between images of the same eye. Improvements in segmentation has shown an increase in performance but, similar methods have not been useful for non-corporative environments.

Considering the feasibility of using visible wavelength iris images (captured using dSLR) for iris recognition in unconstrained environments, feasibility of iris as a biometric on smartphones has been gaining recent interest. This experimentation has been fueled by publicly available iris databases such as MICHE (Marsico et al., 2014, Raja et. al., 2014, Ross & Othman, 2014). Santos (Santos et al., 2014) use iris information obtained from front facing camera of smartphones to fuse with periocular regions. They use modified Daugman's approach towards matching iris images reporting best EER of 36.6% on 50-subject dataset. Various methods have been proposed based on modified Daugman's code as well as other local feature extraction methodologies on the aforementioned dataset.

In this work, I analyze the performance of iris when captured using a dSLR vs. smartphone sensors. Specifically, I compare the performance of traditional iris matching against local feature matching methods for iris images acquired using multiple imaging sensors. Finally, I

test the performance of designed iris biometric systems on smartphone dataset on publicly available mobile iris database.

5.1. Iris Recognition Methods

5.1.1. Daugman's Iris Recognition (Traditional Method)

I followed the traditional Daugman's method for iris recognition with a few modifications for segmenting iris accurately.

1. Segmentation: For iris segmentation, I applied integro-differential (Daugman, 2010) operator to detect pupil and iris boundaries. Any improper segmentation is then processed through intensity based contour detection algorithm, which removes eye lashes and scleral regions in iris segmentation. Any further incorrect segmentations were manually corrected, as the focus of this work is to evaluate feature extraction and matching across different sensors. Contrast of the red layer was enhanced using contrast limited adaptive histogram equalization (CLAHE) before feature extraction.
2. Image Enhancement: I use illumination normalization function followed by contrast adjustments. For illumination normalization, I use retinex algorithm which has been shown to provide better results over other filtering methods for iris recognition (Land & McCann, 1971, Singh et al., 2007). For contrast enhancement, I use CLAHE algorithm.
3. Iris Normalization: Segmented iris image after image enhancement is mapped onto a constant rectangular grid using polar transformations. This helps in normalizing any scaling aberrations. Also, the pixels on angular axis (x-axis of normalized iris image) of rectangular grid can be shifted in order to compensate rotation artifacts. This

constant rectangular grid on which iris region is mapped is referred to as normalized iris

4. Quantization: 1-D log Gabor filters are applied to rows of the normalized image in the Fourier domain and inverse Fourier transform is applied to the filtered response to result in a complex valued output. The frequency response of a Log-Gabor filter is given as

$$G(f) = exp^{\frac{-\left(log\left(\frac{f}{f_0}\right)\right)^2}{2\left(log\left(\frac{\sigma}{f_0}\right)\right)^2}}$$

where, f_0 is the center frequency and σ is the bandwidth of the filter (Gottemukkula et al., 2012). The phases of the complex output are quantized to 0's and 1's by mapping the phase to one of the four quadrants in the complex plane. This binary representation of normalized iris image is called the 'IrisCode'.

5. Matching: Hamming distance is used to measure the dissimilarity between any two 'IrisCodes'. Only the bits that are false in the iris mask are compared for calculating dissimilarity score. Dissimilarity score (*d*) between two irides A and B, whose corresponding IrisCodes are *codeA* and *codeB*, and whose iris masks are *maskA* and *maskB*, respectively, is given by:

$$Iris\_Score = \frac{\left\|\left(codeA \otimes codeB\right) \cap maskA \cap maskB\right\|}{\left\|maskA \cap maskB\right\|}$$

An 'iris mask' which is of the size of corresponding normalized iris image is created depicting textured iris region with false pixels and noisy regions as true pixels for matching purposes. Figure 30 shows the process of building iris templates in traditional iris recognition process.

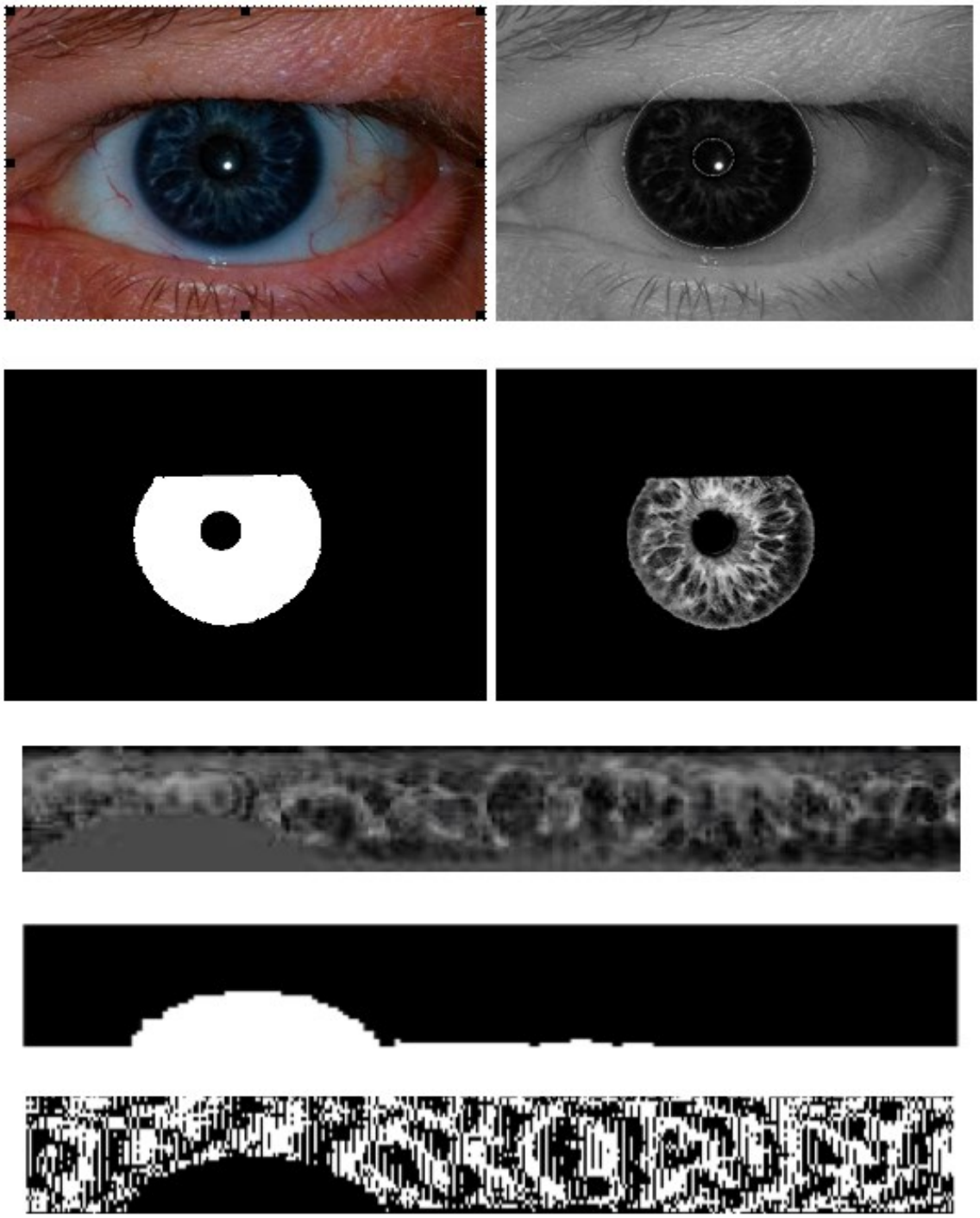

Fig. 30. (Row wise, left to right) Original Image, Extracted limbic and pupil boundaries overlaid on top of gray scale image. Iris mask extracted after removing noise, Enhanced Region of Interest, Normalized Iris region, Noise mask, IrisCode.

5.1.2. Local Feature Based Iris Recognition (Proposed Method)

For local texture matching, I use the same feature detectors that were used in eye vasculature recognition. Since the texture of iris is defined by the crypts (holes), collarette and ciliary area, the use of line detectors (VPD), corner detectors (FAST) and blob detector (SURF) should be sufficient to detect salient points.

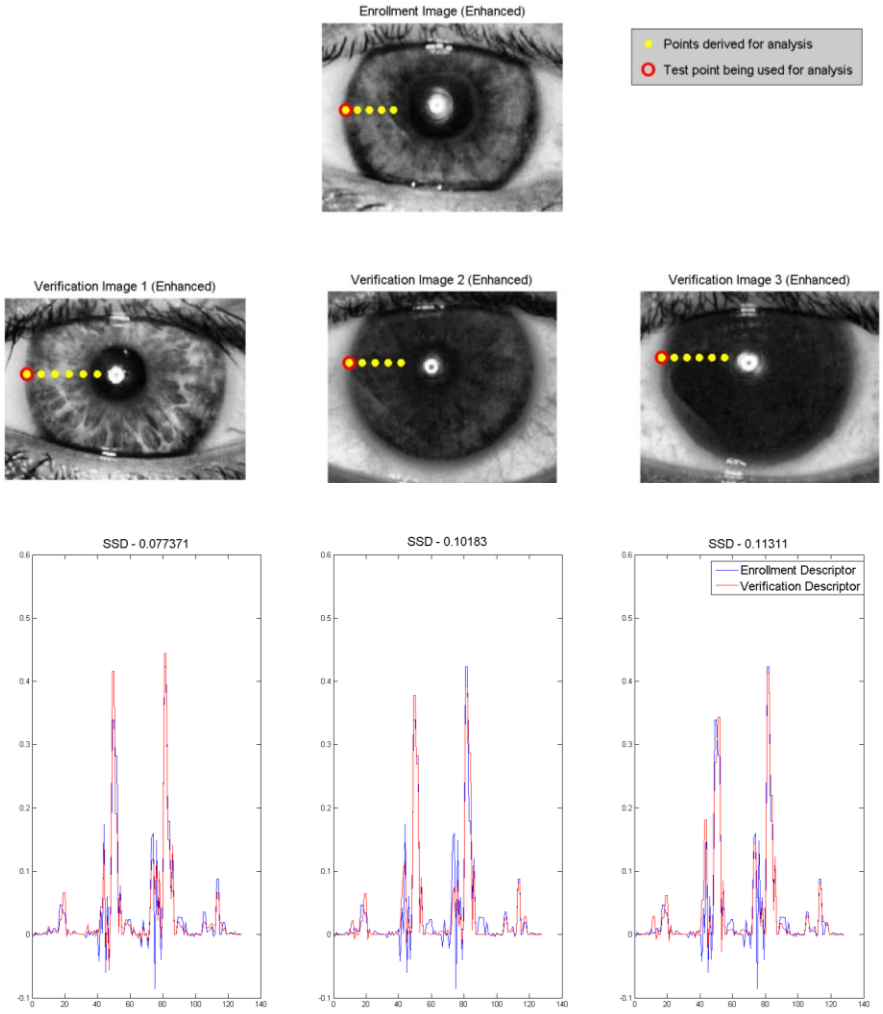

Fig. 31a. (Row wise) Enrollment and Verification Images with corresponding points in test, Surf Descriptors on limbic boundary for enrollment and corresponding imposters. *SSD – Sum of Squared Difference (Similarity Metric)*

Although the texture of iris is significantly different to that of eye vasculature, it is evident that iris is defined by edge information. Since the features used for eye vasculature were designed

to encode edge information, I can use the same features to encode the edge information in iris structure. However, it should be noted that edge density encoded per a certain region varies heavily between sclera and iris. So, I use Fast Retina Keypoint descriptor (FREAK), which uses optimized information sampling for encoding information and Histogram of Gradient (HoG) features.

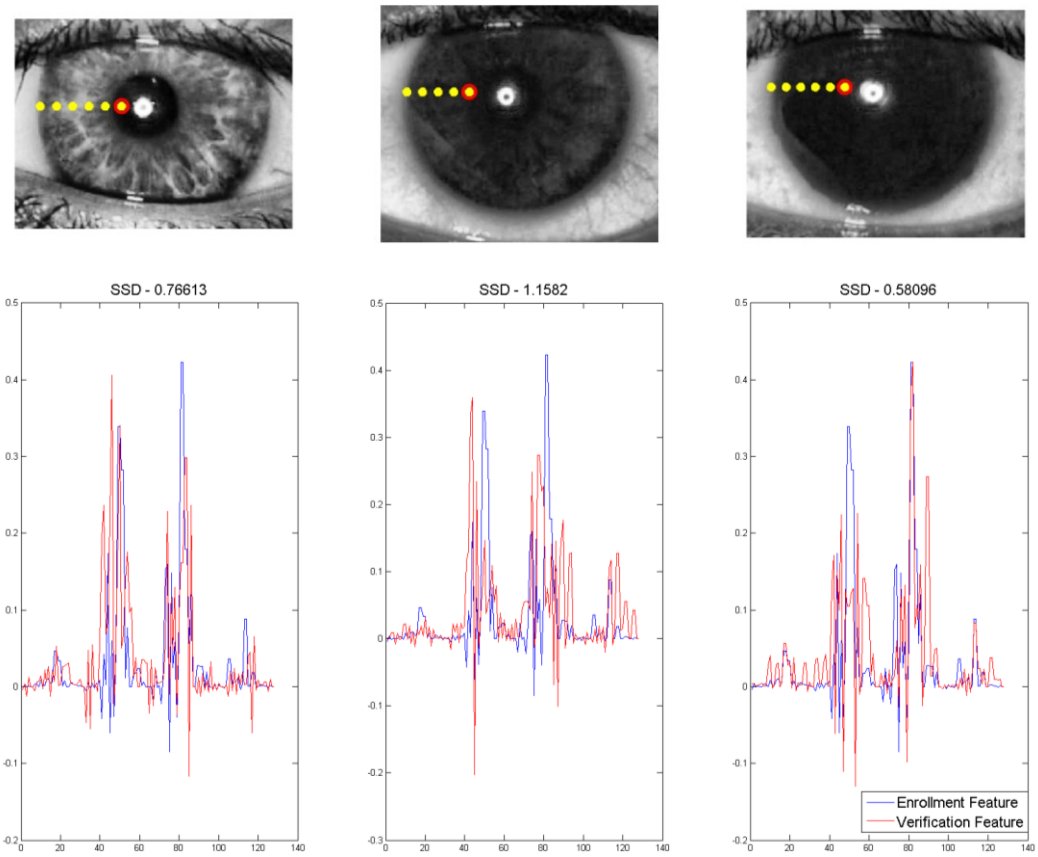

Fig. 31b. (Row wise) Verification Images and corresponding points in test, Surf Descriptors on limbic boundary for enrollment and corresponding imposters. *SSD – Sum of Squared Difference (Similarity Metric)*

Iris biometric is known to carry the distinct information in the central region whereas outer regions towards limbic boundaries are expected to carry redundant information due to high noise probability. This is more prevalent in visible wavelength iris captures since limbic boundary region for all humans looks similar. Similarly, pupil is very hard to detect in

unconstrained environment especially with dark pigmented iris. So, it is important to not consider information close to pupil due to fear of encoding pupil information (dark pixels) into features. For example, in Fig. 31a it is seen that SURF features close to limbic boundary are very similar for various imposter irides. Previous studies using local features have not mitigated the aforementioned problem. I therefore assume that the results can be improved just by excluding the points close to limbic boundary (Fig. 31).

The current iris recognition algorithm I use is as follows:

1. Extract the red layer of RGB image and enhance the layer using retinex algorithm followed by CLAHE.
2. Segment the gray scale image using integro-differential operator.
3. Remove noisy regions in iris.
4. Extract VPD and FAST points on the segmented iris image.
5. Apply quality based suppression and fusion of VPD and FAST points based on *Section 4.5.4*
6. Normalize the verification image based on enrollment image size. (Normalizing the radii of enrollment and verification irides).
7. Remove the points close 5 pixels to iris and pupil boundary.
8. Extract FREAK, HoG, SURF, PH-EMR-LBP, and, PH-EMR-CS-LBP features at all interest points.
9. Match the feature(s) from enrollment and verification templates
10. Remove outliers using RANSAC
11. Calculate the score using the equation described in *Section 4.6.3*

Although I show the comparison of state of art local features for iris recognition, I use FREAK for final calculations based on validation results. Although, I show that FREAK performs best in my results, it should be noted that feature detectors and image enhancement highly influence the performance of feature descriptors. So, my claims are valid as long as similar image enhancement and feature descriptors are used.

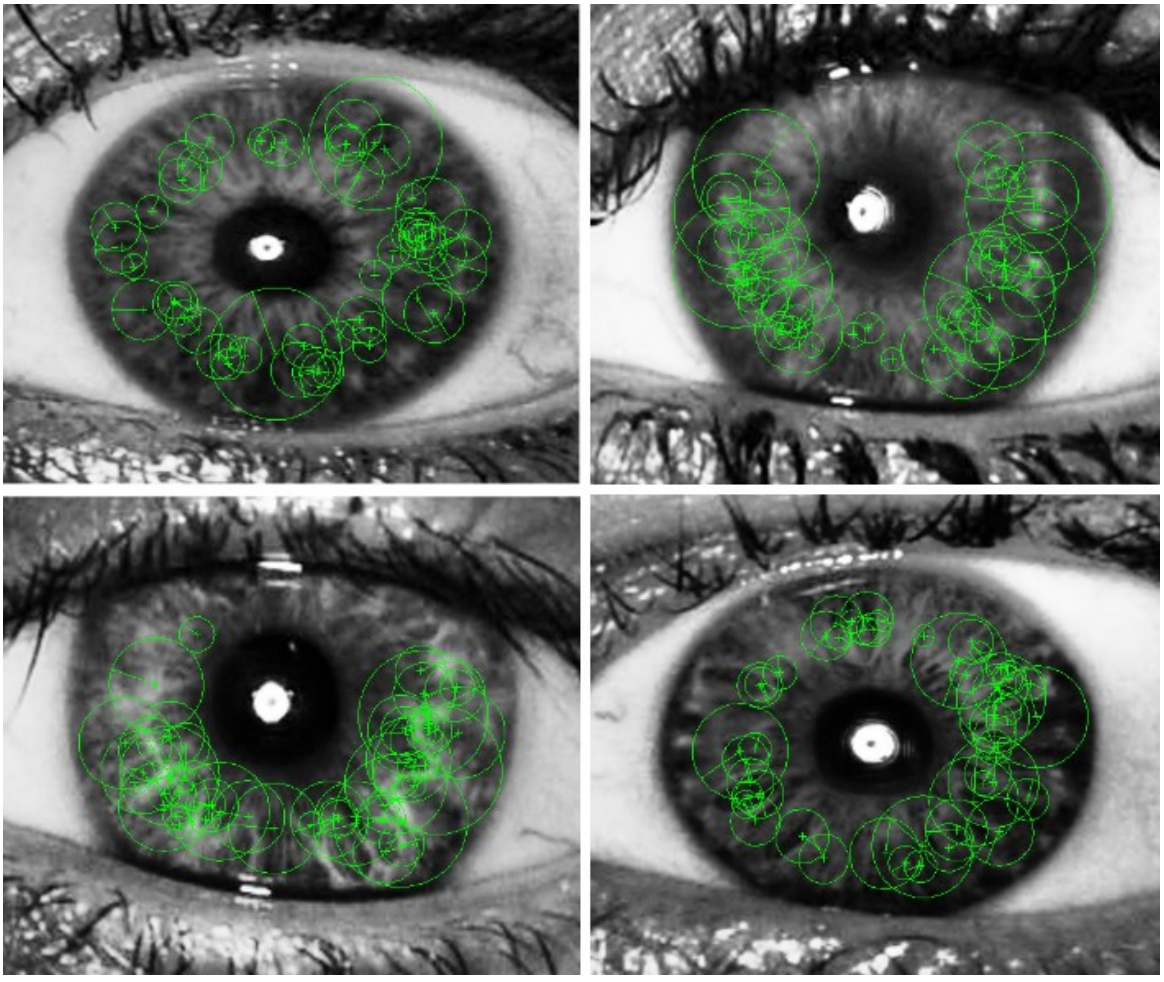

Fig. 32. SURF features constrained to donut excluding points from limbic and pupil boundary.

Figure 33 shows the performance of various feature extraction methods on noisy and non-noisy image datasets.

5.2. Results

In this section, I make a comparison of iris recognition methods when the images are captured via high quality sensors (*DB3 HR* - Nikon D3S) versus low quality sensors (*DB3 LR* - iPhone 4s, Rear Facing Camera) using two iris recognition procedures (*Section 5.1*). For my experiments, I first normalize the iris region (200 pixels) to compensate for varying scales in my datasets. It is expected that images from *DB3 LR* suffer from higher sensor noise when compared to *DB3 HR*. Since *DB3 LR* was captured in regular office environment with no specific constraints on lighting, it is sometimes seen that the images are highly corrupted from noise, especially when the images are captured in low light due to shadow. Majority of the noise from image capture can be grouped into Gaussian noise and shot noise (observed due to statistical quantum fluctuations). Since we use high exposure to capture iris images, majority of the noise is contributed via shot noise.

As we switch from high quality sensors to low quality sensors (rear facing camera to front facing camera), it is seen that images are more corrupted from shot noise especially, due to bad exposure. So, in order to measure the performance of iris biometric system for low quality images, I down sample the images from both *DB3 LR* and *DB3 HR* datasets and synthetically add noise in varying orders. To mimic the shot noise, I use random Poisson distribution in *MATLAB*®. For example, 1st order noisy database represents the down sampled original images synthetically corrupted by Poisson noise. 2nd order noisy database represents 1st order noisy database synthetically corrupted with Poisson noise.

Based on the experiments from noisy iris datasets of *DB3 HR and DB3 LR*, it is seen that local feature based matching is robust to additional noise that might be induced due to capture

environment or sensor change. I further confirm the same from MICHE dataset (publicly available mobile iris dataset).

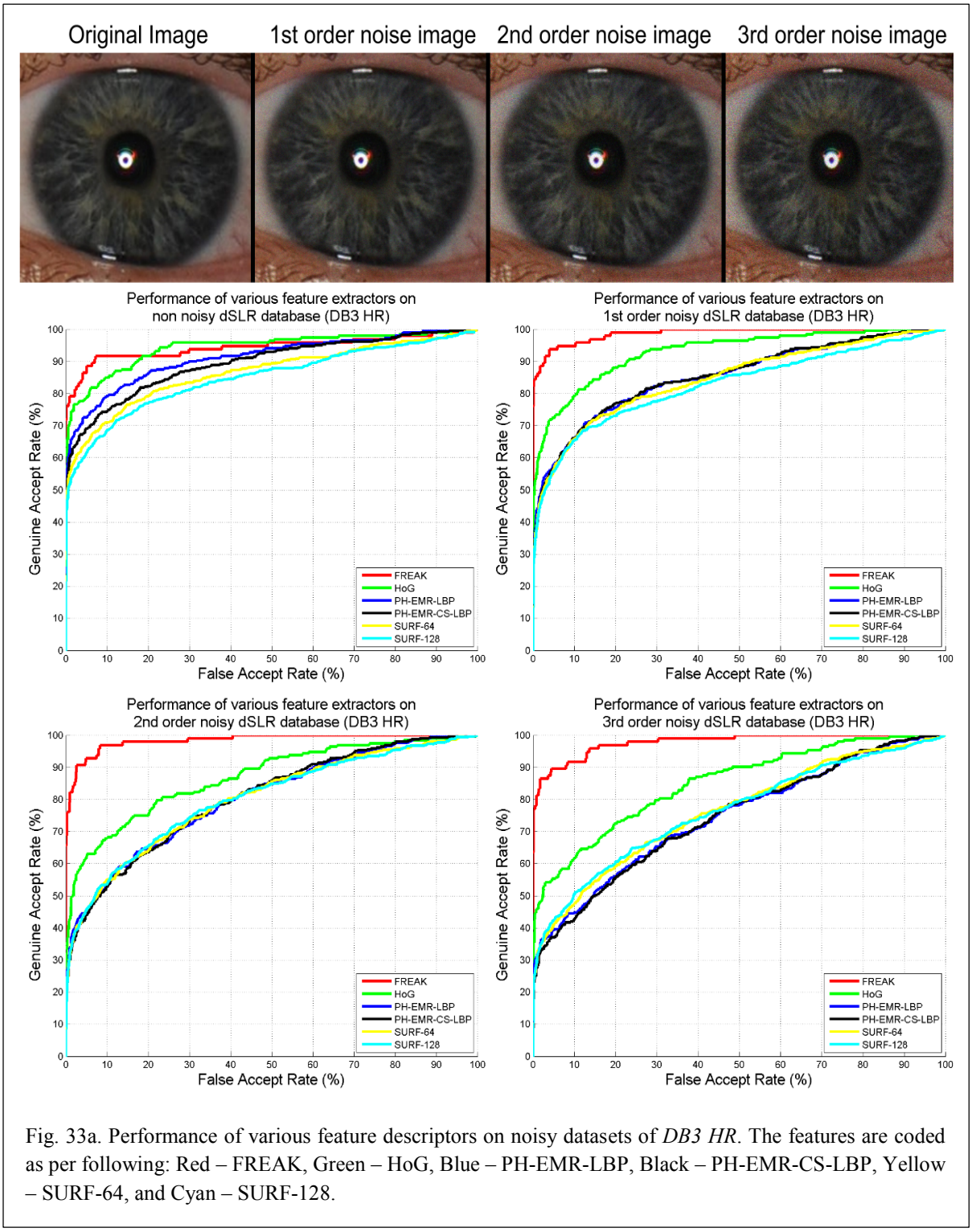

Fig. 33a. Performance of various feature descriptors on noisy datasets of *DB3 HR*. The features are coded as per following: Red – FREAK, Green – HoG, Blue – PH-EMR-LBP, Black – PH-EMR-CS-LBP, Yellow – SURF-64, and Cyan – SURF-128.

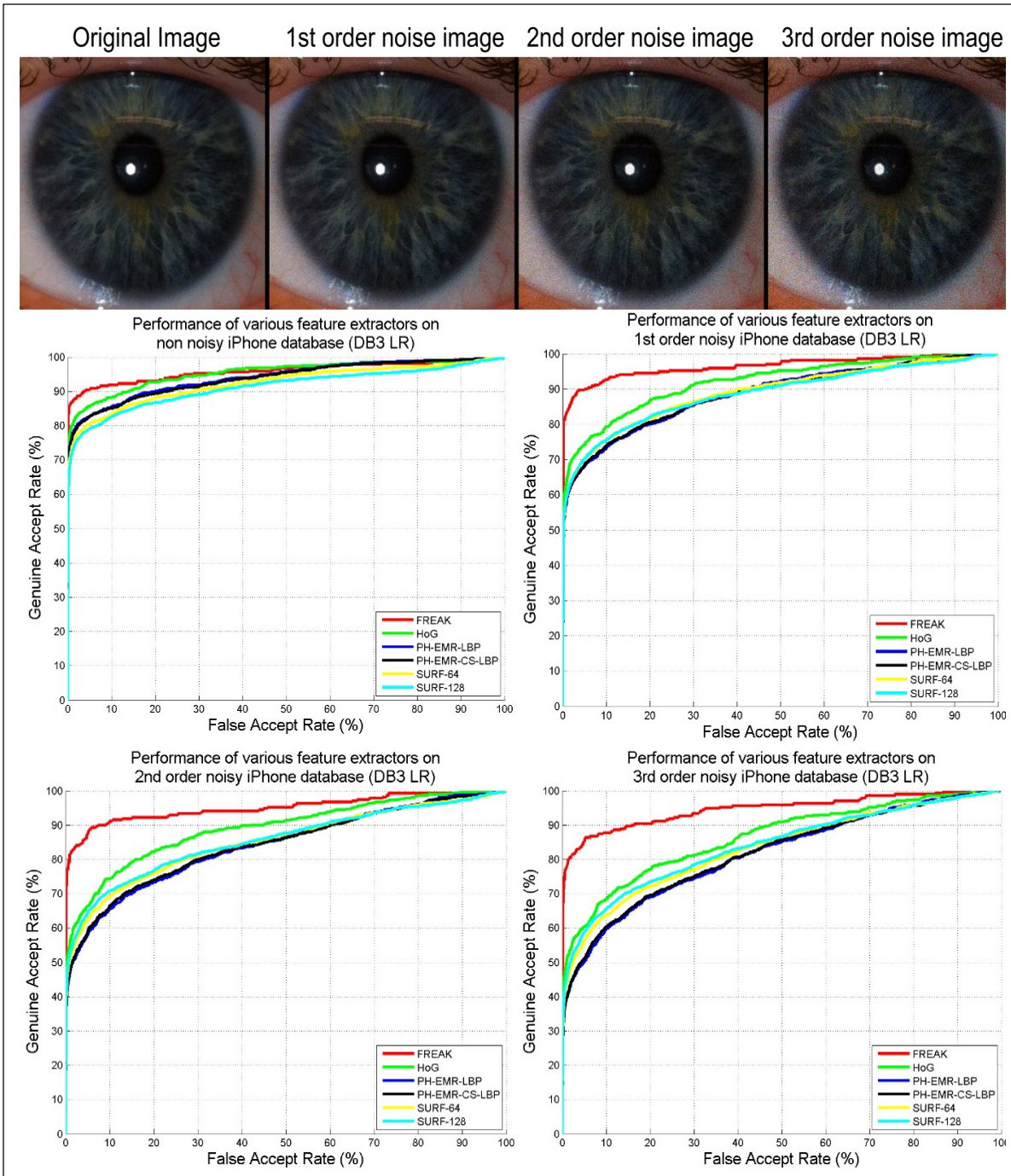

Fig. 33b. Performance of various feature descriptors on noisy datasets of *DB3 LR*. The features are coded as per following: Red – FREAK, Green – HoG, Blue – PH-EMR-LBP, Black – PH-EMR-CS-LBP, Yellow – SURF-64, and Cyan – SURF-128.

Table 9: Performance of Iris biometric systems on DB3

Database	Method	Noise order	AUC	EER (%)	[1]GAR	[2]GAR	[3]GAR	d
DB 3 HR	Daugman	0	96.72	9.11	55.40	79.86	87.05	2.91
DB 3 HR	Daugman	1	92.42	15.62	43.17	63.31	74.82	2.31
DB 3 HR	Daugman	2	90.50	18.63	44.24	60.43	70.50	2.16
DB 3 HR	Daugman	3	86.67	21.74	42.09	57.19	67.27	1.99
DB 3 HR	Proposed	0	94.39	8.33	71.88	79.17	88.54	3.63
DB 3 HR	***Proposed***	***1***	***98.73***	***6.10***	***75.00***	***85.42***	***93.75***	***4.98***
DB 3 HR	Proposed	2	98.42	7.29	64.58	82.29	92.71	4.69
DB 3 HR	Proposed	3	97.78	8.41	63.54	81.25	89.58	4.57
DB 3 LR	Daugman	0	94.61	11.49	61.84	81.58	84.21	2.98
DB 3 LR	Daugman	1	90.88	16.90	52.63	67.98	74.56	2.42
DB 3 LR	Daugman	2	88.34	19.92	50.88	59.21	67.11	2.19
DB 3 LR	Daugman	3	87.42	22.43	49.12	59.65	66.23	2.12
DB 3 LR	***Proposed***	***0***	***95.89***	***8.57***	***78.89***	***87.04***	***90.74***	***4.45***
DB 3 LR	Proposed	1	96.44	8.51	75.56	83.70	90.00	4.42
DB 3 LR	Proposed	2	95.07	9.61	59.63	81.48	87.41	3.99
DB 3 LR	Proposed	3	94.65	11.61	58.52	78.15	85.19	3.76

[1]GAR – GAR at 0% FAR, [2]GAR – GAR at 1% FAR, [3]GAR – GAR at 5% FAR, d – d-prime
Proposed – Local matching method

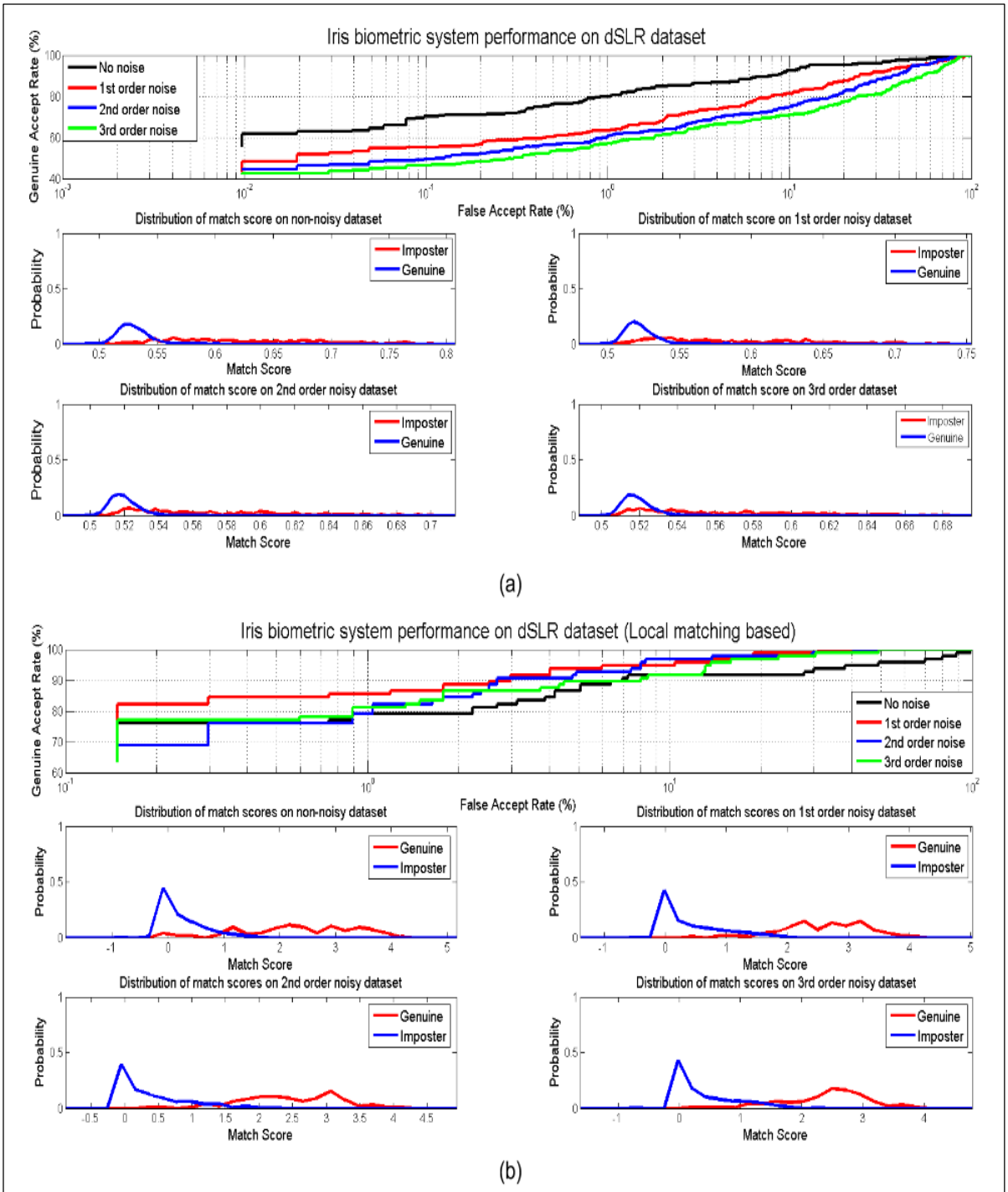

Fig. 34a. Performance of Daugman's proposed iris recognition on various noisy *DB3 HR* databases. (Black – No noise, Red – 1st order noise, Blue – 2nd order noise, Green – 3rd order noise) (b) Performance of *Proposed Method* for iris recognition on various noisy *DB3 HR* databases.

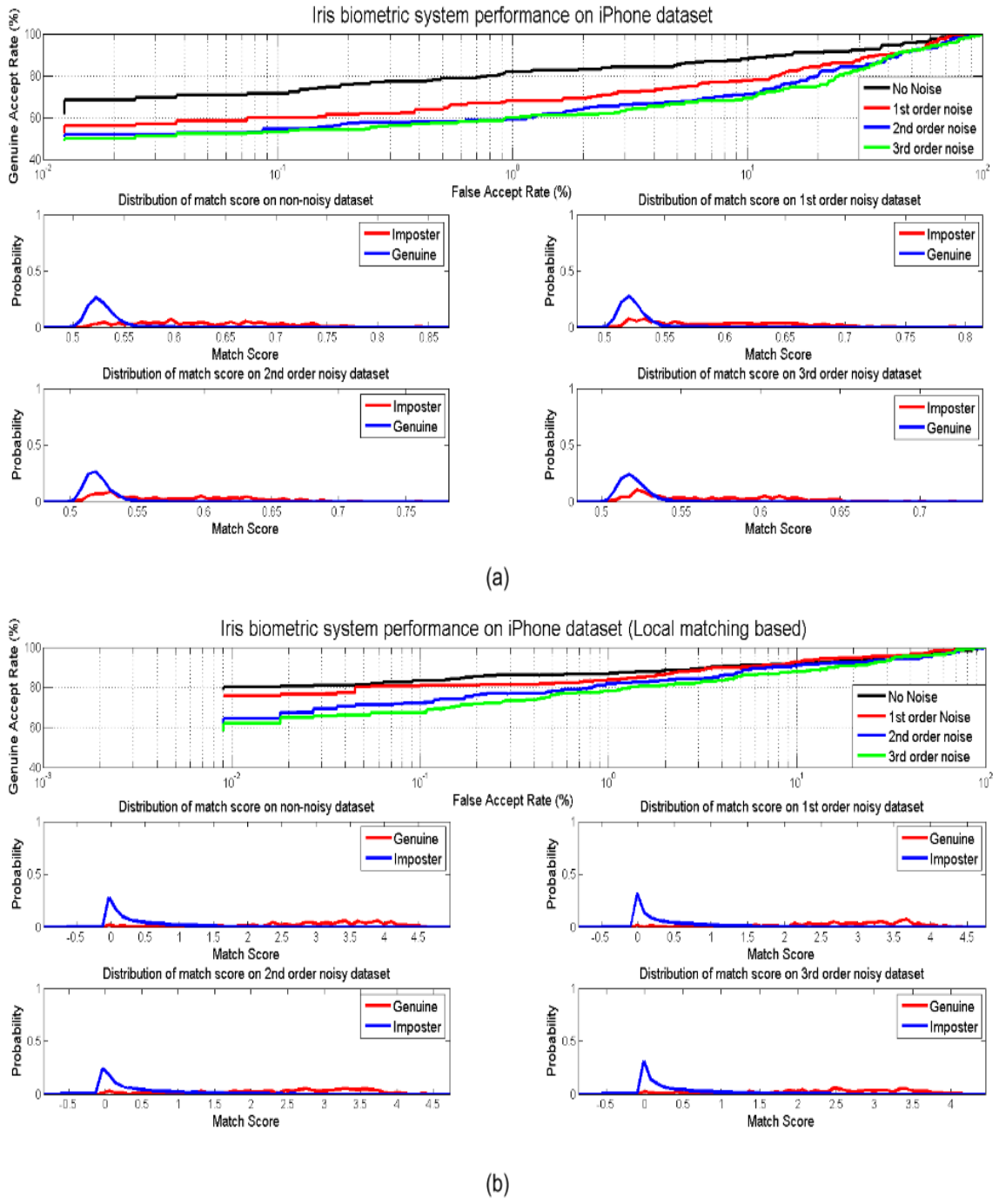

Fig. 35a. Performance of Daugman's proposed iris recognition on various noisy *DB3 LR* databases. (Black – No noise, Red – 1st order noise, Blue – 2nd order noise, Green – 3rd order noise) (b) Performance of *Proposed Method* for iris recognition on various noisy *DB3 LR* databases.

It was also taken care that minimal segmentation errors were present in the dataset, thus neglecting the effect of segmentation on traditional matching method. However, it was more interesting to see feature based local matching performing better especially with darker irides where texture is very limited. The major difference in error for Daugman's based method was introduced by darker irides. It is observed that the proposed local matching method performs better than conventional iris matching methods especially when more noise is introduced in the data. Best error rate of 6.1% was observed for *DB3 HR* databased with proposed method, compared to 15% error using traditional iris method on the same dataset. For *DB3 LR,* best error rate of 8.5% was obtained using proposed local matching method compared to 11.5% error rate using traditional iris method on the same dataset. It is also seen that with traditional matching, adding noise until first two order's doesn't degrade the performance of the local matching based algorithm. However, in case of traditional iris matching, adding noise significantly drops the performance of the biometric system thus proving local feature based matching are more resilient to signal noise and other image aberrations.

Additionally in order to validate the performance of *Proposed Method*, I use a publicly available iris database collected by BIPLab[1] (*MICHE*). The reason for using *MICHE* database over other smartphone iris database is due to its large subject population. In order to test the performance of *Proposed Matcher* on *MICHE* database, I add two additional modules - eye detection module to detect eyes from partial face images and iris quality module to detect bad iris samples. Iris quality module was implemented from Gottemukkula (Gottemukkula et al., 2014).

MICHE dataset consists of images captured using iPhone 5 and Samsung Galaxy S4, while I use Samsung S4 images. The images are captured using both frontal and rear camera in indoor

and outdoor conditions resulting in four scenarios. Each scenario is referred with X_Y where X represents camera (RF for rear camera and FF for front camera) and Y represents illumination (O for outdoor and I for indoor). So, a total of four scenarios are possible in this study – RF_I, RF_O, FF_I, and FF_O. Each of these scenarios are fed through the biometric system. It might be possible that different subjects are accepted for final performance calculations in different scenarios due to the quality of the iris image being captured. I report Failure to Enroll (FTE) rate for each scenario which includes eye crop failure or image quality rejection.

Data was collected in two different sessions with multitude of iris samples captured in each session. However, two sessions are not available for most of the subjects in the dataset. So, I use a single session to report the performance of the biometric system. For each session, I select first two irides with highest quality as enrollments and remaining samples as verifications. The final score is obtained by selecting the maximum score amongst all matches. Table 10 provides the EER scores obtained for each scenario.

Table 10: Performance of *Proposed* Iris biometric systems on *MICHE* database

Database	Scenario	Features	AUC	EER (%)	[1]GAR	[2]GAR	[3]GAR	d	FTE
MICHE	FF-I	FREAK	99.62	3.07	95.45	95.45	98.48	5.98	-
MICHE	FF-I	HoG	99.62	4.51	83.33	93.94	96.97	4.99	-
MICHE	FF-I	PH-EMR-LBP	99.31	4.76	73.85	86.15	95.38	3.96	-
MICHE	FF-I	PH-EMR-CS-LBP	99.51	4.55	64.62	89.23	95.38	4.03	-
MICHE	FF-I	SURF	99.89	1.52	92.31	98.46	98.46	6.61	-
MICHE	***FF-I***	***Fusion***	***99.99***	***0.15***	***95.45***	***100.00***	***100.00***	***6.58***	***12%***
MICHE	FF-O	FREAK	97.58	5.97	88.06	89.55	94.03	4.45	-
MICHE	FF-O	HoG	97.90	7.33	89.55	91.04	92.54	4.01	-
MICHE	FF-O	PH-EMR-LBP	96.42	7.48	85.07	89.55	92.54	3.23	-
MICHE	FF-O	PH-EMR-CS-LBP	96.66	8.79	83.58	88.06	91.04	3.29	-
MICHE	FF-O	SURF	96.77	7.05	85.07	89.55	91.04	4.62	-
MICHE	***FF-O***	***Fusion***	***97.58***	***5.97***	***88.06***	***89.55***	***94.03***	***4.45***	***10.67%***
MICHE	RF-I	FREAK	99.35	1.46	94.20	98.55	98.55	7.08	-
MICHE	RF-I	HoG	99.98	1.23	91.18	98.53	100.00	7.00	-
MICHE	RF-I	PH-EMR-LBP	99.99	0.11	89.86	100.00	100.00	6.95	-
MICHE	RF-I	PH-EMR-CS-LBP	99.92	1.48	91.30	97.10	100.00	6.77	-
MICHE	RF-I	SURF	99.38	2.92	92.75	95.65	97.10	6.48	-
MICHE	***RF-I***	***Fusion***	***100.00***	***0.01***	***98.55***	***100.00***	***100.00***	***8.33***	***30.67%***
MICHE	RF-O	FREAK	96.84	5.79	88.46	88.46	92.31	5.03	-
MICHE	RF-O	HoG	98.73	5.70	90.38	90.38	92.31	5.31	-
MICHE	RF-O	PH-EMR-LBP	96.65	3.82	88.46	94.23	96.15	4.70	-
MICHE	RF-O	PH-EMR-CS-LBP	97.87	3.88	88.46	92.31	96.15	5.00	-
MICHE	RF-O	SURF	95.59	5.87	88.24	94.12	94.12	5.16	-
MICHE	***RF-O***	***Fusion***	***97.24***	***3.85***	***88.46***	***96.15***	***96.15***	***5.60***	***8%***

[1]GAR – GAR at 0% FAR, [2]GAR – GAR at 1% FAR, [3]GAR – GAR at 5% FAR, d – d-prime; Fusion – Weighted fusion (mean) of FREAK, PH-EMR-LBP, PH-EMR-CS-LBP, and SURF.

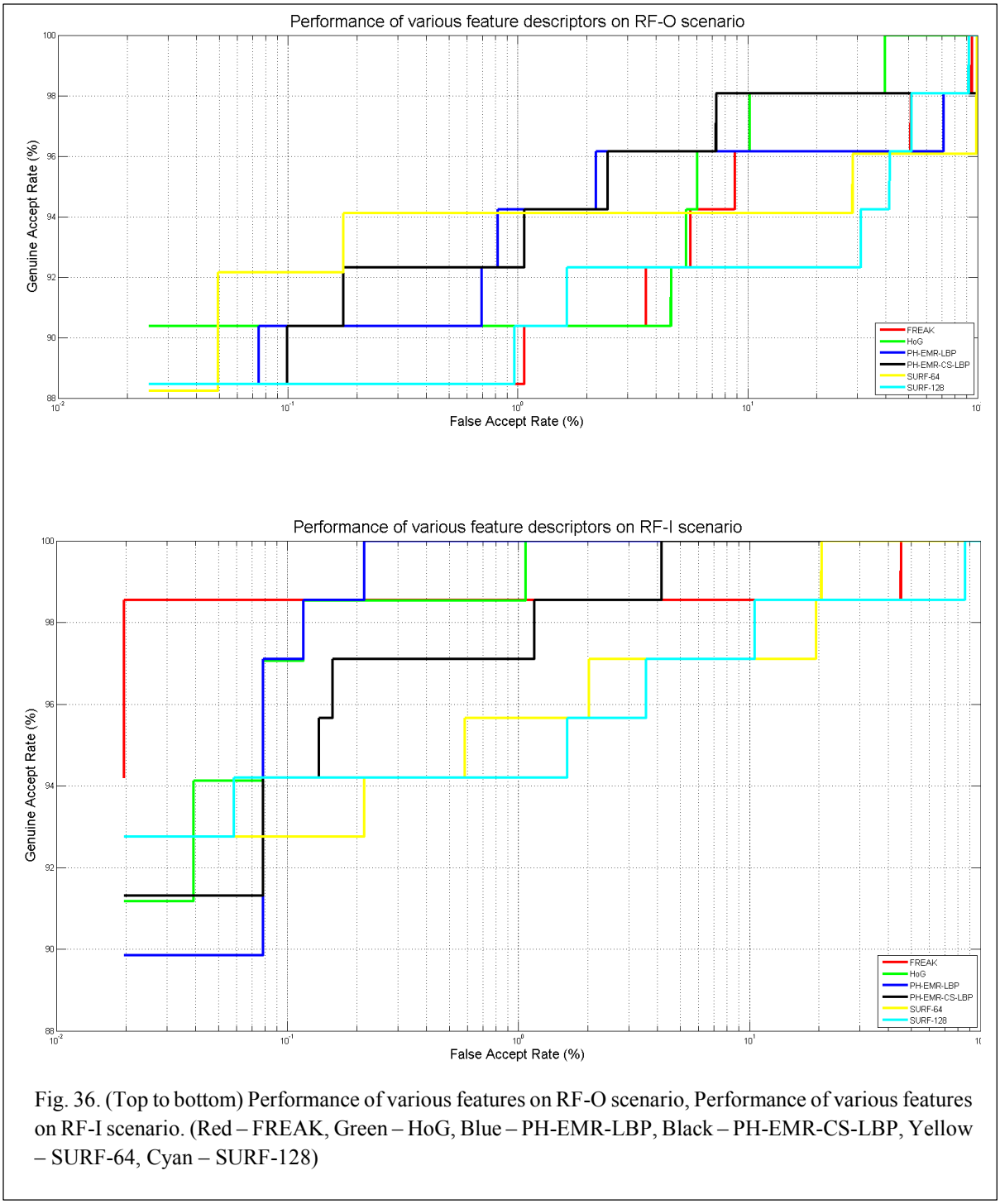

Fig. 36. (Top to bottom) Performance of various features on RF-O scenario, Performance of various features on RF-I scenario. (Red – FREAK, Green – HoG, Blue – PH-EMR-LBP, Black – PH-EMR-CS-LBP, Yellow – SURF-64, Cyan – SURF-128)

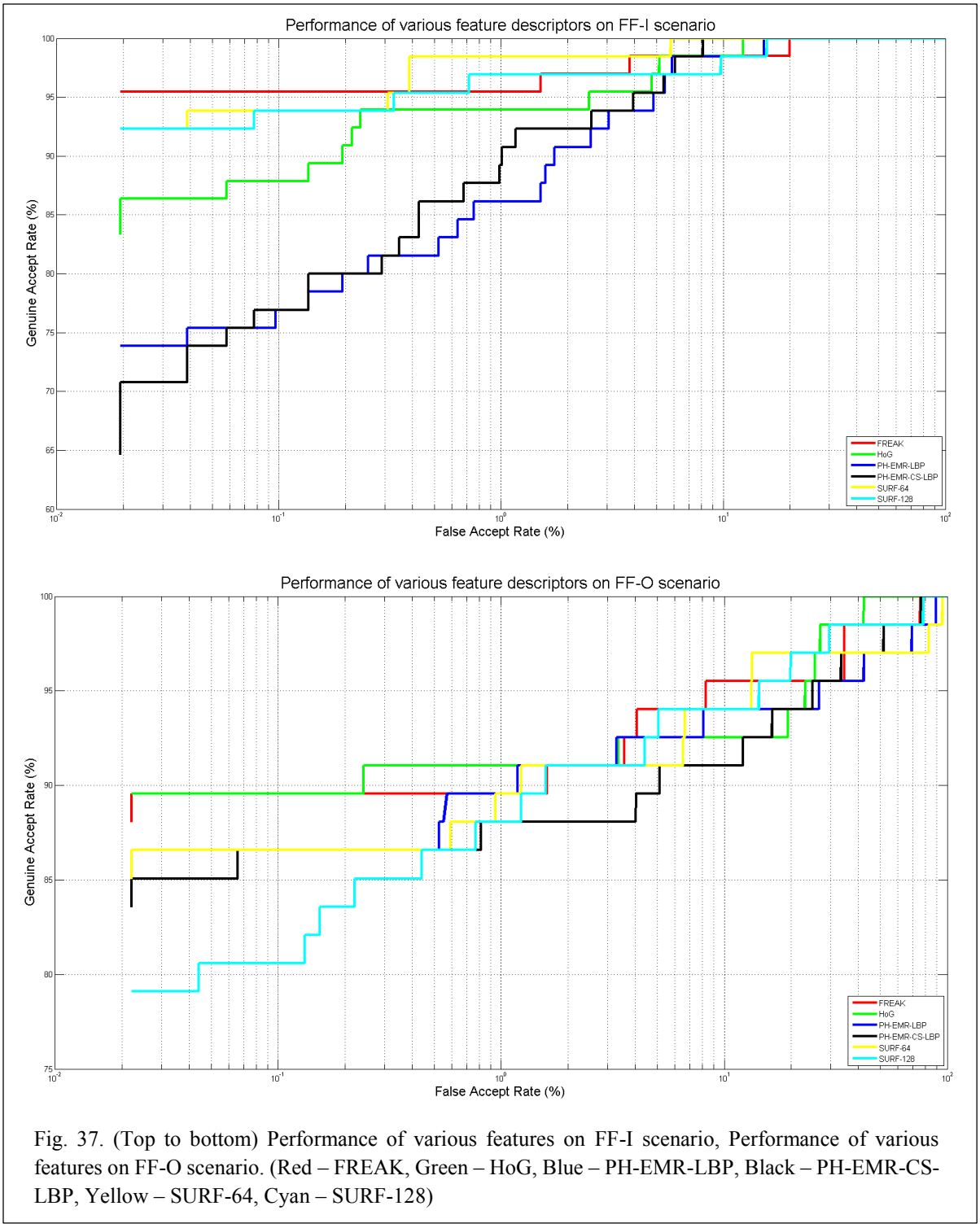

Fig. 37. (Top to bottom) Performance of various features on FF-I scenario, Performance of various features on FF-O scenario. (Red – FREAK, Green – HoG, Blue – PH-EMR-LBP, Black – PH-EMR-CS-LBP, Yellow – SURF-64, Cyan – SURF-128)

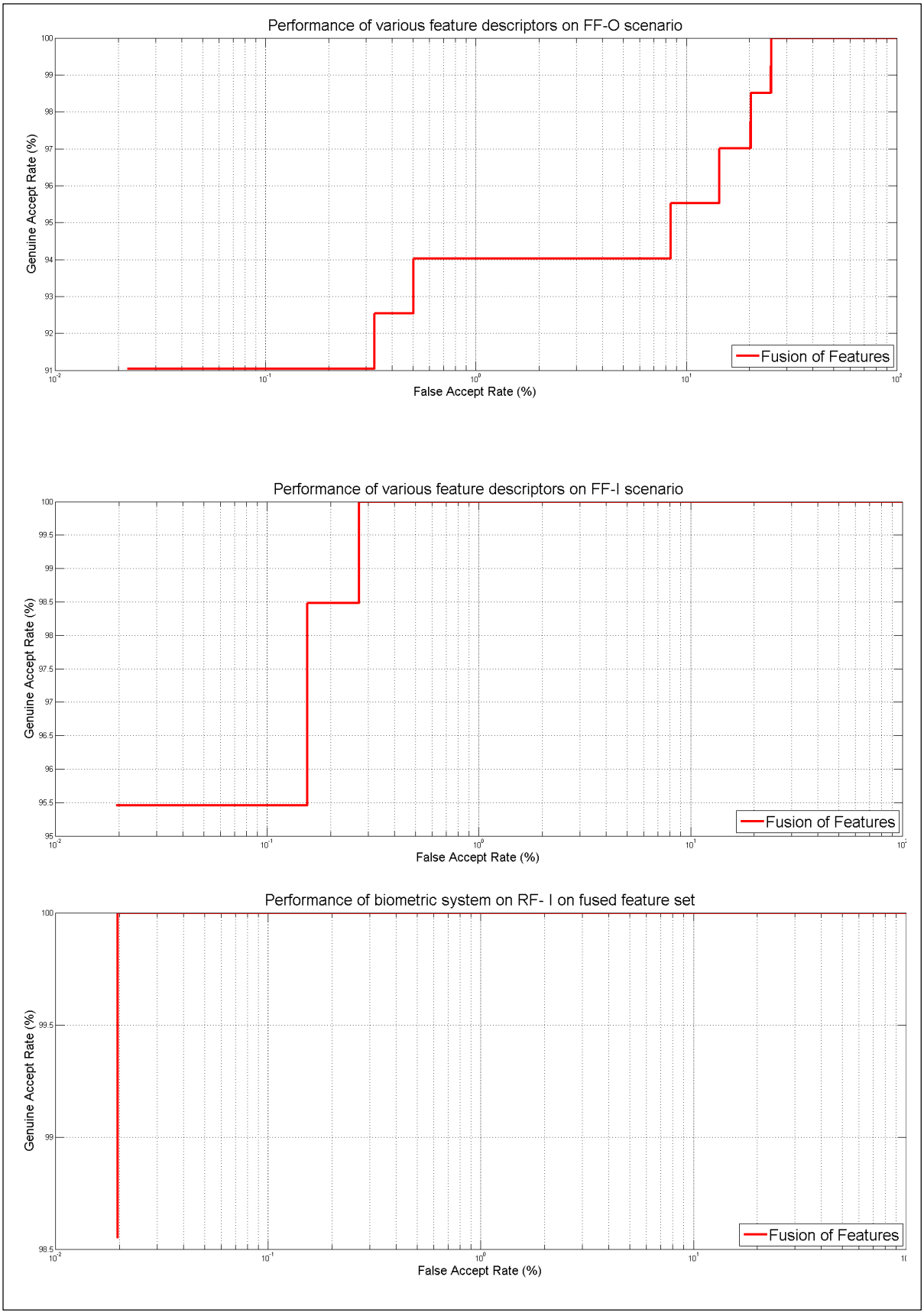
Performance of various feature descriptors on FF-O scenario
Genuine Accept Rate (%)
False Accept Rate (%)
Fusion of Features
Performance of various feature descriptors on FF-I scenario
Genuine Accept Rate (%)
False Accept Rate (%)
Fusion of Features
Performance of biometric system on RF- I on fused feature set
Genuine Accept Rate (%)
False Accept Rate (%)
Fusion of Features

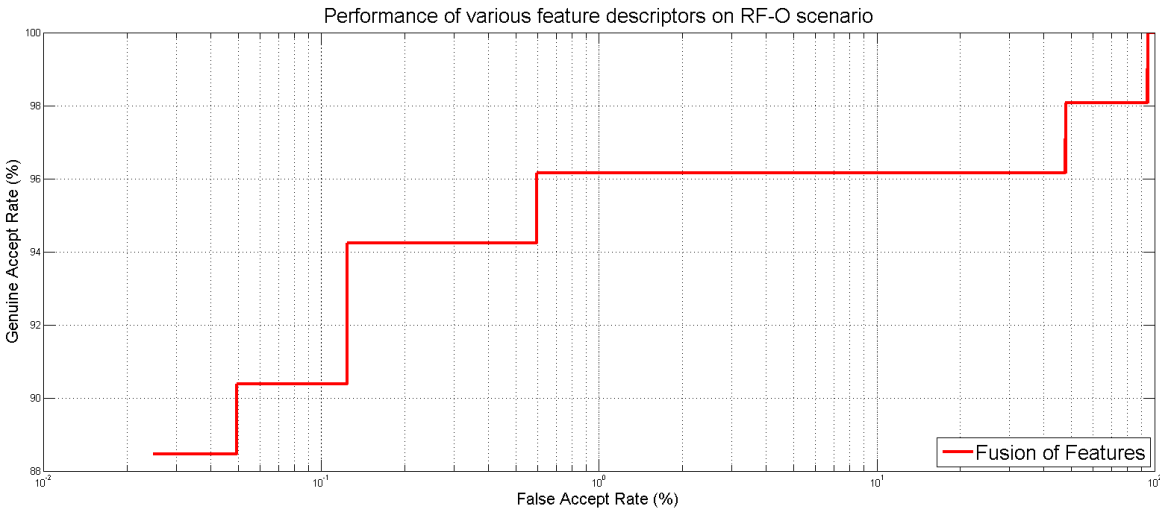

Fig. 38. (Top to bottom) Performance of weighted fusion method on FF-O, FF-I, RF-I, RF-O scenarios respectively

Based on previous study by Raja (Raja et. al., 2014), EER on the database was provided for fifty unique irides across various scenarios. So, results in my study are not comparable to the one published by Raja. However, in all the scenarios, I did have larger sample size compared to one used by Raja and the error rates I obtained were less than those reported in the study.

CHAPTER 6

PERI OCULAR RECOGNITION ON SMARTPHONES

Use of periocular region as a biometric trait has been gaining importance in past decade due to its ease of capture especially in uncontrolled environment. It has also been observed that periocular region performs better than face for recognition purposes in unconstrained environment (Juefie-Xu et al., 2012). Although my datasets do not have uncooperative or non-cooperative users, many of the users lack proper training in using application for capturing biometric. Due to this many subjects pose in awkward angles replicating poses in uncooperative user situations.

The first study of periocular recognition in visible spectrum can be traced back to Park et al. (Park et al. 2009) using local and global feature matching. In global feature matching, eye images were registered using center of the iris as a reference point. Scale invariance was achieved by using the radius of iris as length of patches used for dividing the image. Local features extracted from patches in the image were concatenated into a single dimension vector (global feature). For local feature based matching, SIFT, LBP and HoG features were used. These features provided scale and rotation resilience. Based on this method, there were other methods developed making enhancements towards better feature extraction methods (Table 3). Santos (Santos et al., 2014) initially tested the feasibility of using periocular biometrics on smartphones. They use LBP, HoG, ULBP, GIST, and, SIFT features. Match scores from respective features are then provided to a feed forward neural network to obtain a final score. They report least error rate of 14.5% using a variety of locally derived features fused using neural network model.

Juefei-Xu (Jufei-Xu et al., 2012) have done a comprehensive study on periocular recognition in unconstrained environment laying a solid foundation for further experiments.

My design of periocular recognition model is similar to eye vascular and iris recognition models. The design consists of four critical components: Periocular region extraction (ROI), ROI enhancement, feature extraction, matching.

6.1. Periocular Recognition

6.1.1. Periocular Region Extraction (ROI extraction)

Periocular region has no defined boundary and area enclosing periocular region varies based on the application. Earlier experiments by Padole (Padole and Proenca, 2012) and Santos (Santos et al., 2014) used fixed areas around the eye based on a certain measurable value such as eye width or iris radius. Padole (Padole and Proenca, 2012) shows that using eye corners as reference provides better registration over iris center. Also, they show the significance of scale in periocular region performance. I use *DB1 Still* day 1 and *DB2 FF* day 1 short term samples as a validation datasets for DB1 and DB2 respectively. Based on the user's posture while capturing eye images and eye detection algorithm, it is expected to see varying periocular region from the eye crops. It is possible that some eye samples consist of eye brows and some do not. After the eye region is extracted, I crop all the images tightly to the ocular region using sclera and iris masks. I then increment the size of the tightly cropped image by a constant factor until I attain best performance. It should be noted that most of images do not have extreme scale aberrations due to the design of the biometric capture application used to capture the images. Based on the resolution at which the database was captured, the size of periocular region varies to provide best performance. So, size of periocular region required for best

performance is device specific or at least sensor specific. Also, since I do not register the images, and expect the local matching to compensate for any rotation aberrations, it is seen that area at which periocular region performs the best is larger than what it might be for registered images. On both DB1 and DB2 datasets, for the optimal periocular performance, it is seen that:

- Widths of region 2 and region 3 should be equal to 15% of the bounding box width.
- Height of region 1 should be 30% of bounding box height.
- Height of region 4 should be equal to 15% of bounding box height.

Fig. 39. (Row wise) Enrollment, Verification – Original Image, Iris and Sclera Mask, Tight crop, extracted ROI from tight crop based on optimal periocular size

Significance of these regions are discussed in later sections.

6.1.2. ROI Enhancement

In unconstrained environment, for robust periocular recognition, it is necessary to perform illumination normalization. I use Self Quotient Image (SQI) followed by CLAHE as an image preprocessing technique for periocular recognition. SQI has demonstrated excellent

performance in challenging illumination conditions for face recognition. I modify the algorithm to speed up the calculations required, especially the convolutions, although the concept remains the same.

6.1.3. Feature Extraction Process

For feature extraction, I use the same local features that are being used for eye vasculature. It is seen that periocular region that is typically matched consists of wrinkles or other regions that are structurally similar to eye vasculature. For feature detection, I test the proposed feature detector (VPD) with dense FAST and SURF feature detectors. Based on the validation results, I design a feature detection method based on fusion of various tested feature detectors.

6.1.4. Feature Matching Technique

A similar feature matching technique described in *Section 4.6* is employed for periocular region matching. Since the matching technique I use requires MxN (M enrollment points vs. N verification points) comparisons for a match, it is not practical to use complete periocular region for matching purposes (The number of interest points detected in periocular region is at least thrice that of points detected in ocular region). So, in the first step, I apply *Non Vascular Point Suppression* as described in *Section 4.5.4*. This technique helps on removing all points that do not contain high edge information. Although, *NVS* helps removing up to 30% of the points detected in periocular region, the average number of points being retained still remains very high. So, in order to effectively use periocular region for mobile

based verification, I use partial periocular region based on the regions ability to contribute towards the final match score.

For determining potential partial periocular regions that play an important role in final match score calculations, I divide the periocular region in four quadrants. These four regions are ranked for significance based on the number of interest points being retained for match score calculations over a validation dataset. I progressively the partial periocular regions based on their significance until a match threshold is acquired in verification process. Design, advantages and performance of this technique is shown in *Model 2* of multimodal biometric system. In this section, since most of the datasets have inconsistent crops (with no full face images) especially with upper eyelid, I test the performance of complete periocular region as a biometric to that of lower eyelid region alone. I hypothesize that since upper periocular region is inconsistent, just using lower eyelid region should perform as good as full eye region.

6.2. Results

It is seen that FREAK descriptor doesn't contribute towards periocular biometric system (Fig. 41). Although the results shown in figure 41 is on *DB2 BF* alone, a rigorous validation on all datasets show similar trend in performance of individual feature descriptors. So, a fusion of PH-EMR-LBP, PH-EMR-CS-LBP and SURF is used as described in *Section 4.6.1*. Also, it is observed that *NVS* algorithm used to suppress non-vascular points helps the matcher speed up the verification process by four folds across all datasets. *NVS* also helps reduce the error rate across all the tested datasets compared to non *NVS* based biometric systems. This is due to false matches seen due to low quality features observed in bad images.

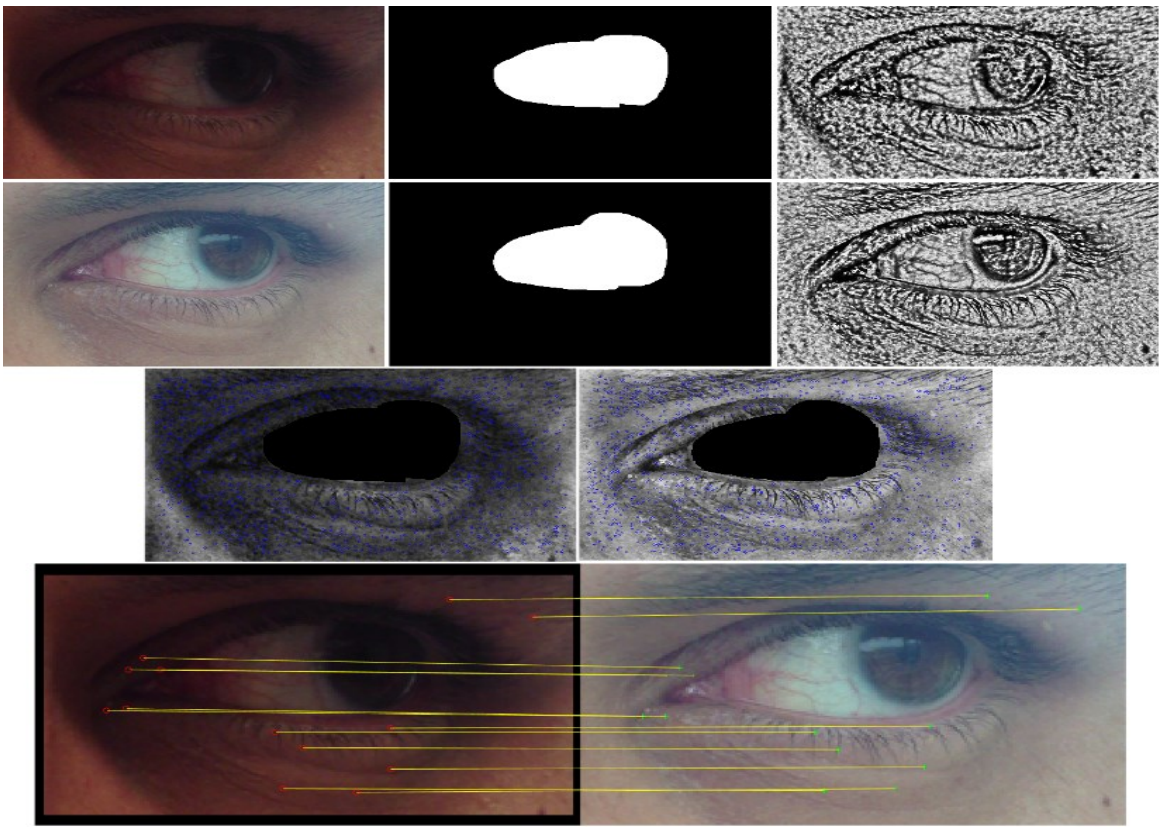

Fig. 40. (Row wise): [Enrollment, Verification] - Original image, Enrollment mask (false pixels), enhanced image for periocular recognition; Detected points in enrollment and Verification, Matched points after RANSAC

Individually, as for the feature detectors, fusion of FAST and SURF has a better retention rate over VPD for high quality images. However, for low quality images captured with front facing camera, VPD outperforms FAST and SURF points in terms of retention capability. With fusion of all feature detectors as described in *Point Fusion (Section 4.5.4)*, it is observed that VPD improves the retention rate for high and low quality image dataset.

A major contribution of this study is observed from the analysis derived from lower eyelid region. From Table 12, we can observe that lower eyelid region alone performs as good as complete periocular region across all datasets. This observation proves the hypothesis that

lower eyelid region has sufficient information to perform as good as complete periocular region.

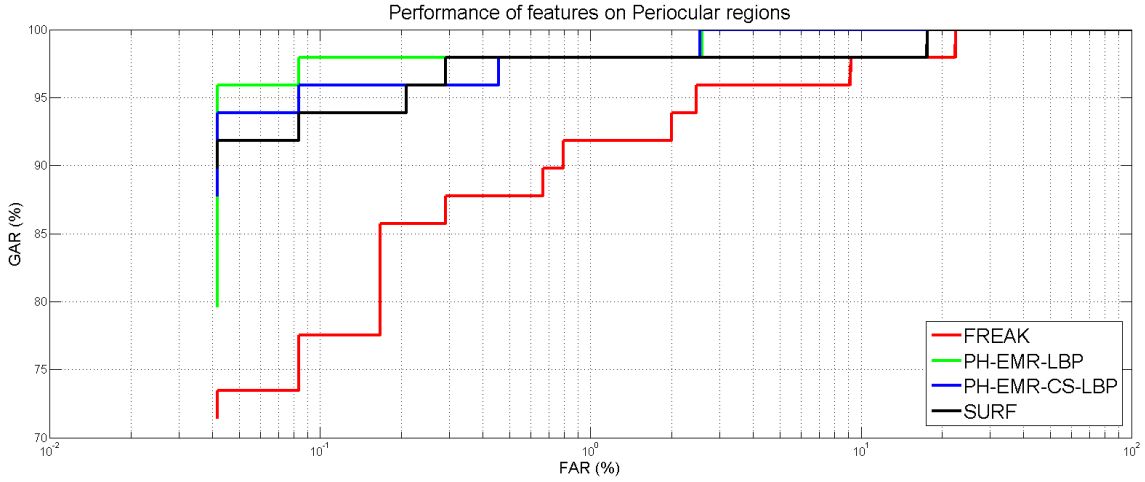

Fig. 41. Performance of individual features on periocular region for DB2 BF database

Table 11: Performance of *Periocular* biometric systems on various databases

Database	Vascular Point Suppression	[5]CT (sec)	AUC	EER (%)	[1]GAR	[2]GAR	[3]GAR	d	FTE	[4]Retention Ratios
DB1 Video	Yes	1.2	99.89	0.23	99.41	99.61	99.89	9.02	0%	10%, 16%, (9%+11%)
DB1 Video	No	7.68	99.52	0.62	97.94	99.2	99.2	9.855	0%	10%, 12%, (11%+15%)
DB2 RF	Yes	0.8	97.05	0.11	91.66	99.67	99.25	5.38	2%	6%, 9%, (10%+12%)
DB2 RF	No	5.2	98.20	0.32	95.19	96.82	97.68	4.71	2%	5%, 12%, (8%+13%)
DB2 FF	Yes	0.76	99.07	1.49	89.38	99.84	99.07	5.01	2%	16%, 8%, (15%+6%)
DB2 FF	No	4.68	98.82	1.86	85.90	96.98	98.79	4.86	2%	12%, 6%, (13%+5%)
MICHE	Yes	1.73	98.24	1.85	90.23	96.98	96.98	6.23	8%	12%, 6%, (13%+5%)
MICHE	No	4.32	98.31	1.78	91.46	97.05	97.05	6.30	8%	12%, 6%, (13%+5%)

[1]GAR – GAR at 0% FAR, [2]GAR – GAR at 1% FAR, [3]GAR – GAR at 5% FAR, d – d-prime; [4]Retention Ratio – VPD only, FAST & SURF only, VPD+FAST+SURF fusion, [5]CT – Average computation time for verification process.

Table 12: Performance of *Periocular* biometric systems on lower eyelid vs. complete eye region

Database	ROI	[5]CT (sec)	AUC	EER (%)	[1]GAR	[2]GAR	[3]GAR	d	FTE
DB1 Video	Lower	0.8	98.53	0.20	97.23	97.23	97.54	8.31	0%
DB1 Video	Complete	1.2	99.89	0.23	99.41	99.61	99.89	9.02	0%
DB2 RF	Lower	0.4	93.05	0.52	87.56	89.52	91.35	4.12	2%
DB2 RF	Complete	0.8	97.05	0.11	91.66	99.67	99.25	5.38	2%
DB2 FF	Lower	0.4	95.23	3.21	81.53	91.24	94.69	4.82	2%
DB2 FF	Complete	0.76	99.07	1.49	89.38	99.84	99.07	5.01	2%
MICHE	Lower	0.87	98.76	1.12	91.41	96.82	96.82	6.43	8%
MICHE	Complete	1.73	98.24	1.85	90.23	96.98	96.98	6.23	8%

[1]GAR – GAR at 0% FAR, [2]GAR – GAR at 1% FAR, [3]GAR – GAR at 5% FAR, d – d-prime; [4]Retention Ratio – VPD only, FAST & SURF only, VPD+FAST+SURF fusion, [5]CT – Average computation time for verification process.

6.3. Fusion

There are two fusion scenarios that I employ in my experiments. The first fusion scenario is performed after feature matching (Pre-Score fusion) and the second fusion scenario is performed after score generation (Post-Score fusion) for each biometric traits. Pre-Score fusion refers to a scenario where matched points from various ROI's (biometric traits) are given to single RANSAC for generating a single score. Post-Score fusion is a scenario where multiple RANSAC's are applied to multiple matched points from corresponding ROI's to generate multiple scores (based on the number of ROI's). The results of Model 1 and Model 2 described in sections *2.5.1* and *2.5.2* respectively are provided in Table 13 and 14 respectively.

Table 13: Performance of *multimodal* biometric system (*Model 1*)

Database	ROI	[5]CT (sec)	AUC	EER (%)	[1]GAR	[2]GAR	[3]GAR	d	FTE
DB1 Video	EyePrint, Periocular	2.8	100.00	0	100.0	100.0	100.0	10.01	0%
DB2 RF	EyePrint, Periocular	1.9	99.9	0.02	98.98	99.21	99.9	11.1	0%
DB2 FF	EyePrint, Periocular	1.03	99.76	0.08	97.45	97.24	98.9	9.82	0%
DB3 HR	Iris, Periocular	3.28	99.98	0.02	99	99	100	10.2	0%
DB3 HR	EyePrint, Periocular	3.03	100	0	100	100	100	10.3	0%
DB3 HR	Iris, Eyeprint	2.03	99.67	0.1	98.12	99	99	8.13	0%
DB3 LR	Iris, Periocular	2.23	99.9	0.01	98.9	100	100	11.2	0%
DB3 LR	EyePrint, Periocular	1.23	100	0	100	100	100	9.67	0%
DB3 LR	Iris, Eyeprint	1.15	98.65	0.16	97.12	98.6	99.1	9.2	0%
MICHE	Iris, Periocular	2.18	99.24	0.25	97.23	97.98	99.28	6.23	1%

[1]GAR – GAR at 0% FAR, [2]GAR – GAR at 1% FAR, [3]GAR – GAR at 5% FAR, d – d-prime; [4]Retention Ratio – VPD only, FAST & SURF only, VPD+FAST+SURF fusion, [5]CT – Average computation time for verification process.

Table 14: Performance of *multimodal* biometric system (*Model 2*)

Database	ROI	[5]CT (sec)	AUC	EER (%)	[1]GAR	[2]GAR	[3]GAR	d	FTE
DB3 HR	Eyeprint, Iris, Periocular	3.8	100	0	100	100	100	11.45	0%
DB3 LR	Eyeprint, Iris, Periocular	2.13	100	0	100	100	100	10.67	0%
MICHE	Eyeprint, Iris, Periocular	3.18	99.82	0.15	98.23	99.8	99.8	6.51	1%

[1]GAR – GAR at 0% FAR, [2]GAR – GAR at 1% FAR, [3]GAR – GAR at 5% FAR, d – d-prime; [4]Retention

CONCLUSIONS AND FUTURE WORK

Our work outlines a practical application of an ocular biometric system on smartphones using both 1.3 and 8 mega-pixel camera sensors. Although a framework for multibiometric system using smartphones has previously been introduced in the literature, my work outlines a practical approach with higher performance and lower computational footprint. Validation of the system performance was implemented on an in-house database and a publicly available database. Performance of the multimodal biometric system on in-house databases - DB1 and DB2 demonstrates the applicability of the proposed system on smartphones. Additionally, performance of the proposed system on a publicly available database shows its efficiency in handling various aberrations in data capture that were not seen in in-house databases. The false rejects in the system were obtained mainly from bad image crops that passed image quality metrics. However, it should also be noted that the subjects who participated in the data capture procedure had minimal training for capturing the ocular regions. Since, using ocular biometrics on smartphones is not prominent amongst smartphone users (as compared to fingerprints), data capture was inconsistent, which can always be improved by improving the data capture application.

False Reject Rate (FRR) and Failure to Enroll of the proposed multimodal biometric system decreases significantly over unimodal biometric systems for both DB1 and DB2. A new quality metric that measures the amount of visible vasculature based on Vascular Point Detector (VPD) is proposed. The Vascular Point Detector, non-training based curve and edge detector to find vasculature structures in noisy low-resolution images is introduced. VPD finds the most significant interest regions in an image compared to other interest point detectors, reducing the computational footprint in performing verification while maintaining a high

retention rate for detected versus matched points. A framework for progressive matching algorithm based on interest regions in periocular region is implemented. It is seen that progressive matcher reduces the computational footprint of multimodal biometric recognition in half compared to using all biometric modalities. Our multimodal application on a smartphone takes ~800 milliseconds on an Intel Quad-Core 2.2 GHz processor while the Samsung S4 and iPhone 5S take around 400 milliseconds.

BIBLIOGRAPHY

Alonso-Fernandez, F., Tome-Gonzalez, P., Ruiz-Albacete, V., Ortega-Garcia, J. 2009. Iris recognition based on sift features. International conference on Biometrics, Identity and Sec. 1–8.

Bay, H., Tuytelaars, & T., Van Gool, L. 2006. SURF: Speeded up robust features. Computer Vision – ECCV. 404-417.

Belcher, C., & Du, Yingzi. 2009. Region-based SIFT approach to iris recognition. Opt. Lasers Eng. 47. 139 -147.

Bellavia, F. 2011. Matching Image Features, Dissertation, University of Palermo, Italy.

Bharadwaj, S., Vatsa, M., & Singh, R. 2014. Biometric quality: a review of fingerprint, iris, and face. EURASIP Journal on Image and Video Processing. 1–28.

Bowyer, K. 2012. The results of the NICE II iris biometrics competition. Pattern Recognition Letters. 965–969.

Brown, M., & Lowe, D. 2002. Invariant features from interest point groups. Proceedings of the British Machine Vision Conference. 1-10

Canny, J.F. 1986. A computational approach to edge detection. IEEE Trans. on Pattern Analysis and Machine Intelligence. 8(6). 679-698.

Crihalmeanu, A., & Ross, A. 2011. On the use of multispectral conjunctival vasculature as a soft biometric. IEEE Workshop on Applications of Computer Vision, 204-211.

Crihalmeanu, A., & Ross, A. 2012. Multispectral patterns for ocular biometric recognition. Pattern Recognition Letters. 33(14). 1860-1869.

Crihalmeanu, A., Ross, A., & Derakhshani, R. 2009. Enhancement and registration schemes for matching conjunctival vasculature. Advances in Biometrics. 5558. 1240-1249.

Dalal, N., & Triggs, B. 2005. Histograms of Oriented Gradients for Human Detection. In Proceedings of IEEE Conference on Computer Vision and Pattern Recognition. 1. 886-893.

Dantcheva, A., Erdogmus, N., & Dugelay, J. L. 2011. On the reliability of eye color as a soft biometric trait. IEEE Workshop on Applications of Computer Vision (WACV). 227 – 231.

Daugman, J. 1993. High confidence visual recognition of persons by a test of statistical independence. IEEE Transactions on Pattern Analysis and Machine Intelligence. 148–1161.

Daugman, J. 1994. Biometric personal identification system based on iris analysis. U.S. Patent No. 5,291,560.

Daugman, J. 2004. How iris recognition works. IEEE Transactions on Circuits and Systems for Video Technology. 21–30.

Daugman, J. 2010. Introduction to iris recognition. http://www.cl.cam.ac.uk/~jgd1000/iris recognition.html.

Demirel, H., & Anbarjafari, G. 2008. Iris recognition system using combined histogram statistics. International Symposium in Computer and Information Sciences, 1-4.

Derakhshani, R., & Gottemukkula, V. 2013. Quality metrics for biometric authentication. US Patent – 8483459.

Derakhshani, R., & Gottemukkula, V. 2014. Quality metrics for biometric authentication. US Patent – 8724857.

Derakhshani, R., & Ross, A. 2007. A texture-based neural network classifier for biometric identification using ocular surface vasculature. International Joint Conference on Neural Networks. 2982-2987.

Derakhshani, R., Gottemukkula, V., & Hughlett, C. 2013. Texture features for biometric authentication. US Patent – 8369595.

Derakhshani, R., Gottemukkula, V., & Hughlett, C. 2014. Texture features for biometric authentication. US Patent – 8744141.

Derakhshani, R., Gottemukkula, V., & Saripalle, S. 2014. Biometric template security and key generation. US Patent Application – 14/454,148.

Derakhshani, R., Hughlett, C., Paben, J., Teply, J., & Rush, T. 2013. Spoof detection for biometric authentication. US Patent – 8437513.

Du, E. Y., WuDunn, D., Thomas, N. L. 2012. System and method for identifying a person with reference to a sclera image. US Patent - 20120163678

Fischler, M.A., & Bolles, R.C. 1981. Random Sample Consensus: A paradigm for model fitting with applications to image analysis and automated cartography. Communication of the ACM. 24(6). 381-395.

Föstner, M. A., & Gülch, E. 1987. A fast operator for detection and precise location of distinct points, corners and centers of circular features. ISPRS Intercommission Workshop. 149-155.

Freeman, W.T., & Adelson, E.H. 1991. The design and use of steerable filters. IEEE Trans. on Pattern Analysis and Machine Intelligence. 13(9). 891-906.

Gottemukkula, V., Saripalle, S.K., Derakhshani, R., & Tankasala, S.P. 2011. A texture-based method for identificaiton of retinal vasculature. IEEE Conference on Technologies for Homeland Security. 434-439.

Gottemukkula, V., Saripalle, S.K., Tankasala, S.P., Derakhshani, R., Pasula, R., & Ross, A. 2012. Fusing and conjunctival vasculature: Ocular biometrics in the visible spectrum. IEEE International Conference on Technologies for Homeland Security. 150-155.

Hilfiker, M.L., Hart, M., Holmes, R., Cooper, M., Kriett, J., Collins, D., & Allshouse, M. 1998. Expansion and division of conjoined twins. Journal of Pediatric Surgery. 33 (5). 768-770.

Hollingsworth, K., Bowyer, K. W., & Flynn, P. J. 2010. Identifying useful features for recognition in near-infrared periocular images. International Conference on Biometrics: Theory, Applications, and Systems. 1–8. 25, 26.

Jain, A.K., Flynn. P., & Ross. A. 2008. Handbook of biometrics. Springer Science.

Jain, A.K., Pankanti, S., Prabhakar, S., Hong, L., Ross, A., & Wayman, J.L. 2004. Biometrics: a grand challenge. International Conference on Pattern Recognition, Cambridge, U.K.

Jain, A.K., Ross, A., & Nandakumar, K. 2011. Introduction to Biometrics. New York, NY, Springer- Verlag.

Johnston, R. Can iris patterns be used to identify people? 1992. Los Alamos National Laboratory, Chemical and Laser Sciences Division Annual Report LA-12331-PR. 81-86.

Land, E.H., McCann, J.J. 1971. Lightness and retinex theory. J Opt. Soc. Am. 1-11.

Lowe, D. 2004. Distinctive image features from scale-invariant key- points. International Journal of Computer Vision, 60(2), 91–110.

Marsico, M.D., Galdi, C., Nappi, M., Riccio, D. 2014. FIRME: Face Iris Recognition for Mobile Engagement. Image and Vision Computing..

Mehrotra, H., Majhi, B., Gupta, P. 2009. Annular Iris recognition using SURF. Pattern Recognition and Machine Intelligence. 464-469.

Mikolajczyk, K. & Schmid, C. 2004. Scale & affine invariant interest point detectors. International Journal of Computer Vision. 63–86

Mimura, T., Usui, T., & Yamagami, S. 2008. Recent Causes of subconjunctival hemorrhage. Ophthalmologica.

Moravec, H. 1977. Towards automatic visual obstacle avoidance. In International Joint Conference on Artificial Intelligence. 12, 19

Narvekar, N.D., & Karam, L. J. 2009. A no-reference perceptual image sharpness metric based on a cumulative probability of blur detection. International Workshop on Quality of Multimedia Experience.

Narvekar, N.D., & Karam, L. J. 2011. A no-reference image blur metric based on the cumulative probability of blur detection (CPBD). IEEE Transactions Image Processing.

Neubeck, A., & Gool, L.V. 2006. Efficient non-maximum suppression. In Proceeding of 18th International Conference on Pattern Recognition. 3. 850–855.

NICE: II, 2010. Noisy Iris Challenge Evaluation – Part II

Ortega, M., Marino, C., Penedo, M.G., Blanco, M., & Gonzalez, F. 2006. Biometric authentication using digital retinal images. Proc. of the 5th WSEAS International Conference on Applied Computer Science. 422-427.

Owen, C. G., Newsom, R.S., & Rudnicka, A. R., 2005. Vascular response of the bulbar conjunctiva to diabetes and elevated blood pressure. Ophthalmology. 1801–8.

Owen, C.G., Newsom, R.S., Rudnicka, A.R., Barman, S.A., Woodward, E.G., & Ellis, T.J. 2008. Diabetes and the Tortuosity of Vessels of the Bulbar Conjunctiva. Ophthalmology

Padole, C. N., & Proenca, H. 2012. Periocular recognition: Analysis of performance degradation Factors. International Conference in Biometrics (ICB). 439–445. 25, 26

Park, U., Ross, A., & Jain, A., 2009. Periocular biometrics in the visible spectrum: A feasibility study. International Conference on Biometrics: Theory, Applications, and Systems (BTAS). 1 – 6.

Proença, H., Filipe, S., Santos, R., Oliveira, J., & Alexandre, L.A., 2010. The UBIRIS.v2: a database of visible wavelength iris images captured on-the-move at-a-distance. IEEE Trans. Pattern Analysis and Machine Intelligence. 1529–1535.

Proenca, H & Alexandre L.A. 2005. UBIRIS: A noisy Iris Image Database. International Conference on Image Analysis and Processing. 1. 970-977.

Raja, K. B., Raghavendra, R., Vemuri, V. K., Busch, C. 2014. Smartphone based iris recognition using deep sparse filtering. Pattern Recognition Letters (in press).

Ross, A., & Jain, A.K. 2003. Information fusion in biometrics, Pattern Recognition Letters. 2115–2125.

Ross, A., & Jain, A.K. 2004. Multimodal biometrics: an overview, Proceedings of the 12th European Signal Processing Conference. 1221–1224.

Ross, A., Othman, A. 2014. Iris and Periocular recognition using mobile phones. The Biometric Consortium.

Rosten, E., & Drummond, T. 2006. Machine learning for high-speed corner detection. European Conference on Computer Vision (ECCV'06). 1. 430–443.

Rosten, E., Porter, R., & Drummond, T. 2009. Faster and better: A machine learning approach to corner detection. IEEE Trans. Pattern Analysis and Machine Intelligence. 32(1). 105-119.

Rother, C., Kolmogorov, V., & Blake, A. 2004. "GrabCut": interactive foreground extraction using iterated graph cuts. ACM Trans. on Graphics (TOG). 23(3). 309-314.

Santos, G., Grancho, E., Bernardo, M.V., Fiadeiro, P.T. 2014. Fusing iris and periocular information for cross-sensor recognition. Pattern Recognition Letters (in press).

Schmid, N. A., & Nicolo, F. 2009. A method for selecting and ranking quality metrics for optimization of biometric recognition systems. IEEE Computer Society Conference on Computer Vision and Pattern Recognition Workshops. 1-8.

Shi, J., & Tomasi, C. 1993. Good features to track. Technical report, Cornell University, Ithaca, NY, USA. 12, 21

Singh, R., Vatsa, M., & Noore, A. 2007. Improving verification accuracy by synthesis of locally enhanced biometric images and deformable model. Signal Process. 87. 2746 - 2764.

Smith, J.R., Mackensen, F., & Rosenbaum, J.T. 2007. Therapy Insight: Scleritis and Its Relationship to systemic autoimmune disease. Nature Clinical Practice Rheumatology. 3(4). 219-226.

Smith, S.M., & Brady, J.M. 1997. Susan - a new approach to low level image processing. International Journal of Computer Vision. 23. 45–78.

Smith, S.M., & Brady, J.M. 1997. Susan - a new approach to low level image processing. International Journal of Computer Vision. 23. 45–78.

Soille, P., 1999. Morphological Image Analysis: Principles and Applications, Springer. 164-165.

Tankasala. S.P., Doynov, P., & Derakhshani, R. 2013. Application of pyramidal directional filters for biometric identification using conjunctival vasculature patterns. IEEE International Conference on Technologies for Homeland Security. 639-644.

Thomas, N.L., Du, E.Y., & Zhou, Z. 2010. A new approach for sclera vein recognition. Proc. SPIE, Mobile Multimedia/Image Processing, Security, and Applications.

Tomasi, C., & Kanade, T. 1991. Detection and tracking of point features. Technical report, Carnegie Mellon University.

Torr, P.H.S, & Murray, D.W. 1997. The development and comparison of robust methods for estimating the fundamental matrix. International Journal of Computer Vision. 24(3). 271–300.

Wang, Z., Sheikh, H. R., & Bovik, A. C. 2002. No-reference perceptual quality assessment of JPEG compressed images. IEEE International Conference Image Processing. 477–480.

Zhou, Z., Du, E.Y., & Thomas, N.L. 2010. A comprehensive sclera image quality measure. 11th International Conference on Control Automation Robotics & Vision. 638-643.

Zhou, Z., Du, E.Y., Thomas, N.L., & Delp, E.J. 2010. Multimodal eye recognition. Proc. SPIE, Mobile Multimedia/Image Processing, Security, and Applications.

Zhou, Z., Du, E.Y., Thomas, N.L., & Delp, E.J. 2012. A new human identification method: Sclera Recognition. IEEE Trans. on Systems, Man and Cybernetics, Part A: Systems and Humans. 42(3). 571-583.

Flom, L., and Safir, A.: ‘Iris recognition system’. U.S. Patent 4641394, 1987

Johnston, R. 1992. Can iris patterns be used to identify people? Los Alamos National Laboratory, Chemical and Laser Sciences Division Annual Report LA-12331-PR. 81–86.

VITA

Sashi K. Saripalle received the bachelor's degree in Electronics and Communication Engineering from Guru Nanak Engineering College, India, in 2008 and the M.S. degree in Electrical Engineering from University of Missouri Kansas City (UMKC), Kansas City, in 2010. He is currently working towards the Ph.D. degree in the department of Computer Science and Electrical Engineering, UMKC. Since Summer 2012, he has been working with EyeVerify as R&D Intern.

He received the best paper award in the IEEE conference on Technologies for Homeland and Security 2012, and Outstanding Ph.D. Student award from the Department of Computer Science and Electrical Engineering, UMKC, in 2014. He is also a recipient of Preparing Future Faculty (PFF) Award and Graduate Research Scholarship. His research interests include image processing, computer vision and, machine learning. He has authored or co-authored 5 research papers, 2 issued patents and 3 filed patents.